NEAR WALL STRUCTURE AND DEVIATION FROM EQUILIBRIUM IN WAVY CHANNEL TURBULENCE

By

SAADBIN KHAN
Bachelor of Science in Mechanical Engineering.
Bangladesh University of Engineering and Technology
Dhaka, Bangladesh
2016

Submitted to the Faculty of the
Graduate College of
Oklahoma State University
in partial fulfillment of
the requirements for
the Degree of
MASTER OF SCIENCE
July, 2019

NEAR WALL STRUCTURE AND DEVIATION FROM EQUILIBRIUM IN WAVY CHANNEL TURBULENCE

Thesis Approved:

Dr. Balaji Jayaraman

Thesis Advisor

Dr. Jamey Jacob

Dr. Omer San

ACKNOWLEDGMENTS

I would like to thank my family and friends for constantly encouraging me all my life and my advisor, Dr. Balaji Jayaraman for sharing his unparalleled knowledge and exemplary guidance throughout last two years. I acknowledge the computing resources and support from Oklahoma State University, High Performance Computing Center. I am indebted to Mr. Jesse Schafer for his timely support while performing the DNS runs. I also acknowledge the contributions of Mr. Prashant Tarey in helping set-up the initial runs for this study.

Acknowledgments reflect the views of the author and are not endorsed by committee members or Oklahoma State University.

To my grandmother for her unconditional care over last 25 years.

Name: Saadbin Khan

Date of Degree: July, 2019

Title of Study: NEAR WALL STRUCTURE AND DEVIATION FROM EQUILIBRIUM IN WAVY CHANNEL TURBULENCE

Major Field: Mechanical & Aerospace Engineering

Abstract: The structure of turbulent flow over non-flat surfaces is a topic of major interest in practical applications in both engineering and geophysical settings. A lot of work has been done in the fully rough regime at high Reynolds numbers where the effect on the outer layer turbulence structure and the resulting friction drag is well documented. It turns out that surface topology plays a significant role on the flow drag especially in the transitional roughness regime and therefore, is hard to characterize. Survey of literature shows that roughness function depends on the interaction of roughness height, flow Reynolds number and topology shape. In addition, if the surface topology contains large enough scales then it can impact the outer layer dynamics and in turn modulate the total frictional force. Therefore, it is important to understand the mechanisms underlying drag increase from systematically varied surface undulations in order to better interpret quantifications based on mean statistics such as roughness function. In this study, we explore the mechanisms that modulate the turbulence structure over a two-dimensional (2D) sinusoidal wavy surface with a fixed amplitude, but varying slope. To accomplish this, we model the turbulent flow between two infinitely wide 2D wavy plates at a bulk Reynolds number, $Re_b = 2800$. We pursue two different but related flavors of analysis. The first one focuses on understanding the non-equilibrium near surface turbulence structure and the second one adopts a roughness characterization of such wavy surfaces. Analysis of the different statistical quantifications show strong dependence on wave slope for the roughness function indicating drag increase due to enhanced turbulent stresses resulting from increased production of vertical velocity variance from the surface undulations. Also, pronounced asymmetry is reported when comparing the turbulence structure on the upstream and downstream region of the wave.

TABLE OF CONTENTS

Chapter Page

I Introduction **1**
1.1 Application and Early Literature 1
1.2 Estimating Drag and Related Effects Due to Rough Topology 2
1.3 Outer Layer Similarity 3
1.4 Challenge in Roughness Characterization 4
1.5 Scope of the Current Work 6
1.6 Organization 8

II Numerical Methods **9**
2.1 Governing Equations 9
2.2 Immersed Boundary Method (IBM) 10
2.3 Simulation Design 12
2.4 Convergence of Turbulence Statistics 13
2.5 Assessment of Simulation Accuracy 15

III Mean Turbulence Structure **17**
3.1 Streamwise Averaging of Turbulence Statistics 18
3.2 Outer Layer Similarity and Mean Velocity Profiles 20
3.3 Quantification of Mean Velocity Gradients and Inertial Sublayer . . 22
3.4 Characterization of Reynolds Stress Tensor and its Production . . . 25
3.4.1 Streamwise Variance 26
3.4.2 Vertical Variance 30
3.4.3 Spanwise Variance 32
3.4.4 Mean Turbulent Kinetic Energy 34
3.4.5 Vertical Turbulent Momentum Flux 35

IV Roughness Characterization **36**
4.1 Characterization of the Roughness Function and Roughness Scales . 36
4.2 Characterization of Horizontal Flow Stress and Implications to Drag 41

V Streamwise Variability and Asymmetric Structure **44**
5.1 Streamwise Variability of Turbulence Structure 44
5.2 Averaging in Fixed Global Coordinate and Inhomogeneity Effect . . 49
5.3 Stationwise Dissection of Asymmetric Structure 55
5.4 Quantification of the Deviation 67

VI Conclusion and Future Work **72**
6.1 Conclusion 72
6.2 Future Work 74

References **76**

A Numerical Scheme Expanded **81**
1.1 Governing Equations 81
1.2 Fractional Step Method 81
1.3 Discretizing the Derivatives 83

B Roughness Function Correlations of Nikuradse and Colebrook . **84**
2.1 **Nikuradse's Correlations** 84
2.2 **Colebrook's Correlation** 84

C Dissection of the Transport Equation for Reynolds Stress Tensor **86**

LIST OF TABLES

Table Page

2.1 Tabulation of different design parameters for the simulations such as: wavelength (λ), amplitude (a) and steepness ($\zeta = \frac{2a}{\lambda}$) of the wavy surface, friction velocity (u_τ), Reynolds numbers (Re) based on boundary layer height (δ) and different velocities expressed as the subscripts ('cl'=centerline velocity, 'b'=bulk velocity, 'τ'=friction velocity) and the grid spacing in different directions ('Δx'=streamwise, 'Δz'=spanwise, 'Δy_w'=wall normal near the wall, 'Δy_{cl}'=wall normal near the flow centerline). Superscript '+' refers to inner scaled quantity (scaled with respect to dynamic viscosity (ν) and friction velocity (u_τ)). 13

4.1 Tabulation of estimated turbulence parameters, namely, von Kármán constants for the different cases and commonly used roughness parameters. 39

LIST OF FIGURES

Figure Page

2.1 Illustration of 1D polynomial reconstruction based on Lagrangian polynomial. The solid black curve in (a) represents the fluid-solid interface, red triangular markers represents solid gridpoints where the reconstruction is performed using the fluid gridpoints shown as filled blue circular markers along with the target quantity on the interface marked as filled green circular marker. To retain stability the gridpoints represented as the empty blue circular markers just above the interface is ignored from the reconstruction computation. Dotted black rectangle shows the direction along which the 1D reconstruction is performed as the gridpoints under consideration is enclosed by this rectangle. In (b) a velocity curve is shown which has zero enforced value on the surface (at filled green circular marker). Using the values on the three gridpoints marked as filled blue circle, we extend the curve by computing values on the solid region (at red triangular markers). 11

2.2 Schematic illustration of the Cartesian grid with the immersed boundaries of different shapes in (a) and a close-up of the buffer region in (b). The solid thick curve represents the wave for $\lambda = 4\pi$ and the dashed line for $\lambda = \frac{8\pi}{3}$. A similar setup is used for other surface shapes as well. 13

2.3 Quantification of statistical stationarity for the different DNS data sets using the residual of mean horizontal stress from 2500 samples collected over $\sim 12\frac{\delta}{u_\tau}$. 14

2.4 Comparison of mean velocity and RMS velocity fluctuation between DNS of flat channel turbulent flow with IBM and the Kim et al. (1987) DNS without IBM 16

3.1 Comparison of instantaneous flow separation for the different wave steepness, ζ. The wavy surface is denoted in cyan and the separation in red. 17

3.2 Inner scaled mean (a) streamwise velocity, (b) vertical velocity, (c) spanwise velocity and (d) defect velocity computed using local coordinate-based average. The thick lines represent averaging at constant $y_{local,1}$ and the thin lines with markers represent averaging at scaled $y_{local,2}$. Three vertical straight lines correspond to the different a^+ for $\zeta > 0$ (see Table 2.1). 19

3.3 Spanwise and temporally averaged streamwise and vertical velocity over wavy surfaces in turbulent channel flow. 21

3.4 Variation of non-dimensional mean streamwise velocity gradients, (a) $\gamma = y^+ \frac{d\langle u \rangle^+_{x,z,t}}{dy^+}$ and (b) $\Phi = \frac{\kappa y}{u_\tau} \frac{d\langle u \rangle_{x,z,t}}{dy}$.The thin dashed black line in (a) corresponds to the mean γ valued 2.5582 computed based on $y^+ = 60-110$. 23

3.5 Schematic illustrating the wall-normal variation of streamwise averaged production of turbulent kinetic energy in (a) inner variable non-dimensionalized and (b) dimensional (m^2/s^3) forms. 25

3.6 Inner scaled mean (a) streamwise variance, (b) vertical variance, (c) spanwise variance and (d) turbulent kinetic energy (TKE). The horizontal lines correspond to height with maximum value of the statistics along the profile. 26

3.7 Schematic illustration of the wall-normal variation of inner-scaled double averaged production of streamwise (a,b,c) variance, $\langle P_{11}\rangle_x^+$ and vertical (d,e,f) variance, $\langle P_{22}\rangle_x^+$. In each row, we further split the corresponding production terms into $\langle P_{11}^{u'u'}\rangle_x^+$ (b), $\langle P_{11}^{u'v'}\rangle_x^+$ (c), $\langle P_{22}^{v'u'}\rangle_x^+$ (e) and $\langle P_{22}^{v'v'}\rangle_x^+$ (f) respectively. The horizontal lines correspond to the vertical location of maximum value for a chosen statistic. If the peak locations are different, we color match the horizontal lines with the corresponding curves. 29

3.8 Inner scaled mean production contours 30

3.9 Inner scaled mean (a) covariance $\langle u'v'\rangle_{x,z,t}^+$, (b) covariance $\langle u'v'\rangle_{x,z,t}^+$ (zoomed near the surface) and (c) vertical gradient of streamwise velocity, $d\langle u^+\rangle_{x,z,t}/dy^+$. The black horizontal line corresponds to the average of the maximum magnitude of $\langle u'v'\rangle_{x,z,t}^+$ for the different ζ. Note that the individual peak values were too close to each other to be shown separately. 33

4.1 Variation of the different roughness quantifications with ζ in (a), (b), (c) and wall normal variation of mean roughness function in (d). . . 38

4.2 Variation of mean roughness function (a) with roughness Reynolds number and (b) with effective slope in comparison with reported data from known literature. 39

4.3 The schematic shows the inner scaled mean (a) horizontal stress, (b) viscous stress and (c) Reynolds stress in the top row and the dimensional mean (d) horizontal stress, (e) viscous stress and (f) Reynolds stress in the bottom row. The vertical lines correspond to the different a^+ values. 42

5.1 Spanwise and temporally averaged inner scaled (a) streamwise and (b) vertical velocity and (c) horizontal stress 46

5.2 Spanwise and temporally averaged inner scaled (a) streamwise, (b) vertical and (c) spanwise variances 47
5.3 Spanwise and temporally averaged inner scaled (a) $\langle u'v' \rangle_{z,t}$ co-variance, (b) TKE and (c) spanwise vorticity 48
5.4 Inner scaled mean (a) streamwise velocity, (b) horizontal stress, (c) spanwise vorticity, (d) turbulent kinetic energy, (e) streamwise variance, (f) vertical variance, (g) spanwise variance and (h) covariance $\langle u'v' \rangle$ computed using global coordinate-based average. The thin horizontal dashed lines correspond to the different a^+ for $\zeta > 0$ (see Table 2.1). . 50
5.5 Inner scaled inhomogeneity effect on (a) streamwise velocity (b) vertical velocity and (c) horizontal stress 52
5.6 Inner scaled inhomogeneity effect on (a) streamwise variance (b) vertical variance and (c) spanwise variance 53
5.7 Inner scaled inhomogeneity effect on (a) $\langle u'v' \rangle_{z,t}$ covariance (b) spanwise vorticity and (c) TKE 54
5.8 Station architecture for the analysis 55
5.9 Comparison of spanwise and temporally averaged inner scaled streamwise velocity profile at different phase locations (ϕ) of the wave. . . . 58
5.10 Comparison of spanwise and temporally averaged inner scaled horizontal stress profile at different phase locations (ϕ) of the wave. 59
5.11 Comparison of spanwise and temporally averaged inner scaled vertical velocity profile at different phase locations (ϕ) of the wave. 60
5.12 Comparison of spanwise and temporally averaged inner scaled streamwise variance profile at different phase locations (ϕ) of the wave. . . . 61
5.13 Comparison of spanwise and temporally averaged inner scaled TKE profile at different phase locations (ϕ) of the wave. 62

5.14 Comparison of spanwise and temporally averaged inner scaled vertical variance profile at different phase locations (ϕ) of the wave. 63
5.15 Comparison of spanwise and temporally averaged inner scaled spanwise variance profile at different phase locations (ϕ) of the wave. 64
5.16 Comparison of spanwise and temporally averaged inner scaled Reynolds stress profile at different phase locations (ϕ) of the wave. 65
5.17 Comparison of spanwise and temporally averaged inner scaled spanwise vorticity profile at different phase locations (ϕ) of the wave. 66
5.18 Normalized L_2 norm error ($||\epsilon||_2^+$) between upslope and downslope profile of different turbulent quantities: (a) streamwise velocity, (b) wall normal velocity, (c) horizontal stress, (d) streamwise variance, (e) vertical variance, (f) spanwise variance, (g) Reynolds stress, (h) turbulent kinetic energy and (i) spanwise vorticity, plotted against the phase angle, ϕ (The dash-dotted green, dotted red, dotted lime and dash-dotted magenta lines correspond to $\zeta = 0.011$, $\zeta = 0.017$, $\zeta = 0.022$ and $\zeta = 0.044$ respectively) 68
5.19 Inner scaled asymmetry-induced error in (a) streamwise velocity, (b) vertical velocity, (c) horizontal stress, (d) streamwise variance, (e) vertical variance and (f) spanwise variance 69
5.20 Inner scaled asymmetry-induced error in (a) $\langle u'v' \rangle_{z,t}$ covariance (b) spanwise vorticity and (c) TKE 70

ABBREVIATIONS

The following abbreviations are used in this manuscript:

DNS	Direct numerical simulation
LES	Large eddy simulation
RANS	Reynolds-averaged Navier-Stokes equations
IBM	Immersed boundary method
HPC	High performance computing
TKE	Turbulent kinetic energy
TBL	Turbulent boundary layer
PPE	Pressure Poisson equation
FFT	Fast Fourier transform
IFFT	Inverse fast Fourier transform
AB3	Adam-Bashforth 3^{rd} order
6OCCS	6^{th} order central compact scheme
6OSCS	6^{th} order spectral compact scheme
KMM87	Kim, Moin and Moser (1987)
ES	Effective slope

CHAPTER I

Introduction

1.1 Application and Early Literature

Surface undulations can have significant impact on turbulent boundary layers both in the atmosphere as well as in engineering applications. In particular, engineering applications such as internal flows in pipes and turbomachinery, external flows over fouled ship hulls (Schultz, 2007), wind turbine blades and other aerodynamic surfaces are common examples. In the atmospheric side, while most roughness such as grass and shrubs are very small, there exist medium to large scale roughness in the form of tree canopies, man made structures and hills. The ubiquitous nature of such flows has made understanding their dynamics a necessity. A significant amount of research has been devoted to understanding turbulent flows over pipe roughness, for example, the work of Darcy (1857) nearly two hundred years ago, in the early half of twentieth century by Nikuradse (1950), Colebrook et al. (1939) and Moody (1944) and more recently by various research groups (Shockling et al., 2006; Hultmark et al., 2013; Chan et al., 2015). In the last two decades, fundamental investigation of turbulent flows over uniform roughness embedded in flat surface has been undertaken through a series of experimental studies (Flack et al., 2005; Schultz and Flack, 2005, 2007, 2009; Flack and Schultz, 2014; Flack et al., 2007; Flack and Schultz, 2010) as reviewed in Jiménez (2004) and Flack and Schultz (2014). In addition there has been extensive simulation-based research of turbulent boundary layers over systematically designed roughness using direct numerical simulation (DNS) (Napoli et al., 2008; Chan et al., 2015; Leonardi et al., 2007) and large eddy simulation (LES) (De Marchis and Napoli,

2012). There has also been interesting recent work on reproducing Nikuradse-type sand grain roughness using DNS at moderately high Reynolds numbers (Thakkar et al., 2018; Busse et al., 2017).

1.2 Estimating Drag and Related Effects Due to Rough Topology

Through the extensive and growing body of literature, the underlying goals and fundamental questions remain consistent, namely, how to estimate flow drag over a given roughness topology at a specified Reynolds number or flow rate. From a geophysical perspective, the goal is to model the outer layer dynamics and understand the turbulent coherent structures within the roughness sublayer that impact man-made applications in the lower atmosphere (Jayaraman and Brasseur, 2014, 2018; Coceal et al., 2006). From a computational standpoint, the question is one of modeling the effective dynamics within the roughness sublayer to bypass the complexity of resolving the roughness elements.

Significant early attempts to answer some of the above questions were the work of Nikuradse (1950) and the subsequent extension by Colebrook et al. (1939) to relate flow drag with roughness. Both these efforts classify roughness as hydraulically smooth, transitional or fully rough regimes depending on the relationship between drag and roughness scales. In the fully rough regime, drag is independent of the Reynolds number and depends only on the roughness scale whereas in the transitional regime both of these are important as per Colebrook et al. (1939) and Nikuradse (1950). These ideas are summarized in the popular Moody diagram (Moody, 1944). A more generic quantification of roughness induced effects applicable across different classes of flows is the Hama roughness function (Hama, 1954), $\Delta\langle u\rangle^+$ which is commonly aligned with the classical view of rough wall turbulent boundary layers. Specifically, the classical view is that roughness influences the turbulence structure only up to a few roughness lengths from the mean surface location while the outer layer flow is unaffected except

for a modulation in the velocity and length scales - a rough wall extension of Townsend's Reynolds number similarity hypothesis (Townsend, 1980). Townsend's hypothesis states that in the high Reynolds number limit, the outer layer motions (outside the roughness sublayer) are independent of the wall boundary condition except for the role it plays in modifying the outer layer velocity (u_τ) and length scale, δ. Therefore, this notion of 'wall similarity' (Raupach et al., 1991) implies that shape of the mean velocity in the overlap and outer layers is unaffected (relative to a smooth wall) by the roughness. This phenomenology is mostly consistent with observations as per Jiménez (2004), but exception do exist. Quantitatively, the roughness function represents the downward displacement in the mean velocity profile plotted in a semi-log scale indicative of the increased drag from the surface inhomogeneities. Combined with Townsend's wall similarity hypothesis, $\Delta\langle u\rangle^+$ represents the shift in the intercept used to describe the logarithmic region of the mean velocity profile as

$$\underbrace{\langle u\rangle^+ = \frac{1}{\kappa} ln(y^+) + B}_{\text{Log law for smooth wall}} - \underbrace{\Delta\langle u\rangle^+}_{\substack{\text{Roughness} \\ \text{function}}}, \tag{1.1}$$

where, κ is the von Kármán constant, $\langle u\rangle^+$ is the averaged streamwise velocity over a rough surface and y^+ is the wall coordinate. Normalization is done using the inner layer variables such as friction velocity, u_τ and kinematic viscosity, ν expressed as $\langle u\rangle^+ = \frac{\langle u\rangle}{u_\tau}$ and $y^+ = \frac{yu_\tau}{\nu}$.

1.3 Outer Layer Similarity

Understanding the extent of universality and conditions for the existence of outer layer similarity continues to be a major topic of interest (Flack and Schultz, 2014; Jiménez, 2004). The underlying assumption behind wall similarity is that there is sufficient scale separation between the boundary layer thickness, δ and the roughness height, k. Consequently, the roughness sublayer is expected to be relatively thin

(compared to the boundary layer thickness) as it scales with k. However, the precise nature of this scaling relationship depends on the detailed roughness topology. Flack et al. (2005, 2007) explored the concept of 'critical' roughness height and conditions for the existence of outer layer similarity. In their work, outer layer similarity was consistently encountered even for moderately high Reynolds numbers over uniform three-dimensional rough surfaces with reasonably large roughness elements. In fact, little to no deviations in outer layer similarity was observed for $\delta/k \gtrsim 20$ and $\delta/k_s \gtrsim 6$ where k, k_s are the mean roughness height and equivalent sand grain roughness respectively. Importantly, it was reported that there exists no critical roughness height (i.e. a height corresponding to a sharp transition) as the influence of roughness size on outer layer statistics is more gradual. These trends appear to break down for two-dimensional roughness (especially periodic) which are known to generate stronger vertical disturbances due to the absence of significant spanwise motions in the roughness sublayer. This two-dimensional surface effect is clearly observed in higher order statistics and less so for the mean velocity profiles. Volino et al. (2011, 2009) clearly illustrate this using experiments with transverse two-dimensional bars and three-dimensional cubes as roughness elements ($\delta/k_s \approx 2-3$) and flow friction Reynolds numbers, $\delta^+ \approx 2000$. Subsequently, Krogstad and Efros (2012) show that flow over two-dimensional roughness elements with higher δ/k and at higher Re_τ (larger scale separation) generate outer layer similarity just like three-dimensional roughness. Therefore, the details of the roughness topology along with the roughness scale and the flow Reynolds number modulate turbulence structure. It is only their relative importance that changes across the different regimes.

1.4 Challenge in Roughness Characterization

The frictional drag from the surface is also strongly influenced by the surface topology and not just the roughness scale. The correlation of friction coefficient with Reynolds

number in the Moody diagram (Moody, 1944) is parameterized for mean roughness height. By leveraging the existence of outer layer similarity, the shift in the mean profile or roughness function is used as a surrogate for prediction of increase in friction drag over a given rough surface. The roughness correlations of Nikuradse (1950) or Colebrook et al. (1939) relate $\Delta\langle u\rangle^+$ to k^+ (scaled roughness height) using $\Delta\langle u\rangle^+ = (1/\kappa)\log(k^+) + B - 8.5$ and $\Delta\langle u\rangle^+ = (1/\kappa)\log(1 + 0.3k^+)$ respectively. The Nikuradse expression is calibrated for the uniform sand grain roughness while the Colebrook relationship is designed for commonly occurring surfaces. However, there exists many examples where $\Delta\langle u\rangle^+$ does not depend solely on k^+ such as a turbulent flow over two-dimensional transverse (or wavy surfaces as reported in this work) bars (Perry and Li, 1990) separated by distances comparable to the height. Perry et al. (1987) classify such cases as "d-type" roughness in contrast to "k-type" roughness where $\Delta\langle u\rangle^+$ scales with k^+. In the case of closely spaced transverse bars, there exist vortical flow cells between each of these elements thus causing the turbulent flow to skim over which makes $\Delta\langle u\rangle^+$ depend little if any on k^+. Schultz and Flack (2009) systematically study turbulent flow over three-dimensional pyramid elements of different heights and inclination angles to understand the role of roughness slope in addition to k on the drag. Their results clearly indicate that smaller slopes produce significant deviation from the uniform sand roughness behavior with $\Delta\langle u\rangle^+$ changing slower with k^+ in the transitionally rough regime. Further, these deviations get stronger with increase in inner scaled roughness height. Nakato et al. (1985) report similar observations for sinusoidal wavy surfaces with slopes greater than $\sim 6^\circ$ mimicking the uniform sand roughness behavior. Physical insight for these observations is available from the numerical work of Napoli et al. (2008) who superposed sinusoidal waves to generate a corrugated two-dimensional rough surface. From their work, the anomalous relationship between $\Delta\langle u\rangle^+$ and k^+ at small slopes or 'waviness' regime is attributed to the dominance of viscous drag over form drag. On the contrary, in the 'roughness'

regime involving higher slopes (as in Nikuradse (1950); Thakkar et al. (2018); Flack et al. (2007)), the form drag dominates. To characterize these deviations, they design a slope dependent roughness parameter termed as *effective slope*, ES, that represents the average surface slope magnitude over a given sampling region. In their findings, $\Delta\langle u\rangle^+$ varies linearly with ES for ES < 0.15 (beyond which $\Delta\langle u\rangle^+$ is constant for a given k^+) whereas Schultz and Flack (2009) report that the transition happens at ES < 0.35. Therefore, ES is an additional 'waviness' parameter along with k^+ that modulates $\Delta\langle u\rangle^+$, i.e. $\Delta\langle u\rangle^+ = f(k^+, ES)$. Of course, one can build a rich enough parameter space in addition to ES and a to learn f using advanced data science methods.

1.5 Scope of the Current Work

In this study we explore the structure of near-wall turbulence and deviations from equilibrium flat channel turbulence in the waviness regime using direct numerical simulation of wavy channel flow at a friction Reynolds number, $Re_\tau = \delta^+ \approx 180$. The simulation infrastructure uses higher-order spectral like compact schemes (Laizet and Lamballais, 2009) for both advection and diffusion terms while a third-order multi-step method is used for time integration. The wavy surface is represented using an immersed boundary method (Peskin, 1972; Parnaudeau et al., 2004) similar to many other efforts (Busse et al., 2017; Leonardi et al., 2007). The focus of our current analysis is to better understand the mechanisms underlying the drag increase at small slope angles dominated by viscous drag. For the sinusoidal two-dimensional surfaces considered in this study, the effective slope, ES is directly related to the non-dimensional ratio of the amplitude (a) and wavelength (λ) of the sinusoid, i.e. ES $= 4a/\lambda = 2\zeta$ where ζ is the steepness factor. In this research, ζ is deliberately varied from 0 to 0.044 (ES $\sim 0 - 0.088$) which is nearly an order of magnitude smaller than the transition location (in ES) beyond which $\Delta\langle u\rangle^+$ becomes constant for a

given mean roughness height a^+. For this range of slope parameter (ζ), there exists very little flow separation over the 2D surface and consequently, very little spanwise flow. The roughness height or wave amplitude, a, is chosen to generate moderate scale separation, i.e. $\delta/a \approx 15$ and the ratio based on the equivalent sand roughness height (assuming the Nikuradse (1950) form) turns out to be $\delta/k_s \approx 30-50$. These values are normally sufficient to generate outer layer similarity based on the three-dimensional surface roughness studies of Flack et al. (2007) and Flack and Schultz (2014), but may not be adequate for the two-dimensional wavy surfaces used in this study. Therefore, analysis in this work will focus on assessing the extent of outer layer similarity and the relationships between roughness function, effective slope and roughness/wave height. In addition, we delve into the nature of roughness induced deviations on higher order turbulence statistics and their production mechanisms in order to generate a process level understanding. Note that the roughness Reynolds numbers used in the work ($a^+ \approx 13-14$) fall within the transitional regime.

The primary goal of this study is three-fold: (i) to explore the non-equilibrium, near-surface turbulence structure over systematically varied sinusoidal undulations, (ii) characterize the roughness characteristics of such wavy surfaces and (iii) explore the inhomogeneity induced streamwise asymmetry. In addition, wherever possible, we quantify deviations from equilibrium phenomenology as evidenced in flat channel turbulence, assess the extent of outer layer similarity and relate to characteristic roughness induced effects as appropriate. To accomplish this, we use conventional turbulence quantifications such as mean first and second order statistics (velocity variances and turbulent kinetic energy (TKE)), horizontal flow stress, mean non-dimensional velocity gradient profiles.

1.6 Organization

The rest of the article is organized as follows. In chapter II, we describe the numerical methods, simulation design, quantification of statistical convergence and validation efforts. In chapter III, we present the results from the analysis of outer layer similarity, roughness induced drag quantification. We further characterize how the turbulence structure, namely, components of the Reynolds stress tensor and the different production mechanisms are modulated by the wavy surface undulations. Characterization of roughness along with the analysis on flow stresses are presented in chapter IV. In chapter V, the streamwise asymmetry is discussed and quantified. Also, the complexity of streamwise averaging in presence of inhomogeneous surface is addressed in this chapter. Finally in chapter 6.1 we summarize the major findings from this study and in chapter 6.2.

CHAPTER II

Numerical Methods

2.1 Governing Equations

In this study, we adopt a customized in-house version of the Incompact3D code framework developed by Laizet and Lamballais (2009) to perform our DNS study. The dynamical system being solved is the incompressible Navier-Stokes equation for Newtonian flow described in a Cartesian co-ordinate system with x,y,z pointing to streamwise, vertical and spanwise directions respectively. The skew-symmetric vector form of the equations are given by

$$\frac{\partial \mathbf{u}}{\partial t} = -\nabla p - \frac{1}{2}\big[\nabla(\mathbf{u} \oplus \mathbf{u}) + (\mathbf{u}\nabla)\mathbf{u})\big] + \nu\nabla^2\mathbf{u} + \mathbf{f} \text{ and} \tag{2.1}$$

$$\nabla.\mathbf{u} = 0. \tag{2.2}$$

Here $\mathbf{f}$ represents the body force, p represents the pressure field. The fluid density (ρ) is considered unity for this incompressible fluid as we solve these equations in non-dimensional form. We denote the advection-diffusion term by $\mathbf{F}$ for simplicity. Naturally, the above systems of equation can be rewritten to generate a separate equation for pressure.

The system of equations are advanced in time using a 3^{rd} order Adam-Bashforth (AB3) time integration with pressure-velocity coupling using a fractional step method (Kim and Moin, 1985). For the channel flow, the body force term, $\mathbf{f}$ is dropped. The velocity

is staggered by half a cell to the pressure variable for exact conservation of mass. A 6^{th} Order Central Compact Scheme (6OCCS) with quasi-spectral accuracy is used to calculate the first and second derivative terms (contained in $\mathbf{F}$) in the transport equation. The pressure Poisson equation (PPE) is solved using a spectral method by applying Fast Fourier Transform on the elliptic equation to generate an algebraic equation. The right hand side of the PPE is computed using a quasi-spectral accuracy using 6OCCS and then transformed to Fourier space. To account for the discrepancy between the spectrally accurate derivative for the pressure gradient and a quasi-spectral accuracy for the divergence term, the algorithm uses a modified wavenumber in the pressure solver. Appendix A provides more details on the schemes and discretizations.

2.2 Immersed Boundary Method (IBM)

A major downside to the use of higher order schemes as above is the representation of the complex geometry. In particular, the boundary conditions for higher order methods are complex and hard to implement without loss of accuracy near the surface. In this work, we adopt an immersed boundary method (IBM) framework to represent the complex surface shapes. In the IBM the surface representation is accomplished through an added body force term to the governing equations while the background grid can be a simple Cartesian grid. Therefore, this approach saves significant grid generation effort, but is prone to inaccuracies. In this study, we leverage the higher order IBM implementation in Incompact3D using the direct forcing method requiring reconstruction of the velocity field inside the solid region. This can be illustrated using the schematic in figure 2.1. Figure II.1(a) denotes the solid nodes in red, fluid nodes in blue and the interfacial nodes in green. The solid curve represents the continuous shape of the fluid-solid interface. The IBM framework aims to enforce zero velocity at the interface through a velocity field reconstruction in the red solid nodes so that the 6OCCS gradient computations are unaffected. Therefore, the key to the accuracy of

this approach is the velocity reconstruction step inside the solid region (red nodes in the schematic) using information at the blue and green nodes. The numerous different IBM implementations (Parnaudeau et al., 2004) differ in the details of this velocity reconstruction.

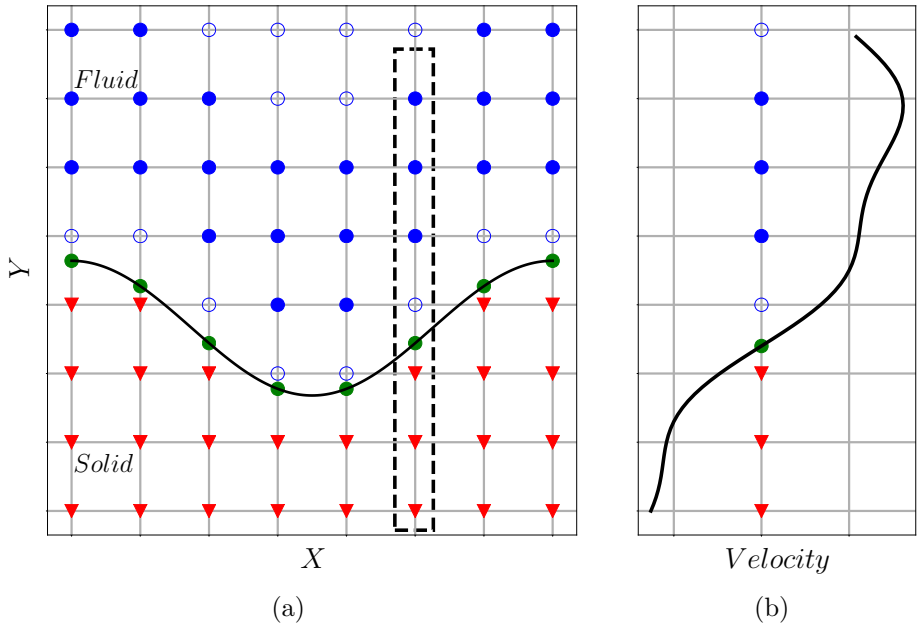

Figure 2.1: Illustration of 1D polynomial reconstruction based on Lagrangian polynomial. The solid black curve in (a) represents the fluid-solid interface, red triangular markers represents solid gridpoints where the reconstruction is performed using the fluid gridpoints shown as filled blue circular markers along with the target quantity on the interface marked as filled green circular marker. To retain stability the gridpoints represented as the empty blue circular markers just above the interface is ignored from the reconstruction computation. Dotted black rectangle shows the direction along which the 1D reconstruction is performed as the gridpoints under consideration is enclosed by this rectangle. In (b) a velocity curve is shown which has zero enforced value on the surface (at filled green circular marker). Using the values on the three gridpoints marked as filled blue circle, we extend the curve by computing values on the solid region (at red triangular markers).

In the current study, we adopt the one-dimensional higher order polynomial reconstruction as reported in Gautier et al. (2014). This reconstructed velocity field is directly used to estimate the derivatives in the advection and diffusion terms of the transport equation. An illustration of this approach is shown in figure II.1(b). Using this 1D polynomial reconstruction, one estimates different solid region velocity fields

when computing the derivatives along the different directions (x, y and z). This is an advantage as well as a disadvantage. However, for the purposes of this study, this approach has shown to be reasonably accurate as described in Section 2.5.

2.3 Simulation Design

We carry out five different simulations of turbulent flows in flat and wavy channels with different steepness levels (ζ), but with the same peak wave height (a) as shown in figure II.2(a). We define an average wave steepness, $\zeta = 2a/\lambda$, where λ is the wavelength. In our study ζ varies from $0 - 0.044$ corresponding to zero, one , one and one half, two and finally, four waves over the streamwise length of the domain. For all these cases, care was taken to ensure that the bulk Reynolds number, $Re_b = \frac{u_b \delta}{\nu}$ is maintained to a constant value of ~ 2800. The corresponding friction Reynolds number, for the flat channel case is ~ 180 which increases slightly with higher ζ. For the wavy channel turbulent flows with the same effective flow volume and mean channel heights, maintaining the same flow rate (or bulk velocity) increases the corresponding friction Reynolds number, $Re_\tau = \frac{u_\tau \delta}{\nu}$, due to increase in u_τ with wave steepness, ζ. However, this increment is as at most $\sim 10\%$ in the current work for upto two waves and therefore is not expected to influence our analysis significantly. In the four wave case, this increment is $\sim 25\%$ and a slight modulation on the regular the analysis is necessary. The simulation parameters for the different cases are summarized in Table 2.1. The simulation domain is chosen as $4\pi\delta \times 2.2\delta \times 4\pi\delta/3$ (including the buffer zone for the IBM) where δ is the boundary layer height. This volume is discretized using a resolution of $256 \times 257 \times 168$ grid points. In the streamwise and spanwise directions, periodic boundary conditions are enforced while a uniform grid distribution is adopted. In wall normal direction, no slip condition representing the presence of the solid wall causes inhomogeneity. To capture the viscous layers accurately, a stretched grid is used. The grid stretching in the inhomogeneous direction is carefully chosen using a

mapping function that operates well with the spectral solver for the pressure Poisson equation. The different inner scaled grid spacings are also included in Table 2.1.

Case	λ	λ^+	a^+	ζ	Δx^+	Δy_w^+	Δy_{cl}^+	Δz^+	Re_{cl}	Re_b	Re_τ	$u_\tau \times 10^3$
A	∞	∞	0	0	8.94	1.05	2.00	4.55	3263	2800	180.9	43.07
B	4π	2354	13.07	0.011	9.23	1.15	2.25	4.70	3277	2800	186.8	44.48
C	$\frac{8}{3}\pi$	1618	13.48	0.017	6.34	1.19	2.32	4.84	3285	2800	192.6	45.85
D	2π	1252	13.92	0.022	9.82	1.23	2.39	5.00	3398	2800	198.7	47.32
E	π	712	15.82	0.044	11.17	1.40	2.72	5.69	3337	2800	226.0	53.82

Table 2.1: Tabulation of different design parameters for the simulations such as: wavelength (λ), amplitude (a) and steepness ($\zeta = \frac{2a}{\lambda}$) of the wavy surface, friction velocity (u_τ), Reynolds numbers (Re) based on boundary layer height (δ) and different velocities expressed as the subscripts ('cl'=centerline velocity, 'b'=bulk velocity, 'τ'=friction velocity) and the grid spacing in different directions ('Δx'=streamwise, 'Δz'=spanwise, 'Δy_w'=wall normal near the wall, 'Δy_{cl}'=wall normal near the flow centerline). Superscript '+' refers to inner scaled quantity (scaled with respect to dynamic viscosity (ν) and friction velocity (u_τ)).

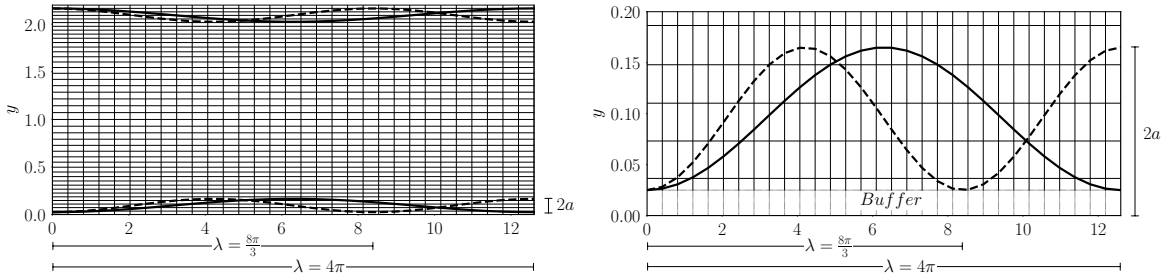

(a) (b)

Figure 2.2: Schematic illustration of the Cartesian grid with the immersed boundaries of different shapes in (a) and a close-up of the buffer region in (b). The solid thick curve represents the wave for $\lambda = 4\pi$ and the dashed line for $\lambda = \frac{8\pi}{3}$. A similar setup is used for other surface shapes as well.

2.4 Convergence of Turbulence Statistics

In order to quantify the convergence of the simulation and ensure statistical stationarity of the turbulence, we consider the streamwise component of the inner scaled mean spatial and temporally averaged horizontal stress that includes both the mean viscous and Reynolds stress components as $\tau_{H,x} = \langle \frac{\partial u}{\partial y} \rangle^+_{x,z,t} - \langle u'v' \rangle^+_{x,z,t}$. Here $\langle \rangle_{x,z,t}$ represents the averaging operation with subscripts denoting averaging directions. In the limit

of statistically stationary and horizontally homogeneous turbulence, $\tau_{H,x}(y)$ can be approximated to a linear profile, $1-\frac{y}{\delta}$ as derived from the mean momentum conservation equations. We estimate a residual convergence error ϵ_{Res} as

$$\epsilon_{Res} = \langle \frac{\partial u}{\partial y} \rangle^{+}_{x,z,t} - \langle u'v' \rangle^{+}_{x,z,t} - (1 - \frac{y}{\delta}), \tag{2.3}$$

whose variation with y/δ is shown in figure 2.3.

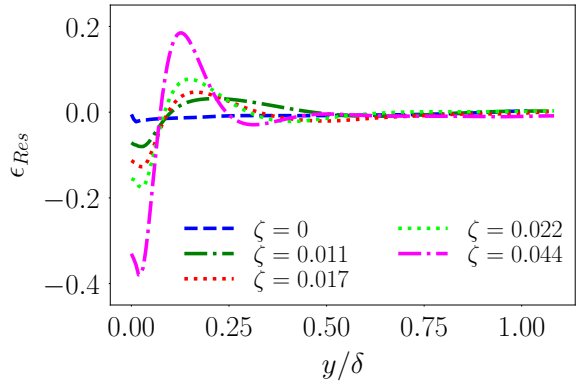

Figure 2.3: Quantification of statistical stationarity for the different DNS data sets using the residual of mean horizontal stress from 2500 samples collected over $\sim 12\frac{\delta}{u_\tau}$.

We note that this error is sufficiently small for the flat channel ($\zeta = 0$) with magnitudes approaching 0.01 near the surface and much smaller in the outer layers. The plot also shows similar quantifications for wavy channel turbulence data with large residual errors near the surface. This is not surprising given that closer to the wall, the turbulence structure is known to deviate from equilibrium due to deviations from horizontal homogeneity. In fact, such deviations from equilibrium phenomenology will be expounded further in the later sections of the article. Nevertheless, we show here that farther away from the surface, the mean horizontal stress approaches equilibrium values as an indicator of stationarity.

2.5 Assessment of Simulation Accuracy

We perform a baseline assessment of the computational accuracy for the turbulent channel flow using an immersed flat channel surface before adopting it for more complex surface shapes. We compare the mean and variance profiles from the current DNS of immersed flat channel flow with the well known work of Kim et al. (1987) (KMM87 here onwards). This turbulent channel flow corresponds to a bulk Reynolds number, $Re_b \approx 2800$, mean centerline velocity Reynolds number, $Re_{cl} \approx 3300$ and a friction Reynolds number, $Re_\tau \approx 180$. KMM87 used nearly 4×10^6 ($128 \times 129 \times 128$) grid points and solved the flow equations by advancing modified variables, namely, wall-normal vorticity and Laplacian of the wall-normal velocity without explicitly considering pressure. They adopt a Chebychev-tau scheme in the wall-normal direction, Fourier representation in the horizontal and Crank-Nicholson scheme for the time integration. In our work, we adopt a spectrally accurate 6^{th} order compact scheme in space and a third order Adam-Bashforth time integration as reported in Laizet and Lamballais (2009). Figure 2.4 clearly shows that the inner-scaled mean (figure II.4(a)) and root mean square of the fluctuations (figure II.4(b)) from the current simulations match that of KMM87. We observe slight differences for the streamwise velocity fluctuation RMS in the outer layer which can be attributed to the improved resolution (and accurate time integration) in our simulations. The method employs a staggered grid arrangement for improved mass conservation.

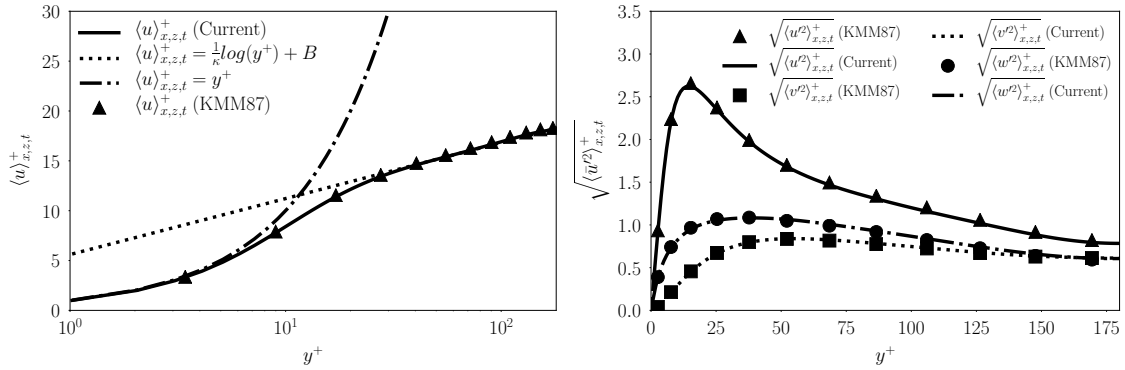

(a) Normalized and averaged streamwise velocity distribution in wall coordinates

(b) RMS normalized velocity fluctuation profiles in wall coordinates

Figure 2.4: Comparison of mean velocity and RMS velocity fluctuation between DNS of flat channel turbulent flow with IBM and the Kim et al. (1987) DNS without IBM

CHAPTER III

Mean Turbulence Structure

As discussed in section 2.3, we consider four different steepness (ζ) levels (table 2.1) including the flat surface to understand the impact on turbulence structure. The flat channel with $\zeta = 0$ represents equilibrium turbulent flow due to horizontal homogeneity and stationarity. To contrast, we consider turbulent flows over wavy surfaces with very little to medium separation as shown in figure 3.1.

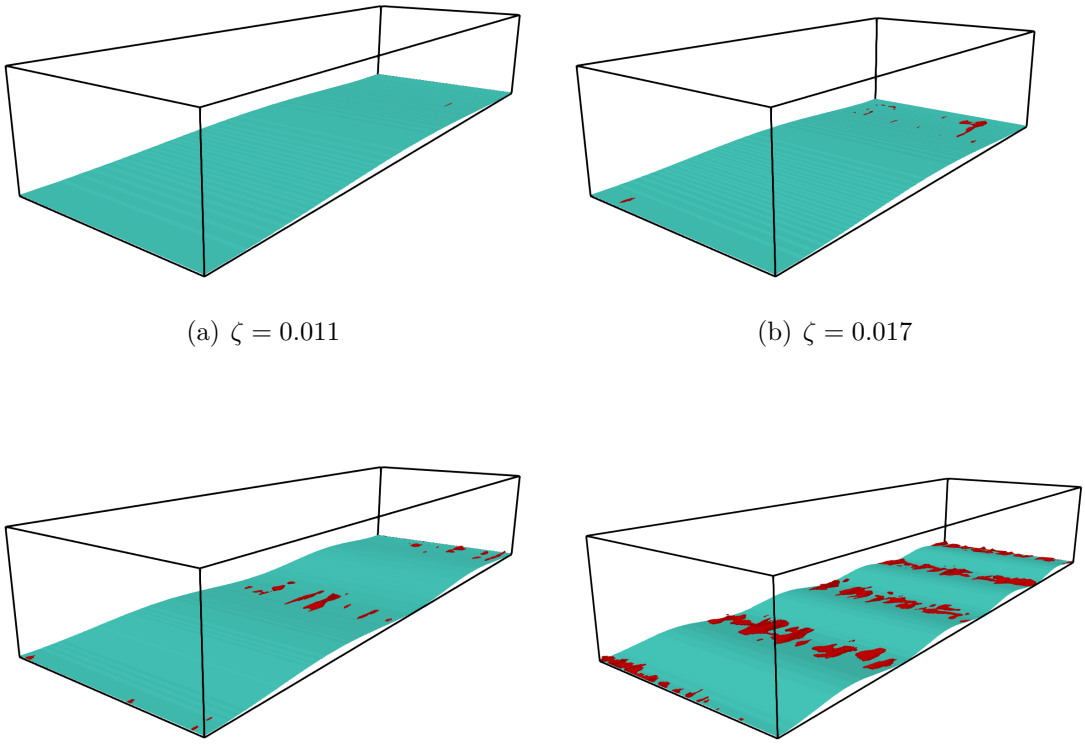

(a) $\zeta = 0.011$ (b) $\zeta = 0.017$

(c) $\zeta = 0.022$ (d) $\zeta = 0.044$

Figure 3.1: Comparison of instantaneous flow separation for the different wave steepness, ζ. The wavy surface is denoted in cyan and the separation in red.

The analysis can be realized using both instantaneous as well as averaged turbulence structure. In this section we focus on the streamwise-averaged or more commonly known as the 'double-averaged' turbulence structure which is a function of solely the wall normal distance. The term 'double-averaging' refers to the combination of averaging along homogeneous ($z,\ t$) and inhomogeneous (x) directions. For the spatial averaging we include both streamwise (x) and spanwise (z) spatial directions and for the temporal (t) averaging we include 2500 three-dimensional snapshots over 20 flow through times for the chosen friction Reynolds number. We use the notation $\langle u \rangle_{x,z,t}$ to specify a quantity u being averaged over x, z and t. For the flat surface, horizontal homogeneity and stationarity implies that x, z and t are equivalentin the averaging operation, $\langle\ \rangle_{x,z,t}$ (i.e. generate equivalent results in the limit of sufficient samples). However when dealing with two-dimensional non-flat surfaces as in this work, only z, t are equivalentand provide sameresults, but depend on x due to absence of streamwise homogeneity near the surface. Therefore, in such situations it is only natural to consider averaged quantities that have both streamwise (x) and vertical (y) variability. This allows one to characterize the near-surface inhomogeneity along both directions. However, in order to quantify deviations from equilibrium and assess the impact of near-surface inhomogeneity on the turbulence we consider streamwise averaged statistics.

3.1 Streamwise Averaging of Turbulence Statistics

In this section, we focus on the deviations from equilibrium in turbulence structure using streamwise averaged statistics that depend only on $\frac{y}{\delta}$ and ζ. To average along the wavy surface, we define a local vertical coordinate, $y_{local,1}$ at each streamwise location with $y_{local,1} = 0$ at the wall. Its maximum possible value is the mid channel height and changes with streamwise location. We then perform streamwise averaging along constant values of $y_{local,1}$, to generate mean statistical profiles. A slight variant

of the above is to use a rescaled coordinate $y_{local,2} = y_{local,1} \times \frac{\delta}{\delta_{local}}$ which stretches $y_{local,2}$ everywhere between $[0, \delta]$ where δ is the mean half channel height. One averages over constant values of $y_{local,2}$ to generate another set of double-averaged mean statistics. Both these approaches implicitly approximate the terrain as nearly flat with a large radius of curvature in a local sense and therefore, nearly homogeneous. This approximation works well when $\frac{a}{\delta} << 1$. In our study $\frac{a}{\delta} = 0.07$ which is an order of magnitude larger than the typical viscous length scale, $L_v = \nu/u_\tau = 1/Re_\tau \approx 0.0055$, but smaller than the log layer ($y^+ \approx 50$) with strong inertial dynamics.

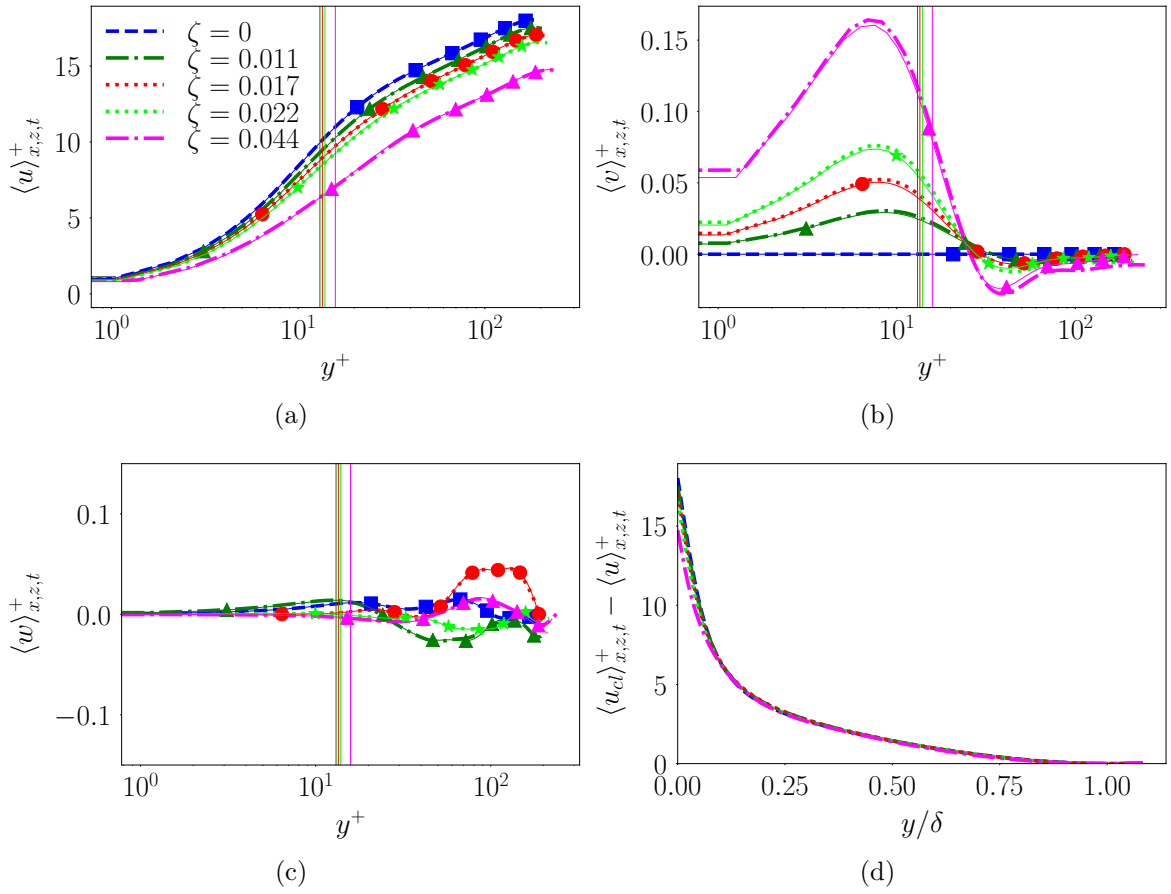

Figure 3.2: Inner scaled mean (a) streamwise velocity, (b) vertical velocity, (c) spanwise velocity and (d) defect velocity computed using local coordinate-based average. The thick lines represent averaging at constant $y_{local,1}$ and the thin lines with markers represent averaging at scaled $y_{local,2}$. Three vertical straight lines correspond to the different a^+ for $\zeta > 0$ (see Table 2.1).

For the mean velocity results presented in this section, we compare both the

averaging approaches to illustrate their closeness to each other. Specifically, we use thick solid lines to denote the mean profiles averaged over constant local coordinate, $y_{local,1}$ and thin lines with markers to denote averaged quantities using scaled local coordinate, $y_{local,2}$. However, for the rest of our analysis, we average over $y_{local,1}$ in a manner consistent with the literature. The different colors, namely, blue, green, red, lime and magenta are associated with different wave steepness, $\zeta = 0$, $\zeta = 0.011$, $\zeta = 0.017$, $\zeta = 0.022$ and $\zeta = 0.044$ respectively.

3.2 Outer Layer Similarity and Mean Velocity Profiles

As the mean channel height (for wavy geometry) is kept constant across all the different steepness, ζ, the observed changes in the mean statistics are only due to surface effects and not the outer layer dynamics. In figure 3.2 we show the inner-scaled, double averaged streamwise, vertical and spanwise velocity along with the streamwise defect velocity for the different cases. The prominent observation for the streamwise velocity is an upward shift (downward shift in the $u^+ - y^+$ plot) of the logarithmic region with increasing wave steepness, ζ (figure III.2(a)) which increases with y^+ before showing near linear growth in the log-layer. This trend is well known for rough-wall turbulent boundary layers (Jiménez, 2004) and is indicative of slowing down of the flow near the wall from increased drag due to the wavy surface for a fixed mass flow rate (bulk Reynolds number). This would naturally result in higher centerline velocities and Re_{cl} as seen in Table 2.1 in order to maintain the prescribed flow rate. The vertical mean velocity structure (figure III.2(b)) is consistent with this interpretation as the wavy undulations generate increasingly stronger net vertical velocity close to the surface with increase in ζ. As seen from figure III.2(b), the mean vertical velocity profile shows systematic upward flow in the viscous and buffer layer along with a weak downward flow in the logarithmic region in order to maintain zero net flow in the vertical direction. It is well known that the mean vertical velocity is zero due to horizontal homogeneity

for the flat channel ($\zeta = 0$). Therefore, these well established vertical motions in the mean over wavy surfaces, although small ($\langle v \rangle^+ = O(0.1)$), represent the most obvious form of deviations from horizontal homogeneity, a prerequisite for equilibrium.

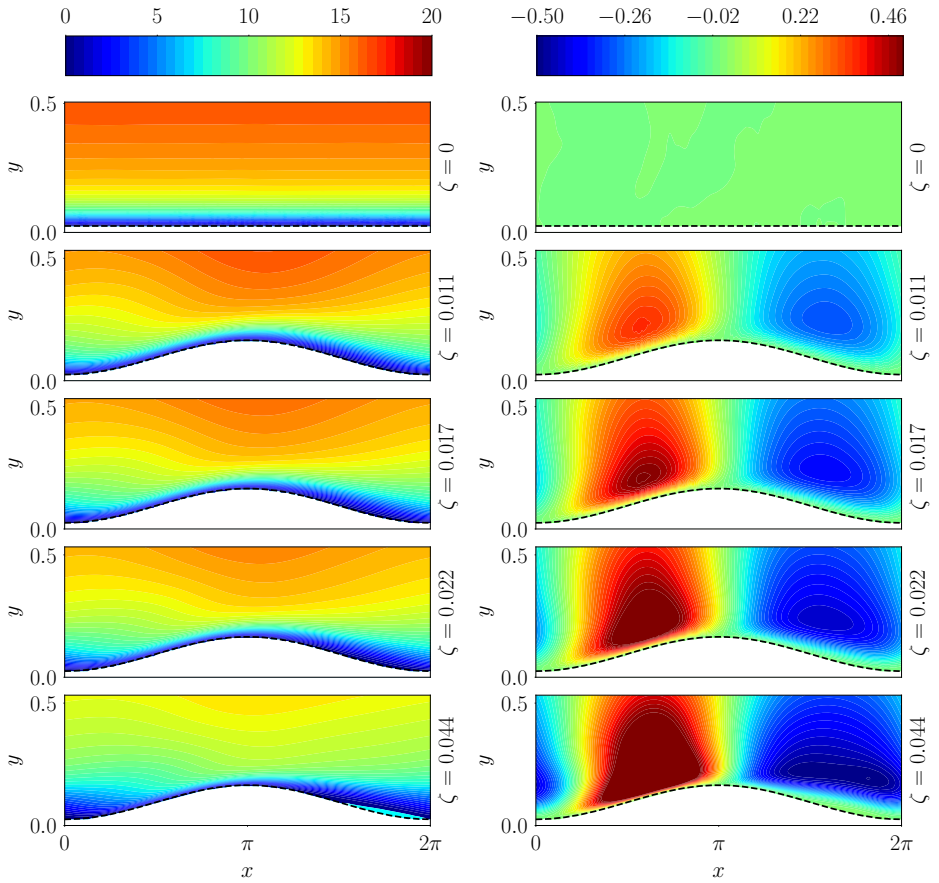

(a) $\langle u \rangle^+_{z,t}$ (b) $\langle v \rangle^+_{z,t}$

Figure 3.3: Spanwise and temporally averaged streamwise and vertical velocity over wavy surfaces in turbulent channel flow.

In particular, the vertical velocity is asymmetric with respect to the symmetric wavy shape as seen from isocontours of time-averaged mean vertical velocity shown in figure 3.3. We observe that the upward and downward slopes display varying tendencies due to presence of adverse and favorable pressure gradients which decelerate (push the flow upward) and accelerate (push downward) the flow as expected. However, the extent of upward deceleration dominates the downward acceleration which breaks the symmetry of the flow patterns around the wave crest. This asymmetry increases with

ζ resulting in stronger net vertical flow in the lower buffer layer (figure III.2(b)).

In spite of these near surface deviations, the dynamics outside the roughness sublayer tend to be similar when normalized and shifted appropriately. To illustrate this outer layer similarity, we show the defect velocity profiles in figure III.2(d) that indicate little to no deviation between $\zeta = 0$ and $\zeta = 0.044$. If anything, the deviation is slightly higher near the surface in the roughness sublayer.

There is no significant trend observed in the spanwise velocity profile shown in figure III.2(c), which can be attributed to the homogeneous nature of the turbulence as well as the geometry in spanwise direction

3.3 Quantification of Mean Velocity Gradients and Inertial Sublayer

The normalized mean streamwise velocity gradients identify the different regions of the turbulent boundary layer and are especially useful to quantify the extent of the inertial sublayer (or the logarithmic region) and the von Kármán constant. In this study, we estimate the normalized premultiplied inner-scaled mean gradient, $\gamma = y^+ \frac{d\langle u \rangle^+_{x,z,t}}{dy^+}$ as shown in figure III.4(a). This function achieves a near constant value of $1/\kappa$ (where κ is the von Kármán constant) in the inertial sublayer due to normalization of the mean gradient by characteristic law of the wall variables, i.e., surface layer velocity (u_τ) and distance from the wall (y). In this study, for the chosen bulk Reynolds number, Re_b (and the realized narrow range of friction Reynolds numbers, Re_τ) we observe that the inertial layer exists over $y^+ \sim 60 - 110$ for $\zeta = 0$ which shifts to $y^+ \sim 75 - 125$ for $\zeta = 0.022$ and $y^+ \sim 85 - 135$ for $\zeta = 0.044$. At the outset, this upward shift (rightward in the plot) in the log layer appears to be associated with the change in wave steepness, ζ and not the small changes ($\sim 10\%$ or lower) in friction Reynolds number, Re_τ for up to $\zeta = 0.022$. For $\zeta = 0.044$, friction Reynolds number is expected to start influencing this shift slightly. The estimated von Kármán constants are tabulated in Table 4.1 and show a range of $0.38 - 0.40$ for the different runs. In

this study, we use the appropriate value of κ to compute the different metrics.

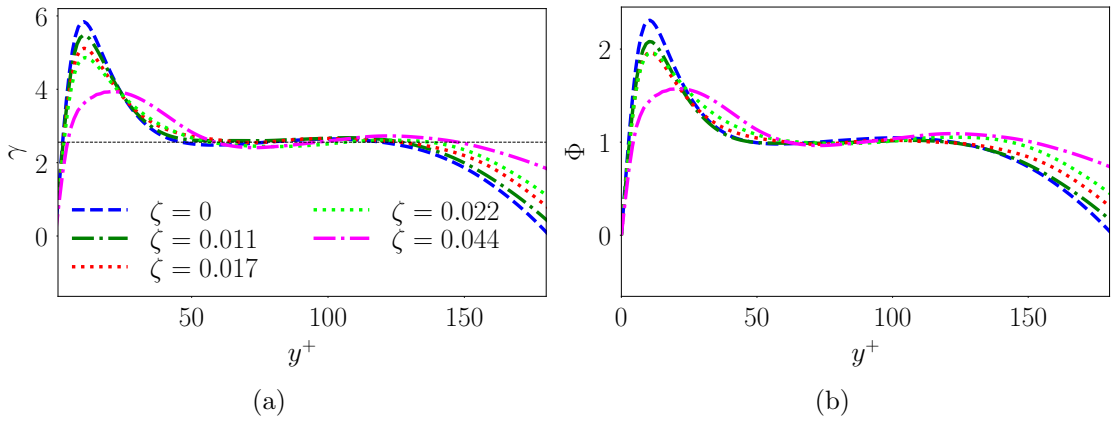

Figure 3.4: Variation of non-dimensional mean streamwise velocity gradients, (a) $\gamma = y^+ \frac{d\langle u \rangle^+_{x,z,t}}{dy^+}$ and (b) $\Phi = \frac{\kappa y}{u_\tau} \frac{d\langle u \rangle_{x,z,t}}{dy}$.The thin dashed black line in (a) corresponds to the mean γ valued 2.5582 computed based on $y^+ = 60 - 110$.

A related quantification often employed to interpret near wall structure is the non-dimensional mean streamwise velocity gradient, $\Phi = \frac{\kappa y}{u_\tau} \frac{d\langle u \rangle_{x,z,t}}{dy}$ whose variation with inner-scaled wall normal distance is shown in figure III.4(b). It is easy to see that $\gamma = \Phi/\kappa$. We observe that the Φ profiles for different ζ mimic the characteristic equilibrium structure starting from zero at the wall followed by a peak at the edge of viscous layer and subsequently, a gradual decrease in the buffer layer to a value of one in the inertial sublayer. This clearly indicates outer layer similarity. In fact, there exists an overall shape similarity in Φ hinting at the potential for universality if only the appropriate scales at the different regimes can be identified.

The origin of the 'overshoot' or near-surface peak is well known and is related to the inconsistency from normalization of the mean gradient using inertial scale variables closer to the surface (viscous layer) where the physically relevant characteristic length scale is $L_v = \nu/u_\tau$. With some analysis, one can easily show that Φ undergoes a linear growth as $\Phi = \kappa y/L_v$ near the surface (L_v being a constant). In the buffer layer, one can similarly formulate $\Phi = \kappa y/L_{bl}$ with L_{bl} increasing super linearly with y to cause the peak followed by a decrease as one approaches the inertial sublayer. In the inertial

layer, $\Phi = \kappa y/L_{il}$ with L_{il} varying linearly with y as per law of the wall (resulting in Φ and γ assuming constant values).

In this context, we see that as the friction velocity, u_τ increases with ζ (see Table 2.1), the viscous length scale, L_v decreases resulting in faster growth of $\Phi = \kappa y/L_v$ in the viscous layer, but over a smaller height that scales with L_v. This is consistent with figures III.4(a) and III.4(b) which show that the magnitude of the peak at the viscous-buffer layer transition decreases with increase in ζ. In addition, we observe an upward (rightward) shift in the log region (i.e. region of nearly constant Φ and γ) with ζ. Taken together, the above observations, namely the upward shift in the log region (figure III.4(a)) and the smaller peak in Φ with increase in ζ, indicate that the buffer layer becomes increasingly thicker for steeper waves. The 'buffer layer' is known as a region of high turbulence production (Pope, 2001) where both the viscous and Reynolds stresses are significant. Therefore, the expansion of the buffer layer with ζ is a consequence of the turbulence production zone expanding due to the wavy surface. This is evident from figure 3.5 where the decay in turbulence kinetic energy (TKE) production is slower for higher ζ in the buffer region ($y^+ \approx 10 - 50$) in both inner-scaled (figure III.5(a)) and dimensional (figure III.5(b)) forms. We expect this trend to be even stronger in the presence of significant separation at larger values of ζ. This trend is consistent with prevalent understanding of classical rough wall boundary layers at high Reynolds numbers, especially in the lower atmosphere where the roughness elements of size $a^+ \gtrsim 50 - 100$ tend to completely destroy the viscous layer (Jiménez, 2004) if not most of the buffer layer. In our studies, $a^+ \approx 13$ for the different ζ (see Table 2.1) and only modulates the buffer layer. A related observation is that the vertical location of the inner scaled peak turbulence production ($y^+ \approx 12$) does not change with ζ, but the magnitude decreases. This is not surprising as for $\zeta > 0$, there exists other sources of turbulence generation, i.e. from the surface roughness or undulations which contributes to the total friction.

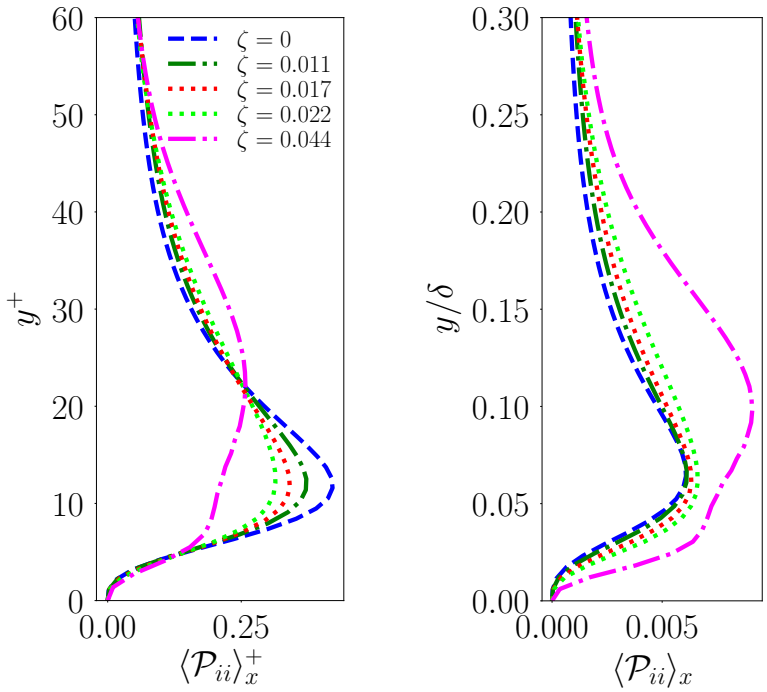

(a) (b)

Figure 3.5: Schematic illustrating the wall-normal variation of streamwise averaged production of turbulent kinetic energy in (a) inner variable non-dimensionalized and (b) dimensional (m^2/s^3) forms.

3.4 Characterization of Reynolds Stress Tensor and its Production

In the earlier discussions, we focused on the mean gradients and their impact on the horizontal flow stresses. In this section, we focus on the effect of changing ζ on elements of the Reynolds stress tensor and the turbulent kinetic energy that are borne out of the interaction between mean gradients and the Reynolds stress. We observed earlier (figure 3.4) that the peak in the mean gradients at the start of the buffer layer decreases with surface undulations which also impacts turbulence production (figure 3.5) in the lower buffer layer and in turn the individual components of the streamwise averaged Reynolds stress tensor, $\langle u_i' u_j' \rangle_{x,z,t}$.

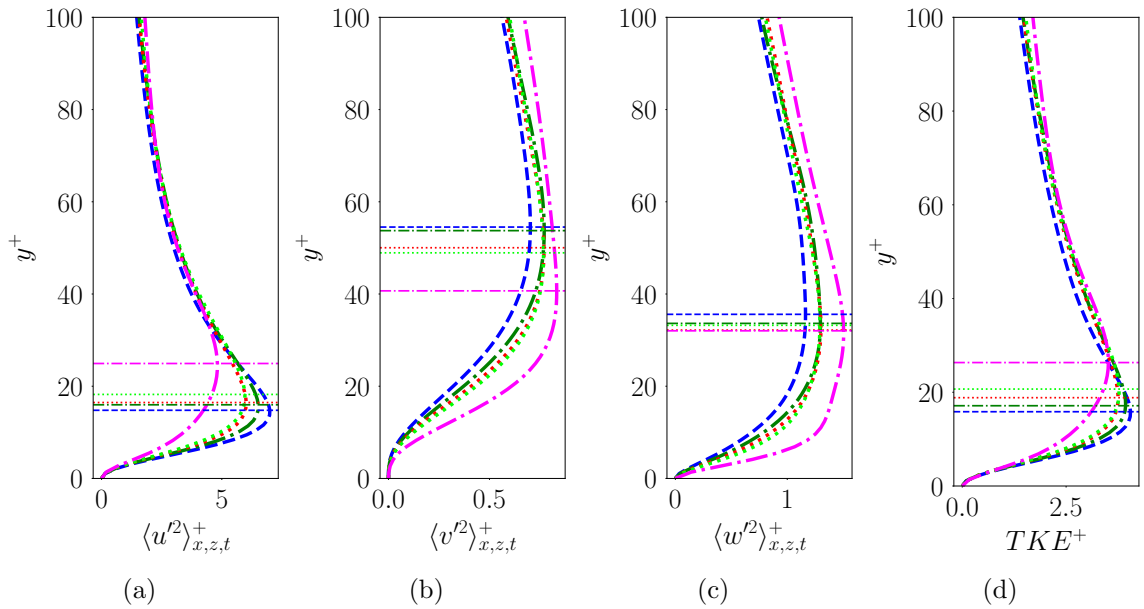

Figure 3.6: Inner scaled mean (a) streamwise variance, (b) vertical variance, (c) spanwise variance and (d) turbulent kinetic energy (TKE). The horizontal lines correspond to height with maximum value of the statistics along the profile.

3.4.1 Streamwise Variance

In fact, the most noticeable deviations from equilibrium in wavy wall turbulence occur in the second order statistics. In particular, we observe in figure III.6(a) the inner-scaled streamwise variance that peaks in the buffer layer and this peak value decreases with increase in ζ. In addition, the inner scaled profiles nearly collapse in the outer region for all ζ while the location of peak streamwise variance shifts upward as ζ increases. Given the lack of significant flow separation, this upward shift in the peak variance is modest, but noticeable. In figure 3.6 we identify the peak location for each curve with color matched horizontal lines so that the trends can be identified. Using this, we see a systematic upward shift of the peak value of $\langle u'^2\rangle^+_{x,z,t}$ with ζ in figure III.6(a). Related research by Ganju et al. (2019) has shown that this upward shift is tied to significant increases in roughness scale, a^+ which can cause very different dynamics around the wave including flow separation. Further, the effect of changing λ was reported to be minimal in their investigation. Their

first observation is consistent with classical understanding of high Reynolds number rough wall turbulence (Pope, 2001; Jiménez, 2004) where the peak variances occur at nearly the roughness height, a. In fact, wall stress boundary conditions for large eddy simulation over rough surfaces are designed to model the same. In our study, the amplitude, a is fixed while the wavelength, λ is decreased in order to change $\zeta = 2a/\lambda$. For a fixed bulk Reynolds number, the decrease in λ (or increase in ζ) increases the net drag and in turn the friction velocity, u_τ. The resulting decrease in the viscous length scale, $L_v = \frac{\nu}{u_\tau}$ changes the inner-scaled wave height, $a^+ = a/L_v$ rather modestly from $13.07 - 15.82$ when ζ increases 4 times from 0.011 to 0.044 (see Table 4.1). Therefore, this systematic upward shift in the location of peak streamwise variance cannot be solely attributed to these very modest increases in a^+. In fact, the wave steepness significantly impacts the buffer layer dynamics and in turn the variance distribution through the turbulence production mechanisms as delineated under.

We further dissect the above observations using the variance production (figure 3.7) term $\langle P_{11} \rangle_x$, in the Reynolds stress transport equation. Note that we further split this component variance production into its dominant contributions, $\langle P_{11}^{u'u'} \rangle_x = \langle \langle u'u' \rangle_{z,t} d\langle u \rangle_{z,t}/dx \rangle_x$ and $\langle P_{11}^{u'v'} \rangle_x = \langle \langle u'v' \rangle_{z,t} d\langle u \rangle_{z,t}/dy \rangle_x$ as shown in figures III.7(b) and III.7(c) respectively. Details on the computation of the production terms can be found in appendix C. We clearly observe that the inner-scaled streamwise variance production due to interaction of the scaled mean shear (i.e., inner-scaled vertical gradient of the mean horizontal velocity, $d\langle u \rangle^+_{z,t}/dy^+$) with the vertical momentum flux ($\langle u'v' \rangle_{z,t}$) denoted by $\langle P_{11}^{u'v'} \rangle^+_x$ clearly peaks in the buffer layer ($y^+ \approx 11 - 15$ as seen in figureIII.7(c)) and this peak shifts upward (with minimal change in magnitude) for increasing ζ. This trend can be interpreted through figures III.9(a) and III.9(c) representing the double averaged profiles of normalized covariance, $\langle u'v' \rangle^+_{x,z,t}$ and mean gradient, $d\langle u \rangle^+_{z,t}/dy^+$ respectively. It is to be noted that $\langle u'v' \rangle^+_{x,z,t}$ peaks at the edge of the buffer layer at $y^+ \approx 32$ whereas the normalized mean gradient, achieves its

maximum value near the surface. In addition, the location of the peak in $\langle u'v' \rangle^+_{x,z,t}$ (at $y^+ \approx 32$) shows very little variation with no clear trend, but its magnitude increases with ζ all through the buffer and log layers. Contrary to this, the magnitude of $d\langle u \rangle^+_{z,t}/dy^+$ decreases with ζ due to surface undulations whose influence decreases away from the surface (through the viscous and buffer layers). In summary, we understand that the combined influence of the surface-induced trends in $\langle u'v' \rangle^+_{x,z,t}$ and $d\langle u \rangle^+_{z,t}/dy^+$ yields the trends observed for $\langle P^{u'v'}_{11} \rangle^+_x$ as shown in figure III.7(c) with peak values occurring over $y^+ \approx 11 - 15$ for different ζ. In addition, the surface undulations play a secondary role in the variance transport (see figureIII.7(b)) with significant production in the roughness sublayer ($y^+ \lessapprox a^+$) followed by destruction above the roughness scale, a^+ that decays with height. This production and destruction process clearly represents deviation from equilibrium as its origins lie in the streamwise mean velocity gradient, $d\langle u \rangle_{z,t}/dx$ being non-zero from horizontal inhomogeneity. A key consequence of this inhomogeneity driven destruction process is that both the peak inner-scaled variance production and the peak variance decrease with ζ (figure III.6(a)). However, it also turns out that the systematic upward shift observed for the peak in $\langle P^{u'v'}_{11} \rangle^+_x$ is non-existent for the $\langle P_{11} \rangle^+_x$ profiles (the peak occurs at or around $y^+ \approx 12$) shown in figure III.7(a). In summary, we observe that more severe the surface inhomogeneities, smaller the rate of streamwise turbulence production through $d\langle u \rangle^+_{z,t}/dy^+$, $d\langle u \rangle^+_{z,t}/dx^+$ and $\langle u'v' \rangle^+_{x,z,t}$, but the location of peak production in wall coordinates remain unaffected. Therefore, the observed upward shift in the peak of $\langle u'^2 \rangle^+_{x,z,t}$ (figure III.6(a)) should arise from other turbulent transport mechanisms including return to isotropy.

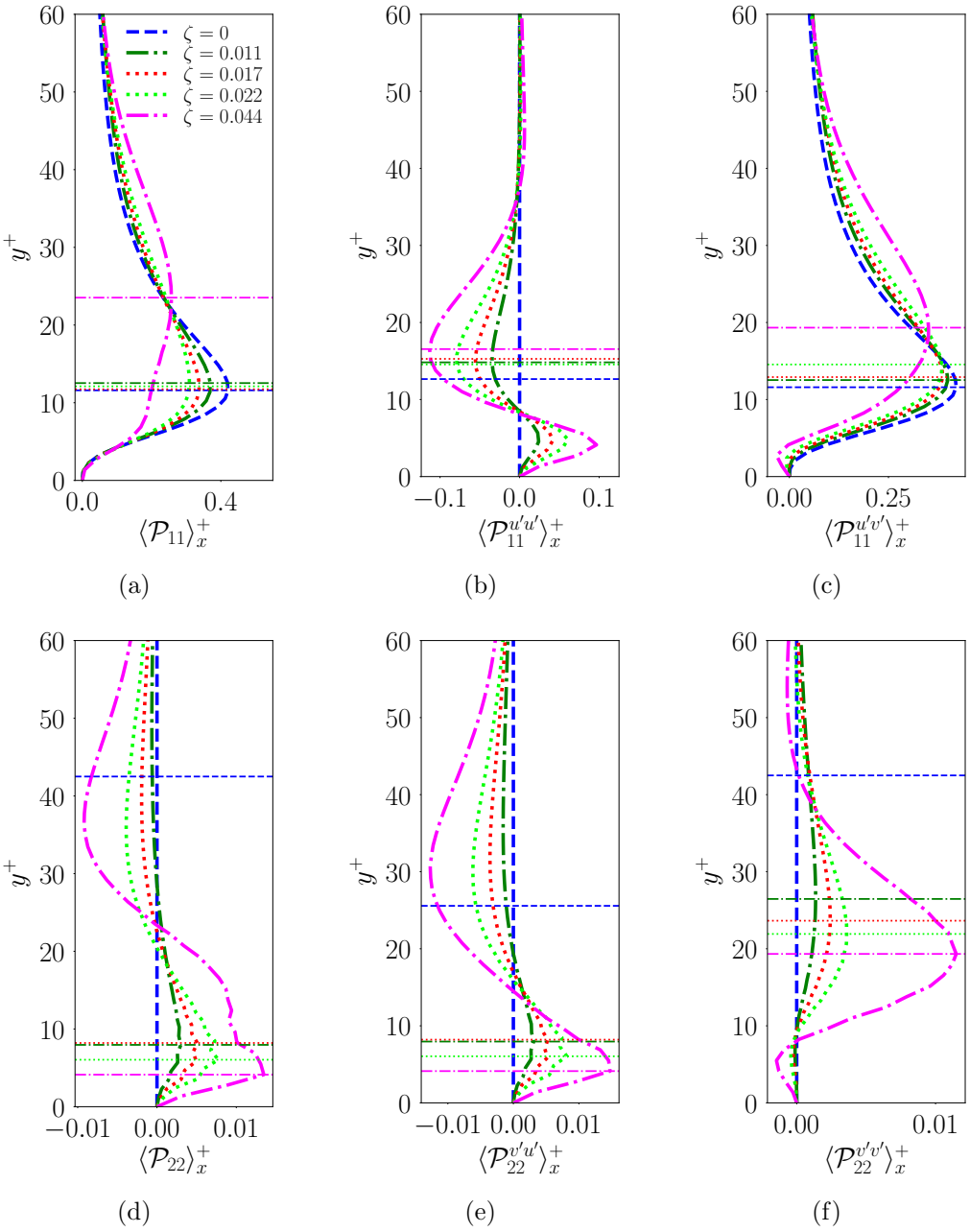

Figure 3.7: Schematic illustration of the wall-normal variation of inner-scaled double averaged production of streamwise (a,b,c) variance, $\langle P_{11} \rangle_x^+$ and vertical (d,e,f) variance, $\langle P_{22} \rangle_x^+$. In each row, we further split the corresponding production terms into $\langle P_{11}^{u'u'} \rangle_x^+$ (b), $\langle P_{11}^{u'v'} \rangle_x^+$ (c), $\langle P_{22}^{v'u'} \rangle_x^+$ (e) and $\langle P_{22}^{v'v'} \rangle_x^+$ (f) respectively. The horizontal lines correspond to the vertical location of maximum value for a chosen statistic. If the peak locations are different, we color match the horizontal lines with the corresponding curves.

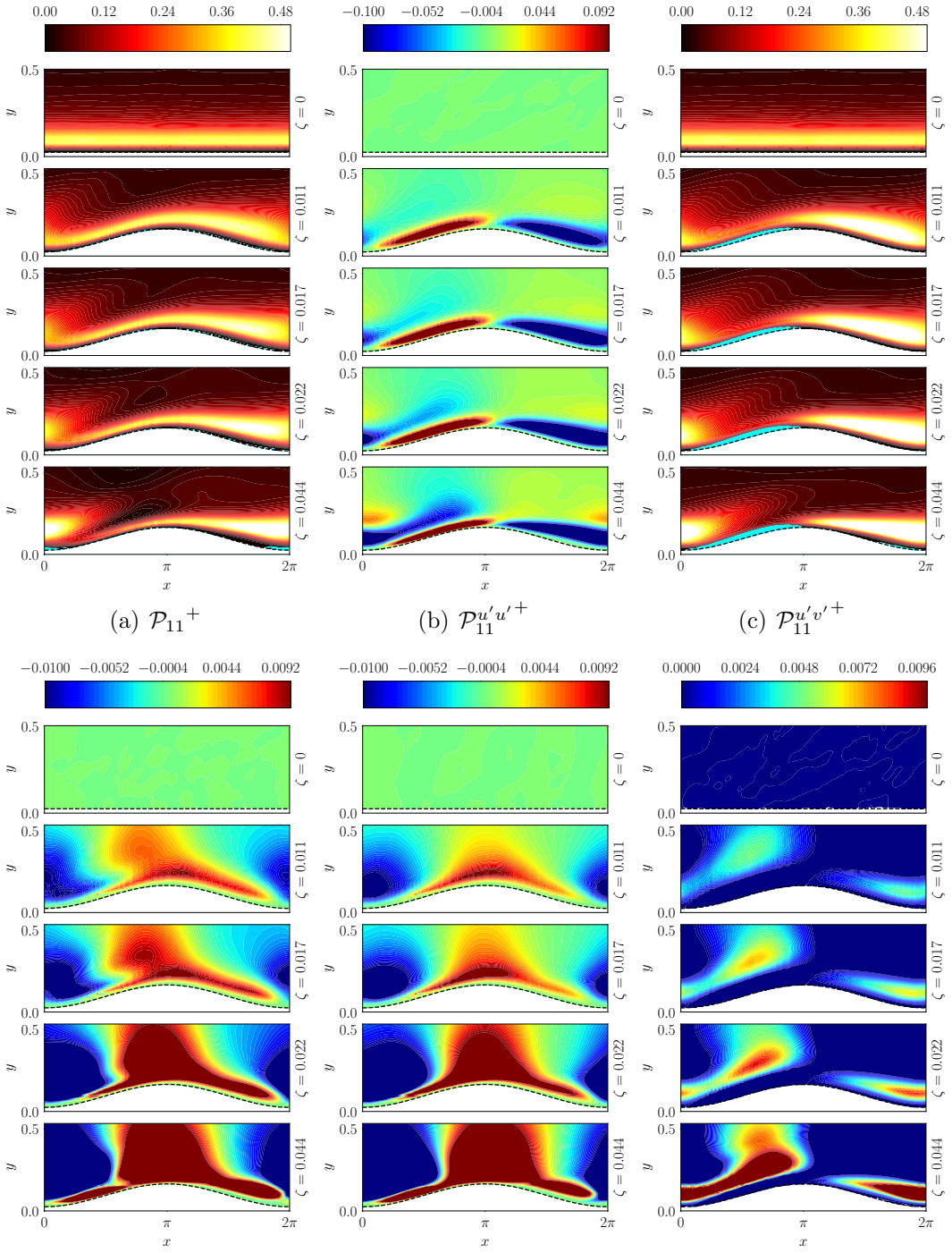

(a) $\mathcal{P}_{11}{}^{+}$ (b) $\mathcal{P}_{11}^{u'u'}{}^{+}$ (c) $\mathcal{P}_{11}^{u'v'}{}^{+}$

(d) $\mathcal{P}_{22}{}^{+}$ (e) $\mathcal{P}_{22}^{v'u'}{}^{+}$ (f) $\mathcal{P}_{22}^{v'v'}{}^{+}$

Figure 3.8: Inner scaled mean production contours

3.4.2 Vertical Variance

The effect of surface undulations on vertical variance profiles is opposite to that

observed for the streamwise variance, i.e. the peak variance in the buffer-log transition region ($y^+ \approx 55$) increase and shift downward with ζ in comparison to flat channel turbulence data. While the shift in the peak location is systematic, we note that the peak value in itself changes very little from $\zeta = 0.011$ to 0.022 after making a sharp jump from $\zeta = 0.0$ to 0.011 and exhibits another jump from $\zeta = 0.022$ to 0.044. It is well known (Pope, 2001) that streamwise turbulent fluctuations are generated closer to the surface in the buffer layer and is then distributed to the other components through the pressure-strain term (Lumley and Newman, 1977). Consequently, the vertical and spanwise variances peak further away from the surface, closer to the log layer. Among the two, the vertical variance is nominally expected to achieve maximum value further away from the surface due to the wall effect, i.e. vertical fluctuations are damped closer to the wall. In our investigations, the vertical variance peaks closer to the log layer ($y^+ \approx 55$) while the spanwise variance peaks lower in the buffer-log transition ($y^+ \approx 35$) as observed in figures III.6(b) and III.6(c) respectively.

Due to the presence of surface undulations (non-zero ζ), vertical velocity variance is produced closer to wall (or effective wall for wavy surfaces) in the roughness sublayer (i.e $y^+ \lesssim a^+$) as seen from the inner-scaled vertical variance production, $\langle P_{22} \rangle_x^+$ in figure III.7(d). The extent of near surface production increases with wave steepness, ζ. To dissect further, $\langle P_{22} \rangle_x^+$ is further split into $\langle P_{22}^{v'u'} \rangle_x^+ = \langle \langle v'u' \rangle_{z,t} d\langle v \rangle_{z,t}/dx \rangle_x^+$ and $\langle P_{22}^{v'v'} \rangle_x^+ = \langle \langle v'v' \rangle_{z,t} d\langle v \rangle_{z,t}/dy \rangle_x^+$ as shown in figures III.7(e) and III.7(f) respectively. The dominant variance production originates from non-zero streamwise gradient of vertical velocity (see figure III.2(b)) which is positive below the roughness scale and negative above it. Consequently, the surface imhomogeneity driven non-zero mean vertical flow over the wavy surface impacts turbulence production by generating vertical variance below the roughness scale and destroying some of it above in the buffer layer (figure III.7(e)). Therefore, unlike flat channel turbulence, return to isotropy is accelerated with increase in ζ causing $\langle v'^2 \rangle_{x,z,t}^+$ to grow faster (figure III.6(b))

through the viscous and buffer layers to ultimately peak closer to the surface (in the buffer-log transition). The location of peak vertical variance is illustrated in figure III.6(b) through coloured horizontal lines that show a clear downward shift from $\zeta = 0 - 0.044$. In essence, what we are observing is that changes in λ with fixed a impacts the growth rate in the buffer layer with perceptible effect on the peak location and magnitude. This trend is maintained until strong separation related dynamics including detachment of the shear layer sets in at higher ζ. As shown in Ganju et al. (2019), this causes a secondary peak in the buffer layer for both vertical and spanwise variance, possibly due to turbulence production within the separation bubble as well as above it. Such effects are absent in the current study as evidenced by just a single peak for the vertical variance production for at least the cases up to $\zeta = 0.022$. However, the jump of the profile from $\zeta = 0.022$ to $\zeta = 0.044$ hints the incipience of the secondary peak due to the onset of separation bubble.

We would like to report that small noise is generated very close to the wall for the vertical velocity due to the effect of immersed boundary method employed in presence of streamwise undulation. Although this noise is ignorable for vertical variance, while multiplied with the Reynolds stress term it partially contributes for the visible discontinuities in the overall vertical variance production structure as in figure III.7(d). This small noise can be avoided by clustering the grid more near the wall. However, as the conclusion of our analysis is not expected to be influenced by this slight numerical deviation, we decided to not go through further clustering which would raise the computational cost and also make the derivative calculation in the clustered region erroneous.

3.4.3 Spanwise Variance

Similar to $\langle v'^2 \rangle^+_{x,z,t}$, the inner-scaled spanwise variance, $\langle w'^2 \rangle^+_{x,z,t}$ also shows stronger growth (see figure III.6(c)) through the viscous and lower regions of the buffer layer to

ultimately peak in the buffer layer ($y^+ \approx 35$). Intriguingly, we note a systematic shift in the peak location and magnitude only for $\zeta = 0.0$ to 0.011 and $\zeta = 0.022$ to 0.044, but little variation from $\zeta = 0.011$ to 0.022. This may be attributed to the peak occurring farther away from the surface where the inhomegeneity effects are small. As we are dealing with mildly steep two-dimensional wavy surfaces in this study, we observe that $\langle w'^2 \rangle_{x,z,t}$ is not produced near the surface as evidenced by the production terms in the variance transport equation (not shown here) being nearly zero throughout the boundary layer due to $d\langle w \rangle_{z,t}/dx = d\langle w \rangle_{z,t}/dy = 0$. In spite of the quasi-two-dimensional wavy surfaces employed here, the above trends will breakdown in the presence of strong separation that can introduce three-dimensional flow patterns. As part of an ongoing research study we are exploring higher values of ζ to verify the above statement.

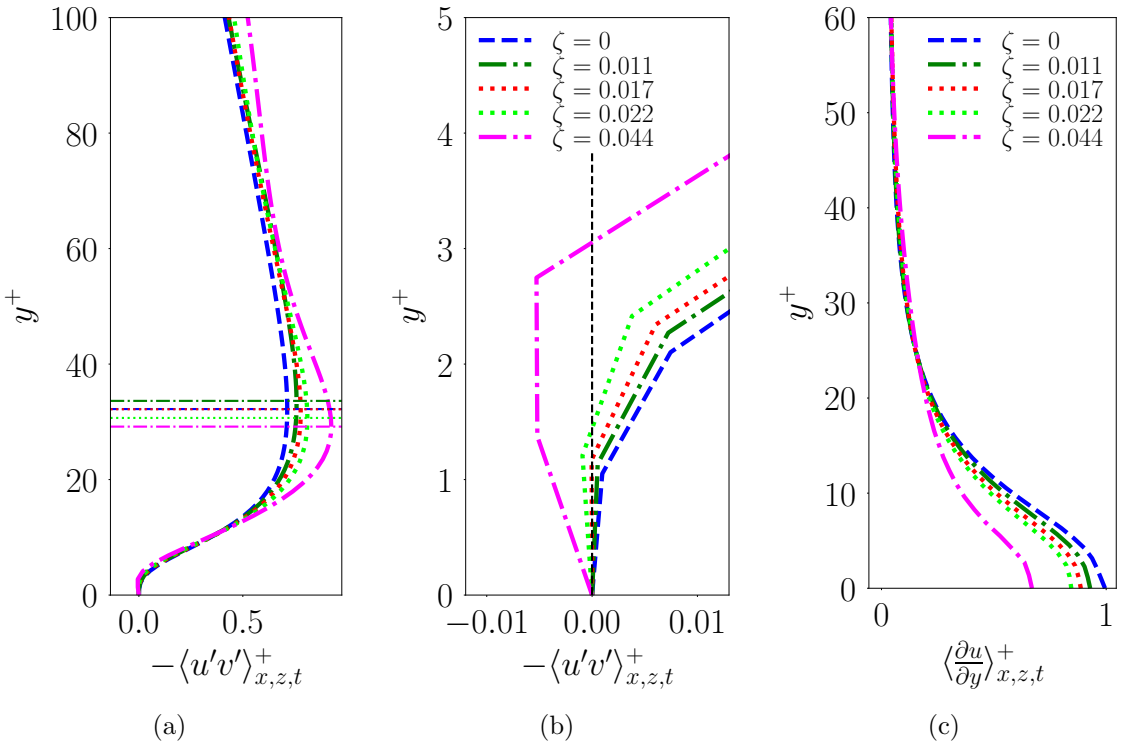

Figure 3.9: Inner scaled mean (a) covariance $\langle u'v' \rangle^+_{x,z,t}$, (b) covariance $\langle u'v' \rangle^+_{x,z,t}$ (zoomed near the surface) and (c) vertical gradient of streamwise velocity, $d\langle u^+ \rangle_{x,z,t}/dy^+$. The black horizontal line corresponds to the average of the maximum magnitude of $\langle u'v' \rangle^+_{x,z,t}$ for the different ζ. Note that the individual peak values were too close to each other to be shown separately.

In the absence of three-dimensional flow (both forced by a three-dimensional surface and induced by separation over a two-dimensional surface), the location of peak $\langle w'^2 \rangle^+_{x,z,t}$ shows no clear monotonic trend although a consistent downward shift is observed for $\zeta > 0$ for up to $\zeta = 0.022$. This can be attributed to either the small amounts of separation observed in these flows (see figure 3.1) or due to conversion of the vertical variance produced from the surface undulation through the pressure-strain term. We expect the latter to be the likely mechanism although no quantification is provided work to support this hypothesis. However, for $\zeta = 0.044$, a downward shift of the peak location is evident that can be attributed to the onset of consistent separation bubble. As one would expect away from the surface, the $\langle v'^2 \rangle^+_{x,z,t}$ and $\langle w'^2 \rangle^+_{x,z,t}$ profiles across different values of ζ approach each other in the outer layer indicating that the effect of the surface undulations is concentrated closer to the surface. We nevertheless note that in this region of the TBL, $\langle v'^2 \rangle^+_{x,z,t}$ (figure III.6(b)) and $\langle w'^2 \rangle^+_{x,z,t}$ (figure III.6(c)) are slightly higher for non-zero ζ when compared to the flat channel with $\zeta = 0$.

3.4.4 Mean Turbulent Kinetic Energy

The mean inner scaled turbulent kinetic energy, TKE^+, displays the cumulative effect of the individual variances as shown in figure III.6(d). In particular, we observe an exaggerated upward shift (note the horizontal lines in figure III.6(d)) in the location of peak k^+ in the buffer layer. This is caused by the combined effects of the upward shift in $\langle u'^2 \rangle^+_{x,z,t}$ along with the downward shifts in both $\langle v'^2 \rangle^+_{x,z,t}$ and $\langle w'^2 \rangle^+_{x,z,t}$. Beyond the peak, the different curves nearly collapse in the outer layer although in the inertial logarithmic region, TKE^+ shows consistently higher values for the wavy turbulence cases due to systematically higher $\langle v'^2 \rangle$ and $\langle w'^2 \rangle$ for $\zeta > 0$.

3.4.5 Vertical Turbulent Momentum Flux

In addition to the diagonal components of the Reynolds stress tensor discussed above, we also look at the dominant off-diagonal terms, namely, $-\langle u'v' \rangle^+_{x,z,t}$ and $-\langle w'v' \rangle^+_{x,z,t}$ as shown in figure 3.9. In the limit of high Reynolds number (i.e $Re_\tau \geq 4000$), for channel flow turbulence over smooth flat surfaces, there exists a well defined log layer with nearly constant $\langle u'v' \rangle^+_{x,z,t}$ (Lee and Moser, 2015). This nearly constant $\langle u'v' \rangle^+_{x,z,t}$ layer is very narrow at low Reynolds numbers. Nevertheless, this study still lets us characterize the influence of the wavelike undulation on the turbulence structure. As discussed earlier, the location of the peak in $\langle u'v' \rangle^+_{x,z,t}$ (at $y^+ \approx 32$) shows very little variation with no clear trend, but its magnitude increases with ζ. The peak location in $\langle u'v' \rangle^+_{x,z,t}$ falls roughly between the peak values of $\langle u'^2 \rangle^+_{x,z,t}$ and $\langle v'^2 \rangle^+_{x,z,t}$ as shown in figures III.6(a) and III.6(b). This increase in peak value is not surprising as the wavy surfaces naturally generate (figures III.7(a) and III.7(d)) stronger u' and v' fluctuations. As shown in figures III.9(a) and III.9(b), increase in the positive peak of $-\langle u'v' \rangle^+_{x,z,t}$ is correlated with a small negative peak in the viscous layer at higher values of ζ, indicative of the surface shape induced mixing that is different from turbulence induced stress. This negative value of $-\langle u'v' \rangle^+_{x,z,t}$ close to the surface indicate that higher momentum fluid particles move away from the wall due to up slope part of the wavy surface.

CHAPTER IV

Roughness Characterization

4.1 Characterization of the Roughness Function and Roughness Scales

A common way to assess the influence of the wavy surface on turbulence structure is to quantify the effective drag and its influences on the flow structure. While the increase in friction velocity for a fixed Re_b (apparent from Table 2.1) is a natural way to quantify the increased drag, estimating the downward shift in the mean streamwise velocity profile (figure III.2(a)) is another approach and often used to characterize the effective roughness scales. It is well known that the logarithmic region in the equilibrium flat channel turbulent boundary layer (TBL) is given by

$$\langle u \rangle^+_{x,z,t} = \frac{1}{\kappa} ln(y^+) + B \tag{4.1}$$

where the additive constant B is typically estimated to fall within the range, $\approx 5.0 - 6.0$ and depends on the details of the buffer and viscous layer for a given simulation or measurement. The flat channel data in the current work provides an estimate of ≈ 5.6, possibly due to a combination of the friction Reynolds number regime and simulation algorithm. In the presence of surface undulations of scale a, we observed from the earlier discussion that the log region underwent a upward shift due to an expanding buffer layer. As per Hama (1954); Jiménez (2004); Flack and Schultz (2014), the influence of these buffer layer modulations on the log layer shift is characterized in terms of a modified logarithmic profile for rough-wall turbulent boundary layers

(TBLs),

$$\langle u \rangle^+_{x,z,t} = \frac{1}{\kappa} ln(y^+) + B - \Delta\langle u \rangle^+_{x,z,t} \tag{4.2}$$

where $\Delta\langle u \rangle^+_{x,z,t}$ is defined as the roughness function. The roughness function, $\Delta\langle u \rangle^+_{x,z,t}$ can be related to the characteristic "equivalent" sand grain roughness, k_s as

$$\Delta\langle u \rangle^+_{x,z,t} = \frac{1}{\kappa} ln(k_s^+) + B - 8.5, \tag{4.3}$$

and the characteristic roughness length, k_0 as

$$\Delta\langle u \rangle^+_{x,z,t} = \frac{1}{\kappa} ln(k_0^+) + B. \tag{4.4}$$

It is easily seen that $k_0 = k_s e^{-8.5\kappa}$. While k_s and k_0 are used to quantify the non-equilibrium 'roughness' effects near the surface, they mostly cater to complex roughness such as grasslands, urban canopies or sand grain type surfaces. Of course, k_s corresponds to a case where the buffer layer dynamics is significantly modified by the roughness while k_0 corresponds to a situation where the buffer and. viscous layers are completely destroyed by the roughness. Therefore, such metrics do not represent the smooth, low steepness surfaces adopted in this work. Table 4.1 compiles estimates of the roughness function, $\langle \Delta\langle u \rangle^+_{x,z,t} \rangle_y$, averaged over the entire logarithmic region given by $y^+ \approx 60 - 120$ as illustrated in figure IV.1(d) over which the values are nearly constant. For all the metrics reported in this work, we use data from the averaged profiles across constant values of the non-scaled local coordinate, $y_{local,1}$.

For comparison sake, we also report the equivalent sand grain roughness, k_s of Nikuradse (1950) and the characteristic roughness length, k_0 scaled by the inner-layer variables for different values of ζ. As expected, these different roughness metrics increase linearly with wave steepness as seen in figures IV.1(a)-IV.1(c). The effective

sand grain roughness assumes a non-zero value of ≈ 3.3 for $\zeta = 0$ due to the upward shift caused by the viscous and buffer layers. Therefore, $k_s^+ \approx 4$ is indicative of a nearly smooth wall which in our study corresponds to $\zeta \sim 0 - 0.01$. The higher values of ζ considered in this work generate $k_s^+ \sim 6$ although no substantial flow separation is observed for up to $\zeta = 0.022$. However, for $\zeta = 0.044$, $k_s^+ \sim 14$ which can be partially attributed to the increased friction Reynolds number. As expected, the k_0^+ is extremely small indicating that the flow is smooth enough to retain the viscous and buffer layers.

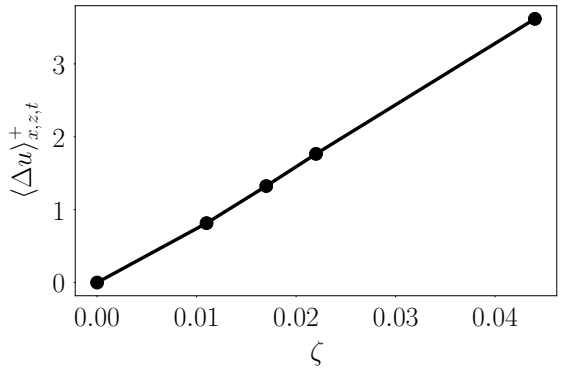

(a) Mean roughness function variation with wave steepness.

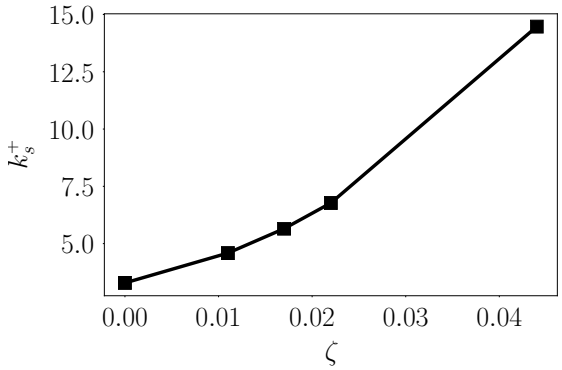

(b) Equivalent sand grain roughness variation with wave steepness.

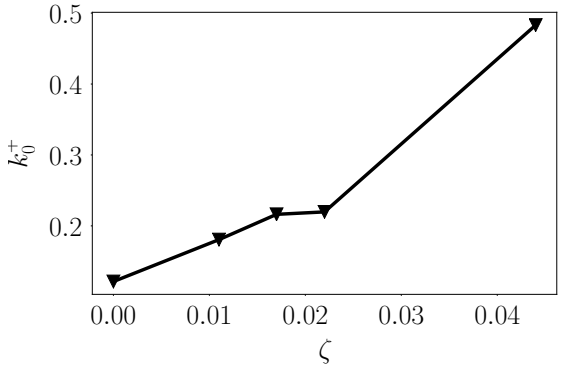

(c) Characteristic geophysical roughness length variation with wave steepness.

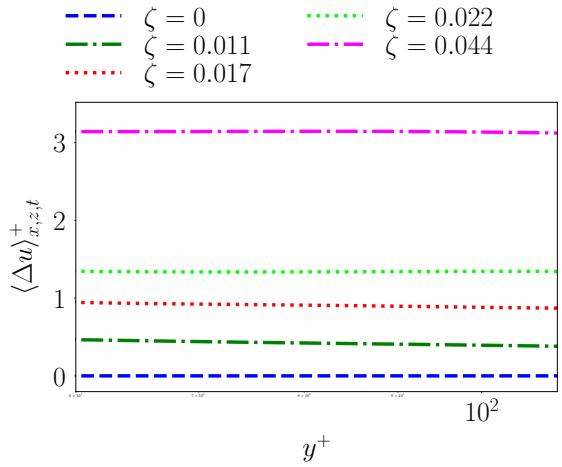

(d) Roughness function variation in the log region.

Figure 4.1: Variation of the different roughness quantifications with ζ in (a), (b), (c) and wall normal variation of mean roughness function in (d).

Given that a^+ is nearly constant for all the cases while k_s^+ and k_0^+ show near

linear growth confirm that such wavy surfaces do not fit the k-type roughness description (Perry et al., 1969; Jiménez, 2004). In addition, given that the boundary layer height in channel flow turbulence is fixed as a constant δ, the independence of $k_s,\ k_0$ on δ indicate a departure from d-type classification (Perry et al., 1969). In fact such surfaces as considered in this work belong to the 'transitional' and 'waviness' regime as $a^+ \sim 13-15$ does not represent a sufficiently large (i.e $O(100)$) roughness Reynolds number, $Re_a = au_\tau/\nu$. We have also reported the λ^+ values for the different cases in Tables 2.1 and 4.1.

$\boldsymbol{\zeta}$	$\boldsymbol{\kappa}$	$\langle\Delta\langle u\rangle^+_{x,z,t}\rangle_y$	k_s^+	k_0^+	$a+$	λ^+
0.000	0.3954	0.0000	3.2838	0.1215	0.0000	∞
0.011	0.3805	0.8150	4.5867	0.1806	13.070	2354
0.017	0.3839	1.3242	5.6514	0.2163	13.480	1618
0.022	0.4033	1.7655	6.7725	0.2197	13.920	1252
0.044	0.4000	3.6174	14.4711	0.4831	15.820	712

Table 4.1: Tabulation of estimated turbulence parameters, namely, von Kármán constants for the different cases and commonly used roughness parameters.

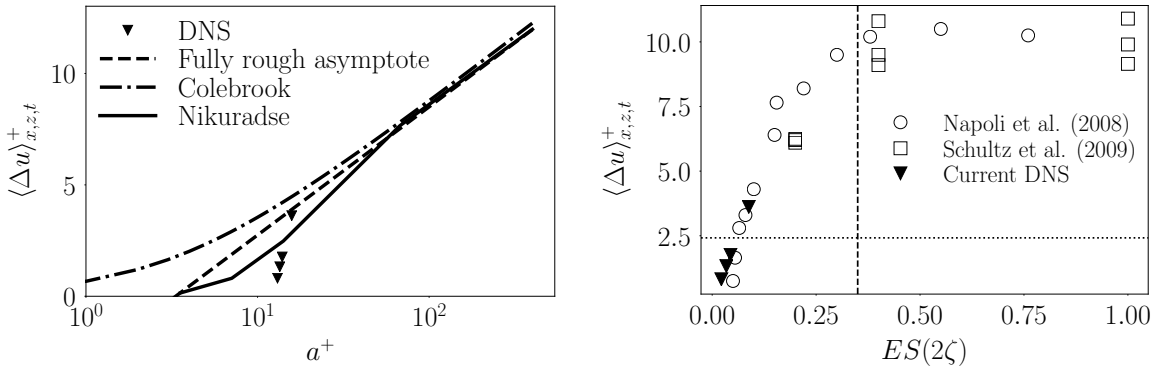

(a) Mean roughness function variation with roughness Reynolds number in comparison with the correlation obtained from the data of Nikuradse (1950), the Colebrook relation (Colebrook et al., 1939) and fully rough asymptote along with the current DNS (See appendix for the correlation equations).

(b) Comparison of variation of mean roughness function with effective slope (ES) reported in Napoli et al. (2008) and Schultz and Flack (2009) with the current DNS.

Figure 4.2: Variation of mean roughness function (a) with roughness Reynolds number and (b) with effective slope in comparison with reported data from known literature.

The 'waviness' regime implies a surface that is very different from a Nikuradse

roughness dominated by form drag caused by flow separation and vortical re-circulation zones within the roughness sublayer. Therefore, strong waviness causes the drag (as estimated by the roughness function $\Delta\langle u\rangle^+_{x,z,t}$) to be smaller than the corresponding Nikuradse value for a given $k^+ = a^+$. At low slopes (waviness) the overall drag is more dominated by viscous shear and less by the form drag. The opposite is true in the roughness regime. This is clearly illustrated in figure IV.2(a) where the correlation between $\Delta\langle u\rangle^+_{x,z,t}$ and $k^+ = a^+$ from Nikuradse (1950) and Colebrook et al. (1939) are compared with our current DNS data. We clearly see that for the current study with nearly constant a^+, $\Delta\langle u\rangle^+_{x,z,t}$ increases with wave steepness ζ to approach the Nikuradse curve. The wave slope dependence on the flow drag is evident from figure IV.2(b) where $\Delta\langle u\rangle^+_{x,z,t}$ is shown against the effective slope, ES= 2ζ. We clearly see that our data follows the trend of Napoli et al. (2008), i.e., $\Delta\langle u\rangle^+_{x,z,t}$ increases with ES until it asymptotes to a value dependent on $k^+ = a^+$ and the flow Reynolds number. This capping value can be estimated somewhat accurately from the Nikuradse curve (Nikuradse, 1950) for sand grain roughness (this value is denoted by the horizontal line in figure IV.2(b) for our DNS data) as the sand grains typically represent a high effective slope surface. However, the data point for $\zeta = 0.044$ in our case is placed above the horizontal line because of increased roughness Reynolds number which corresponds to a slightly higher capping value as suggested by the Nikuradse curve. Figure IV.2(b), also shows the data from Schultz and Flack (2009) who performed experiments with systematically varied pyramid roughness elements of different slope. These data trends indicate that the slope transition from waviness to Nikuradse type roughness regime (denoted by a vertical line in figure IV.2(b)) occurs between $ES \sim 0.25 - 0.4$ ($\zeta \sim 0.12 - 0.18$) with possible dependence on the extent of separation between the surface and outer layer scales (δ/k) and Reynolds number (Re_τ). This transition has been correlated to the dominance of form drag over viscous drag (Schultz and Flack, 2009; Napoli et al., 2008). For the benefit of the reader,

we have explicitly documented the roughness function correlations of Nikuradse and Colebrook used above in Appendix B.

In summary, the modulations in the mean averaged first order statistics from wavy surface undulations manifest as: (i) increase in drag (through friction velocity u_τ); (ii) modified buffer region including (iii) a systematic upward flow in the buffer layer and a smaller downward flow at the lower logarithmic layer. To interpret the above effects better, we analyze the horizontal flow stress and components of the Reynolds stress tensor in the following sections.

4.2 Characterization of Horizontal Flow Stress and Implications to Drag

The horizontal flow stress directly impacts the flow drag through the boundary layer and in turn the mean velocity profiles discussed above. The viscous flow stress $\overline{\tau}_V$ acting on a fluid particle is described including both spanwise and streamwise components as $\overline{\tau}_V = \tau_{xy}^V \hat{i} + \tau_{zy}^V \hat{k}$, where $\tau_{xy}^V = \mu\big(\frac{\partial \langle u \rangle_{x,z,t}}{\partial y} + \frac{\partial \langle v \rangle_{x,z,t}}{\partial x}\big)$ and $\tau_{zy}^V = \mu\big(\frac{\partial \langle w \rangle_{x,z,t}}{\partial y} + \frac{\partial \langle v \rangle_{x,z,t}}{\partial z}\big)$. Similarly, the Reynolds stress is given by $\overline{\tau}_R = \tau_{xy}^R \hat{i} + \tau_{zy}^R \hat{k}$, where $\tau_{xy}^R = -\langle u'v' \rangle_{x,z,t}$ and $\tau_{zy}^R = -\langle w'v' \rangle_{x,z,t}$. The total horizontal stress is then $\overline{\tau}_H = \overline{\tau}_R + \overline{\tau}_V$ with τ_H, τ_R and τ_V without overbars denoting their magnitudes.

Figure IV.3(a) shows the inner-scaled double-averaged horizontal stress magnitude, τ_H felt by a fluid particle. We further split this into the inner-scaled viscous and turbulent parts, τ_V and τ_V respectively as shown in figures IV.3(b) and IV.3(c). In the viscous layer, the total stress is dominated by the viscous stress for the different cases A-E with different ζ varying between $0 - 0.044$. The inner scaled mean viscous shear stress magnitude (figure IV.3(b)) decreases with steepness (figure IV.3(b)) in the viscous layer where it is nearly constant before decreasing across the buffer layer. Away from the mean surface level, in the buffer layer, the inner-scaled Reynolds stress magnitude grows (from near-zero values in the viscous layer) into a peak value at

$y^+ \approx 35$ (figure IV.3(c)) whose magnitude increases with ζ before collapsing over each other in the log layer. Overall, the viscous stress dominates in the viscous layer while the Reynolds stress grows through the buffer layer (a region where the viscous stresses continually decrease in importance) to peak at the buffer-log transition region.

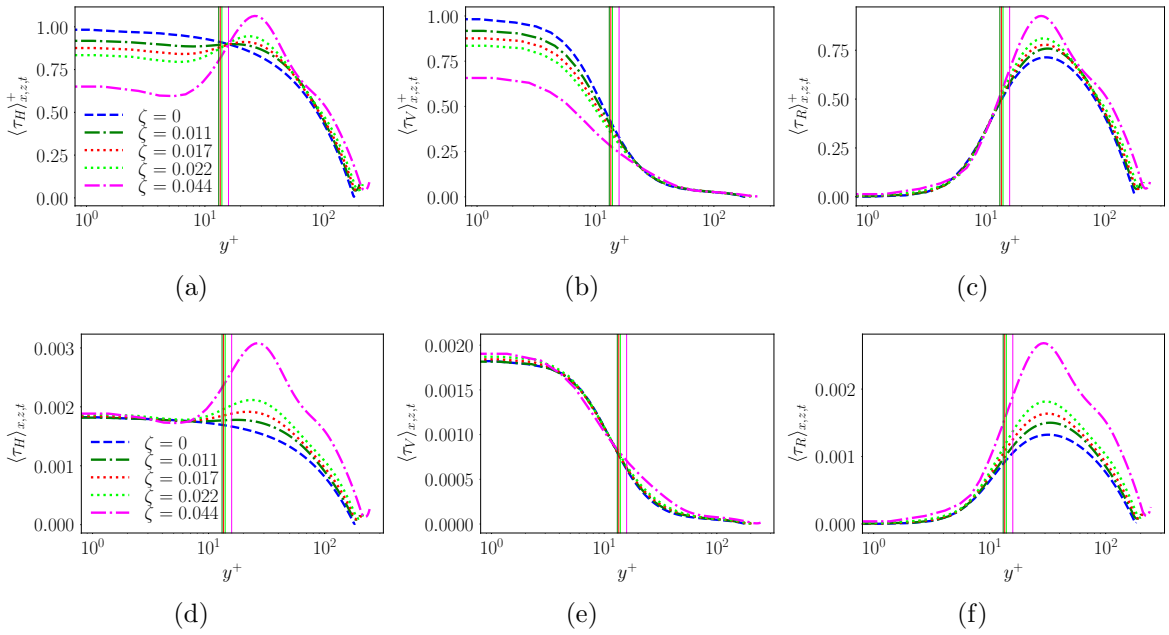

Figure 4.3: The schematic shows the inner scaled mean (a) horizontal stress, (b) viscous stress and (c) Reynolds stress in the top row and the dimensional mean (d) horizontal stress, (e) viscous stress and (f) Reynolds stress in the bottom row. The vertical lines correspond to the different a^+ values.

The decrease in magnitude of the inner-scaled viscous stress with ζ in the viscous and lower buffer layers is a consequence of the normalization using the averaged wall stress, u_τ^2 which increases with wave steepness. We observe that the mean τ_V is relatively unaffected, but its contribution to the total drag decreases with increase in ζ. In general, the mean streamwise flow near the wall slows down due to the presence of wave-like undulations (see figure III.2(a)) which in turn reduces its gradient in the wall normal direction. This reduction in the average viscous stress is compensated by the non-zero vertical velocity and its variation along the streamwise and vertical direction. This explains why the net double-averaged (i.e. both temporally and

spatially averaged) dimensional viscous stress sees very little increase in the viscous layer as seen from the dimensional stress profiles in figure IV.3(e). This observation clearly indicates that the increase in net wall stress (u_τ^2) with ζ has its origins in the increase of Reynolds stress in the buffer-log layer transition as seen in figure IV.3(f) which is reflected in the total mean stress variation as well (figure IV.3(d)). Given that the non-dimensional roughness scale, $a^+ \approx 13 - 15$ corresponds to the buffer layer, it is not surprising that the buffer layer shoulders much of the effect of increasing wave steepness. However, the mechanism underlying increase in the peak double-averaged Reynolds stress with ζ will invariably depend on the structure of the attached (or detached) shear layers in the vicinity of the wavy surface resulting in a coupling between the viscous shear layers and buffer layer turbulence production. The nature of this coupling will be further explored in the future. Of course, when the shears layers are detached as in a separated flow, the interactions could entail very different characteristics which is hinted by the $\zeta = 0.044$ curve showing a major jump from the other four cases. An incipient secondary peak is also observed for this case (figure IV.3(c) and IV.3(f)) in the Reynolds stress profile that can be attributed to the onset of strong separation isolating the different behavior in the roughness sublayer and the shear layer

CHAPTER V

Streamwise Variability and Asymmetric Structure

All of the 1D statistical analysis in the section III and IV to understand different turbulence structure as a function of only vertical distance from the wall are decent yet not complete because of the underlying assumption of streamwise homogeneity. In reality, richer physics is expected to be involved varying in streamwise direction due to the inhomogeneity introduced by the wavy geometry. Ideally we would want to look at 3D structures which would make this analysis too complicated. However, our simulations ensure spanwise homogeneity which allows us to learn the streamwise variability by analyzing only 2D statistical structures. So, we look at the inner scaled spanwise and temporally averaged statistics. Later, we perform a station by station dissection of the local 1D profiles to investigate the origin of the deviation from equilibrium.

5.1 Streamwise Variability of Turbulence Structure

Streamwise velocity for the cases with $\zeta > 0$ is clearly skewed towards the upslope region near the wall as observed in figure V.1(a) indicating the high velocity particles getting rolled over the low velocity particles beyond the wave peaks. This is the dominant horizontal asymmetry that originates in the downslope region beyond the wave peak as the backward facing wall in that region enforces minimum form drag contrary to the symmetric upslope region where the fluid particles near the wall climb up the wave against maximum drag. This conclusion is bolstered looking at the horizontal stress distribution near the wall as in figure V.1(c) that suggests high stress

in the upslope as the frictional drag is added with form drag whereas in the downslope only the viscous shear acts on the fluid. This also hints that the streamwise turbulence production is maximum in the downslope region driving the flow over the next wave as suggested in figure V.2(a). This deviation gets more and more pronounced with increasing *zeta* suggested by the increasingly thicker low velocity region as well as decreasing horizontal stress in the downslope. This behavior whatsoever is limited inside the viscous layer as Reynolds stress starts building away from the wall in the buffer layer and starts dominating the total shear. So in the buffer layer of the flows with undulation, the total shear peaks due to dominant Reynolds stress. Magnitude of the peak increases with increasing steepness of the wave which is consistent with the behavior of Reynolds stress component as shown in figure V.3(a) At $\zeta = 0.044$, we see a negative streamwise velocity bubble built up in the downslope marked by the cyan region indicating the onset of dominant separation.

Vertical velocity on average shows opposite sign in the upslope and downslope of the wave peak as observed in figure V.1(b). The positive skew of the 1D profile in figure III.2(b) can be explained if the dark red $\langle v \rangle^+_{z,t} \gtrapprox +0.30$ and the dark blue $\langle v \rangle^+_{z,t} \lessapprox -0.30$ contour regions are observed closely. Areas enclosed by these two blobs are different in a sense that positive contour region is bigger than the corresponding negative contour region. Therefore, the resulting averaged vertical velocity profile is expected to be skewed into the positive. The reason is uplifting of the fluid particles in the upslope of the wave due to the form drag enforced by the forward facing wave while the downslope is more free for the particles to keep the momentum and climb down as there is no hindrance from the backward facing wall to push the particle downward.

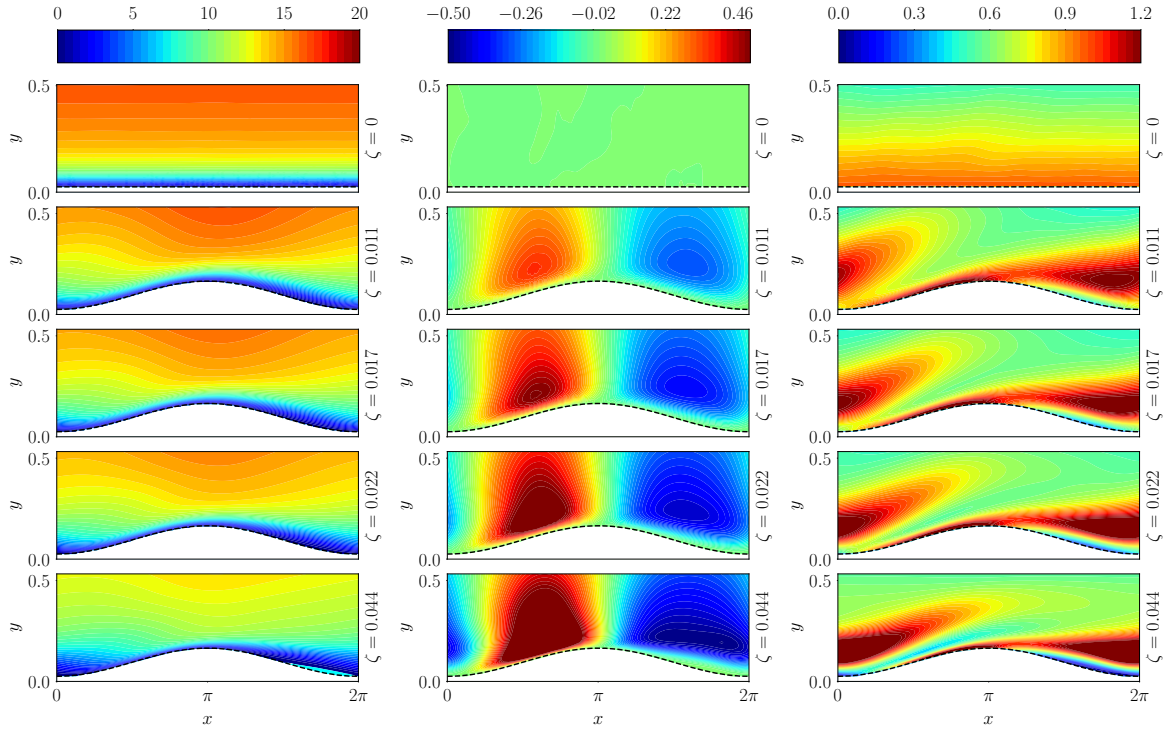

(a) $\langle u \rangle^+_{z,t}$ (b) $\langle v \rangle^+_{z,t}$ (c) $\langle \tau_H \rangle^+_{z,t}$

Figure 5.1: Spanwise and temporally averaged inner scaled (a) streamwise and (b) vertical velocity and (c) horizontal stress

Second order statistics of the cases with $\zeta > 0$ provides major information the behaviors of the distribution of turbulence kinetic energy (TKE). Streamwise variance as in figure V.2(a) decreases significantly with increasing steepness and peaks very near the wall in the buffer region indicated by the dark red region. However the higher streamwise variance region seems to be significantly more pronounced in the downslope region suggesting maximum production of streamwise TKE taking place there. Away from the buffer region this streamwise fluctuation is distributed into vertical and spanwise fluctuation which peaks at the upslope region indicated by the yellow-red region in figure V.2(b) and figure V.2(c) respectively. Unlike streamwise fluctuation, there two components gets stronger with increasing ζ. Therefore, to conclude, the streamwise variance is the major contributing component in the TKE production ($\mathcal{P}$) peaking in the downslope region, which converts using the pressure-strain-rate

term ($\mathcal{R}$) to the vertical and spanwise variance away from the buffer layer peaking in the upslope region. While getting an overall idea on the transport of TKE is a bit complex just by looking at the distribution of individual variance components, the cumulative effect shows clear trend in terms of streamwise variability. As suggested in figure V.3(b), the streamwise position of the maximum TKE shifts from the downslope of the wave to the upslope of the next wave with increased ζ while the magnitude decreases in and averaged sense

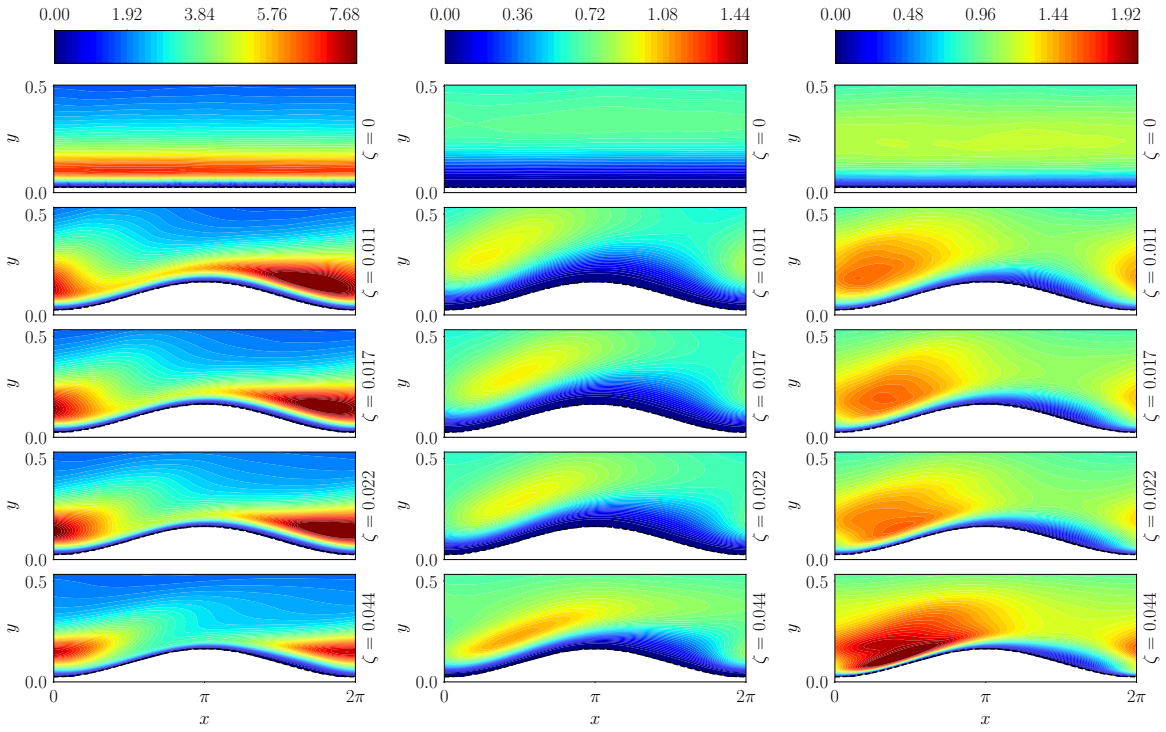

(a) $\langle u'^2 \rangle^+_{z,t}$ (b) $\langle v'^2 \rangle^+_{z,t}$ (c) $\langle w'^2 \rangle^+_{z,t}$

Figure 5.2: Spanwise and temporally averaged inner scaled (a) streamwise, (b) vertical and (c) spanwise variances

Interesting behavior of the shear layer can be identified from the 2D structure of spanwise vorticity in presence of undulation. As we observe from figure V.3(c), we see a thin dark red high negative vorticity region adjacent to the bottom wall in the upslope of the wave crest. But, in the downslope region this structure starts breaking up with increasing ζ signifying the upward motion of the low velocity particles. The higher the

ζ, the earlier the breaking up happens in terms of phase angle. Also, with increasing ζ, beneath that disturbed structure in the downslope low vorticity region starts building up indicating incipient separation as the streamwise gradient of vertical velocity ($\frac{\partial v}{\partial x}$) takes over the dominance of vertical gradient of streamwise velocity ($\frac{\partial v}{\partial x}$) slowly. At $\zeta = 0.044$, the shear layer (i.e. the thin red region) is completely uprooted/detached from the wall, and a cyan positive vorticity region emerges indicating the onset of flow detachment/separation in the downslope.

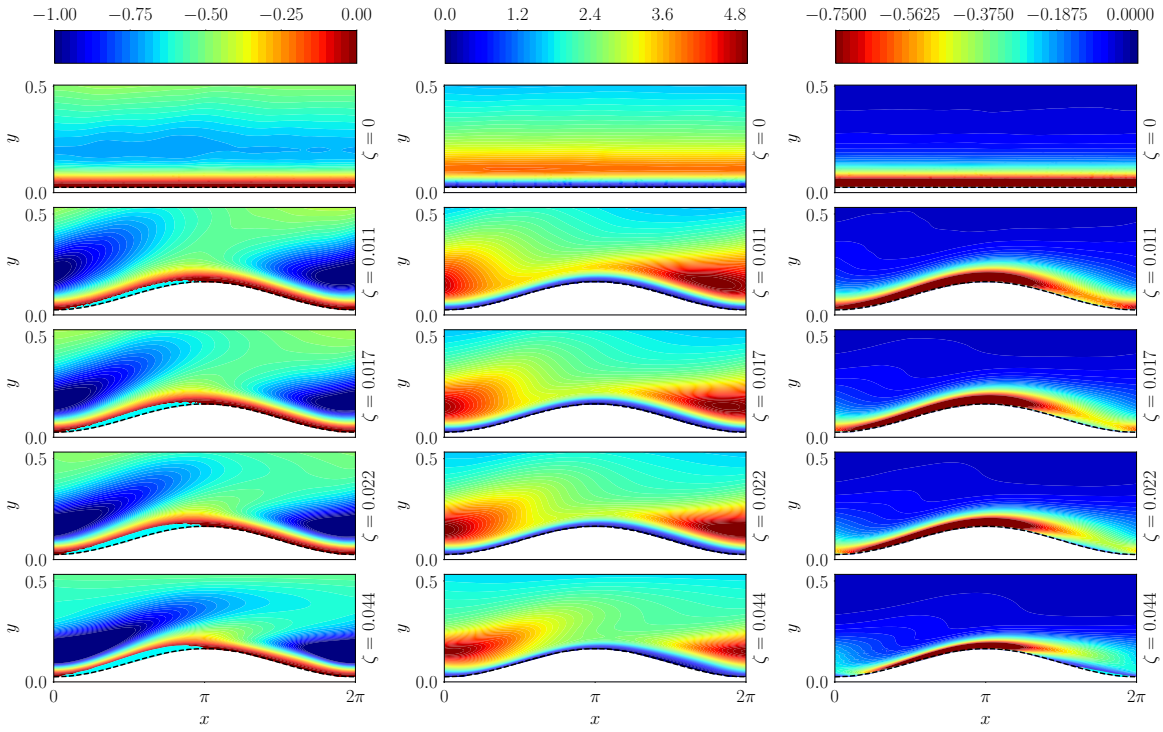

(a) $\langle u'v' \rangle^+_{z,t}$ (b) TKE^+ (c) ω^+_z

Figure 5.3: Spanwise and temporally averaged inner scaled (a) $\langle u'v' \rangle_{z,t}$ co-variance, (b) TKE and (c) spanwise vorticity

This phenomenon can be justified by the well understood fact of attached shear layer for turbulent flow in absence of separation which is true even in presence of undulation when the separation is very little. When closely observed, it can seen that the thin red vortical structure for $\omega^+_z \lessapprox -0.6$ breaks at about $\Delta\phi \approx 0.1\pi$ phase angle unit early in the $\zeta = 0.022$ case compared to the $\zeta = 0.011$ case and it seems to be

completey lifted up by a separation bubble in $\zeta = 0.044$ case.

5.2 Averaging in Fixed Global Coordinate and Inhomogeneity Effect

By far we discussed the 1D profiles of turbulence structure using a streamwise averaging along a vertical co-ordinate that assumes local homogeneity. However, it needs addressing that this averaging along inhomogeneous direction is rather complex if we take into account the streamwise varying physics. In this section we present a different averaging technique that adopts a global coordinate system, y_{global} which is nothing but the co-ordinate system of the actual simulation. In terms of understanding, there are both advantages and disadvantages of this technique. This method limits the sampling rate of ensemble averaging at y-levels below the peak of the wavy surface as the effective fluid region reduces with height. However, we expect this effect to minimally impact the results due to temporal averaging across nearly 2500 snapshots to approximate the statistics. We set the mean height of the wave to be $y_{global} = 0$ and render the $y_{global} < 0$ to be the lower half of the roughness sublayer. Nevertheless, the motivation behind computing such streamwise averaged statistics is to clearly isolate the dynamics of the flow in the roughness layer, shear layer and free boundary layer (BL). Because in reality we do not get locally smooth structured undulation where we can deal with every streamwise station in the streamwise direction individually to compute different vertical coordinates. In addition such measures represent practical data acquisition where sensors are fixed at uniform altitudes.

In figure 5.4, some of the major first and second order quantities are presented as a function of y_{global}. To start with, the most noticeable difference in the profiles compared with the conventional averaging is the sharp jump exactly at the roughness height a^+ (represented by the horizontal lines color matched with the 1D profile for each case) for all the cases with $\zeta > 0$. This can be interpreted as the sudden change in the physical behavior above the peak of the wave in an averaged sense. This

measurement is also useful to identify three different region of the turbulence structure based on vertical height from the wall:

i Roughness sublayer below the wave peak,

ii Shear layer near the jump and

iii Outer layer.

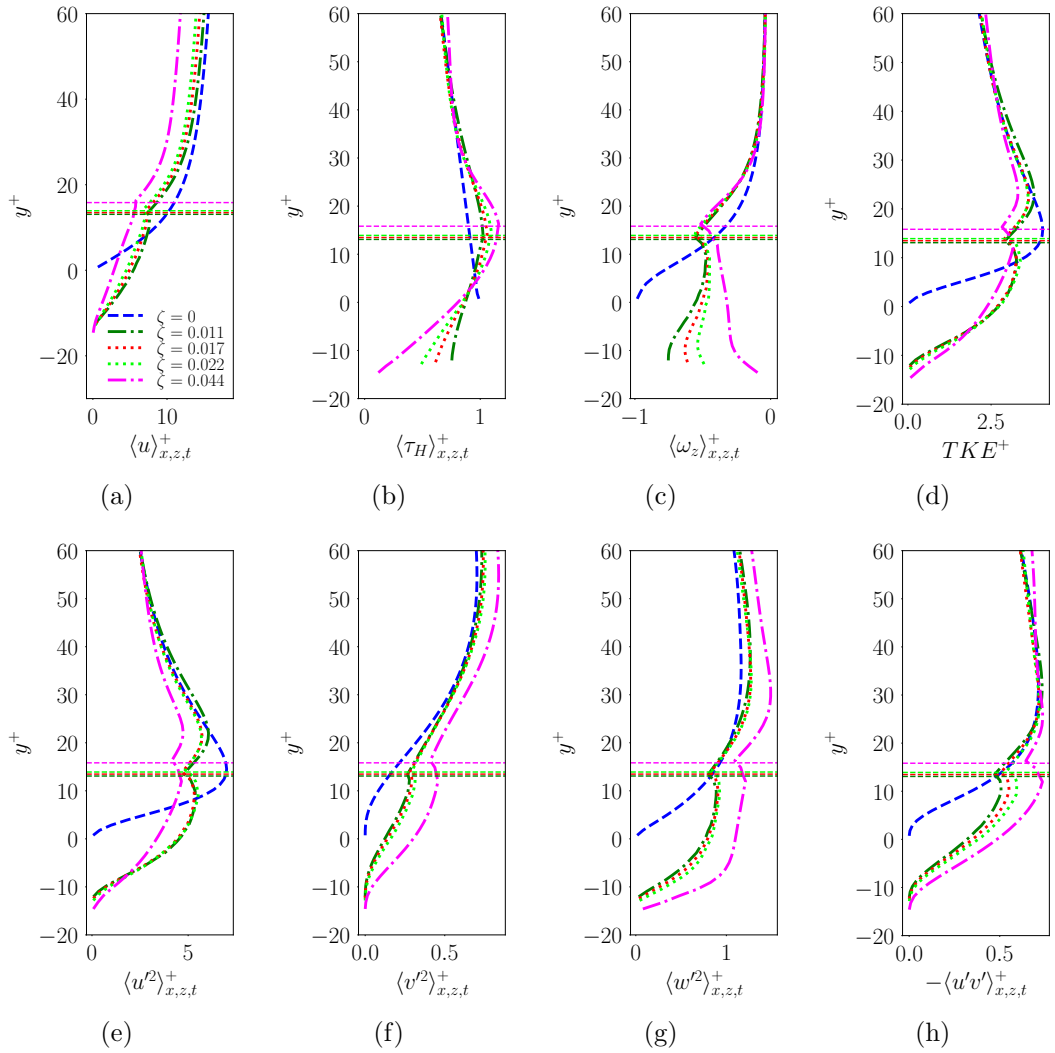

Figure 5.4: Inner scaled mean (a) streamwise velocity, (b) horizontal stress, (c) spanwise vorticity, (d) turbulent kinetic energy, (e) streamwise variance, (f) vertical variance, (g) spanwise variance and (h) covariance $\langle u'v' \rangle$ computed using global coordinate-based average. The thin horizontal dashed lines correspond to the different a^+ for $\zeta > 0$ (see Table 2.1).

Distinctly different streamwise velocity distribution is observed inside the roughness sublayer and above the peak of the wave as in figure V.4(a). Change in the vertical gradient with ζ is very clear inside the sublayer while this gradient becomes comparatively insensitive to ζ above the peak indicated by the near parallel lines. This suggests that inside the the roughness sublayer, viscous stress is dominant. This claim is further bolstered when we observe the horizontal stress profiles (figure V.4(b)) shifting the trend near a^+ (i.e. shear layer) because of the production of Reynolds stress in the buffer region.

While the turbulent kinetic energy (figure V.4(d)) and its most dominant component streamwise variance (figure V.4(e)) nearly collapses with each other in the outer layer similar to what we observed before, the profiles in the shear layer and the roughness sublayer behave very differently. Clearly the production of all the components of TKE starts from inside the roughness sublayer and the trends we observed from the averaging using local co-ordinate is still valid for $\zeta > 0$ both below and above a^+. Also, spanwise vorticity shows completely opposite trend on two side of $a+$ and collapses in the outer layer as observed in figure V.4(c).

This is to be noted that the mechanistic interpretation of the streamwise averaged structure using this new averaging technique as compared to the conventional technique has yet not been thoroughly explored. There is scope of stretching this analysis even deeper for understanding the streamwise dispersion in presence of streamwise inhomogeneity. However, we present a different 2D analysis of the inhomogeneity effect where we observe how the deviation from equilibrium is distributed along the streamwise and vertical direction. Figure 5.5, 5.6 and 5.7 represent inner scaled quantification of inhomogeneity effect, ϵ_I for different turbulent quantities by taking out the 1D averaged profile using global co-ordinate from the 2D structure of that

quantity. As example, inhomogeneity effect on the streamwise velocity is expressed as:

$$\epsilon^{+}_{I,\langle u\rangle} = \langle u\rangle^{+}_{z,t} - \langle u\rangle^{+}_{x,z,t}, \tag{5.1}$$

where, $\langle u\rangle^{+}_{x,z,t}$ varies only with y_{global}.

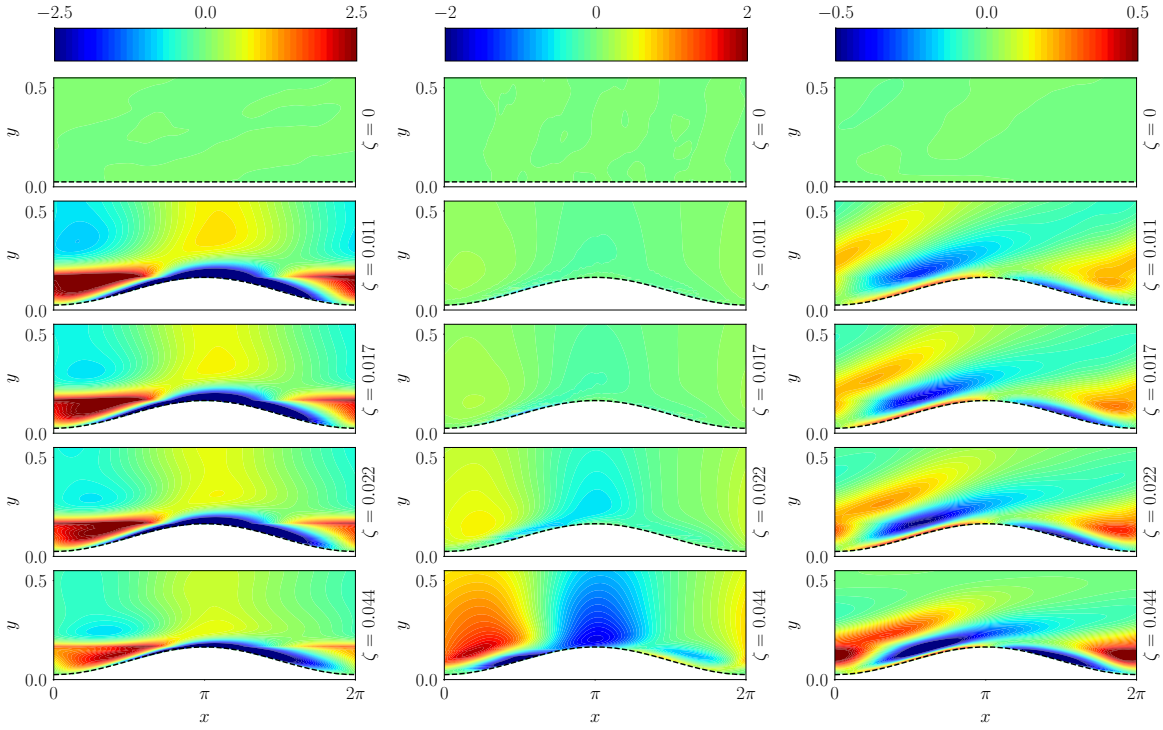

(a) $\epsilon^{+}_{I,\langle u\rangle}$ (b) $\epsilon^{+}_{I,\langle v\rangle}$ (c) $\epsilon^{+}_{I,\langle \tau_H\rangle}$

Figure 5.5: Inner scaled inhomogeneity effect on (a) streamwise velocity (b) vertical velocity and (c) horizontal stress

In the inner scaled streamwise velocity, the surface inhomogeneity effect is positive in the trough of the wave ($\epsilon^{+}_{I,\langle u\rangle} > 0$) representing higher local streamwise velocity compared to the streamwise averaged 1D profile. On the other hand adjacent to the wall near the peak this effect is negative evident from the thin blue layer wrapping around the crest as in figure V.5(a). With increasing steepness (ζ), inhomogeneity effect gets weaker, particularly around the trough. Also, the negative effect is skewed into the downslope region of the wave indicating significantly lower velocity region near the surface of the downslope. While this skewed nature is consistent with the

observations we have already made, the decreasing trend of the effect with increasing ζ is intriguing. This is most likely related to the flow through time required for the particle to traverse a single wave. The less time a particle gets to traverse a full wave, the less deviation from equilibrium it experiences below the inertial layer. However, the vertical variability of this streamwise velocity increases with ζ indicated by the increasingly higher magnitude of horizontal stress (τ_H) observed in figure V.5(c). Inhomogeneity effect for horizontal stress is also asymmetric showing more stress than average in the trough region while less stress is evident near the peak. Surprisingly for up to $\zeta = 0.017$ the effect of inhomogeneity seems to be very little as observed in figure V.5(b). For $\zeta = 0.022$ we see the inhomogeneity structure growing and reaching to significant amount for $\zeta = 0.044$. This is definitely an artifact of the onset of separation, because we only see relatively consistent separation for $\zeta > 0.017$.

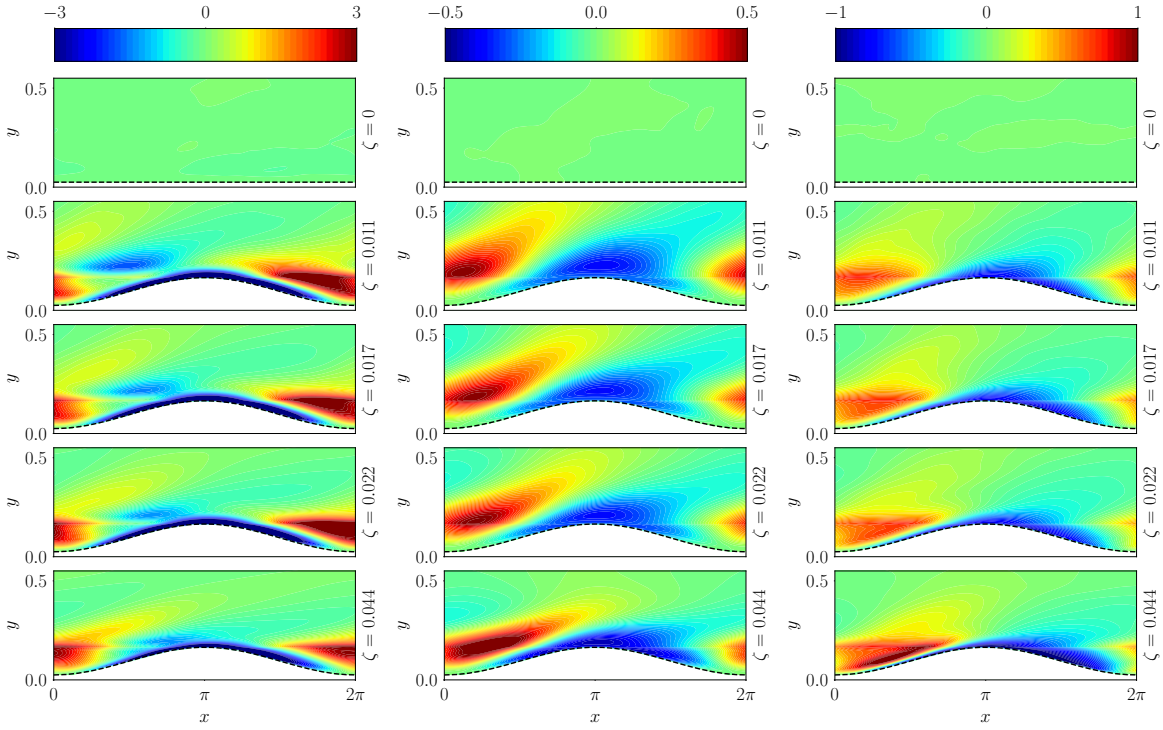

(a) $\epsilon^+_{I,\langle u'^2\rangle}$ (b) $\epsilon^+_{I,\langle v'^2\rangle}$ (c) $\epsilon^+_{I,\langle w'^2\rangle}$

Figure 5.6: Inner scaled inhomogeneity effect on (a) streamwise variance (b) vertical variance and (c) spanwise variance

Effect of the inhomogeneity on the second order statistics seem to be insensitive to the steepness (ζ) until separation becomes consistent in the downslope region. The structure of the inhomogeneity effect is different on the two side of the wave peak whatsoever. Position of the peak vertical and spanwise variance gets closer to the surface at the upslope region for $\zeta = 0.044$ as evidenced in figure 5.6. Reynolds stress also shows similar behavior as in figure V.7(a). Positive inhomogeneity effect in the streamwise variance indicates more production at the downslope compared to the upslope of the wave (figure V.6(b)). On the contrary, vertical and spanwise variance seems to peak in the upslope while showing large negative effect region in the downslope (figure V.6(b) and figure V.6(c))

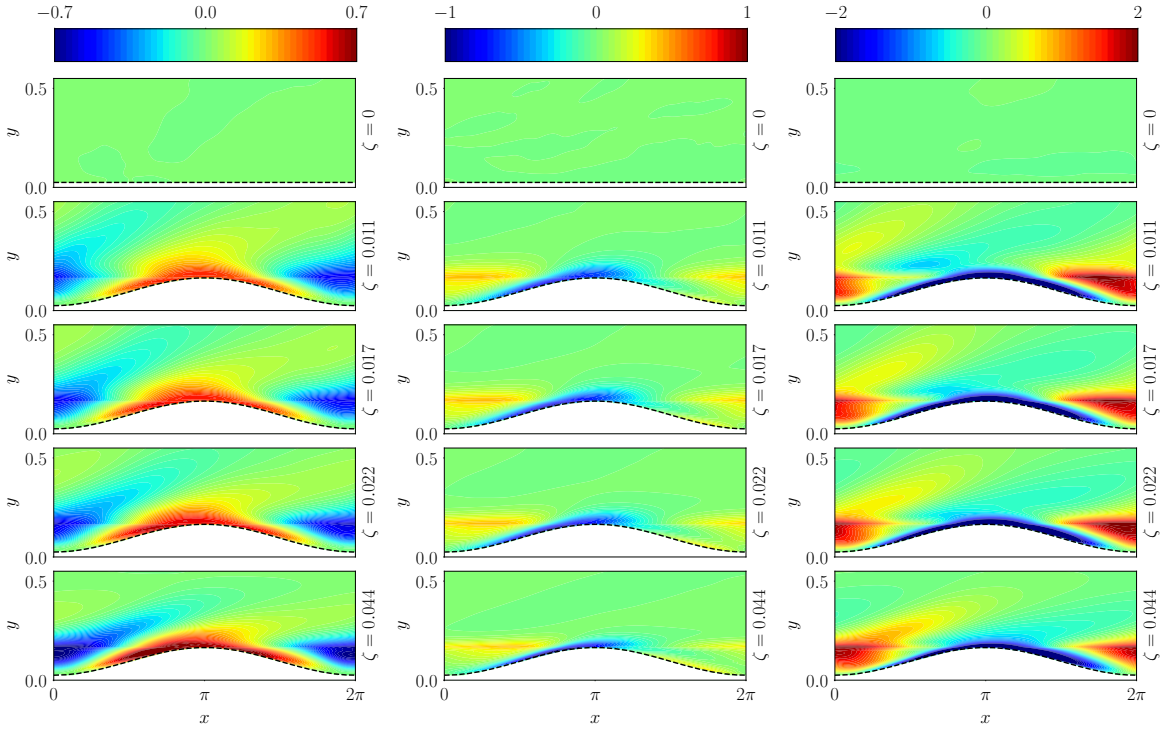

(a) $\epsilon^+_{I,\langle u'v'\rangle}$ (b) $\epsilon^+_{I,\langle \omega_z\rangle}$ (c) TKE^+

Figure 5.7: Inner scaled inhomogeneity effect on (a) $\langle u'v'\rangle_{z,t}$ covariance (b) spanwise vorticity and (c) TKE

A thin blue region ($\omega_z \approx -1$) of negative effect of inhomogeneity in vorticity distribution seems to wrap around the peak of the wave that extends mostly over the

upslope region and ends just after the peak is reached. This represents the potential destruction of the shear layer in the downslope. If we compare with the 2D spanwise vorticity in figure V.3(c), we see the similar trend of the blue structure compared with the shear layer in a sense that the blue inhomogeneity structure also ends earlier as ζ increases.

Based on this analysis of 2D deviation from the 1D averaged profile, one conclusion is clear that the roughness sublayer is of immense importance in the study of inhomogeneity borne asymmetric structure. Because, the effects of the inhomogeneity is most pronounced in that region.

5.3 Stationwise Dissection of Asymmetric Structure

At this stage, we have completed a decent study of global structures corresponding to first and second order statistics to understand the dynamics of fluid particles in presence of a undulated boundary as a function of vertical position. Moreover, we looked at the 2D structure to understand the streamwise variability along with the effect of inhomogeneity to a reasonable extent. However, for better understanding the asymmetric structure due to the presence of geometric inhomogeneity, we perform a stationwise dissection of local 1D structure that varies only with vertical distance $y_{local,1}$ (coordinate system explained in section 3.1).

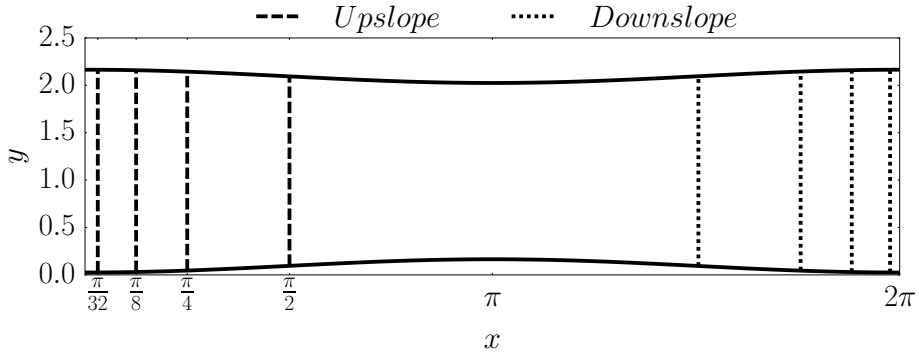

Figure 5.8: Station architecture for the analysis

We choose systematically located pairs of streamwise stations with varying phase angle, ϕ. More specifically, if the upslope station of a pair is at $\phi = \frac{\pi}{2}$ then the corresponding downslope station would be at $\phi = 2\pi - \frac{\pi}{2}$. This allows us to accurately characterize the difference in turbulence structure between the upslope and the downslope of the wave. Figure 5.8 illustrates the location of the stations as vertical lines where the dashed and dotted lines represents the upslope and downslope stations respectively. This is to be noted that due to the periodic nature along the stream, the first pair of stations ($\phi = \frac{\pi}{32}$ and $\phi = 2\pi - \frac{\pi}{32}$) shows very similar behavior. But the structures starts deviating as we start climbing towards the peak from both end of the computational domain. For the sake of representing the vertically varying 1D structure at both the upslope and the corresponding downslope station, we use the same color code that we have been using throughout the paper. More specifically we use dashed blue, dash-dotted green, dotted red, dotted lime and dash-dotted magenta lines for the upslope structure corresponding to $\zeta = 0$, $\zeta = 0.011$, $\zeta = 0.017$, $\zeta = 0.022$ and $\zeta = 0.044$ respectively. On the other hand thin solid lines with square blue, upward-pointing triangular green, circular red, asterisk lime and downward-pointing triangular markers have been used to represent corresponding downslope profiles respectively.

Major difference in the streamwise velocity behavior is observed between the upslope and downslope 1D profile at $\phi = \frac{\pi}{4}$ and $\phi = \frac{\pi}{2}$, particularly at $y/\delta \approx 0.0 - 0.2$ as illustrated in figure 5.9. Slowing down of the fluid particle at the downslope station is fairly evident which results into the downward shift of the logarithmic profile in figure III.2(a). Outer layer streamwise velocity in the downslope station exhibits higher magnitude but almost the same vertical gradient compared to the upslope profile to compensate for the mass flow deficit in the near wall region. This near wall asymmetry is immensely important to ultimately characterize the roughness behavior of wavy wall as they are directly related to the quantification of the roughness function.

Now, this small vertical gradient of streamwise velocity is dominantly responsible for the low viscous drag felt by fluid particles at surface in the downslope. On top of that the form drag is also significantly small in the downslope as the particles deal with the backward facing surface when they climb down from the wave peak. This two effect cumulatively results in the asymmetry in the total horizontal stress near the wall as shown in figure 5.10. At the the upslope stations for each $\zeta > 0$ where $\phi > \frac{\pi}{32}$ shows a small kink (local minima) indicating the enforced form drag acting on the particles at the upslope by the forward facing wave surface which is absent in the downslope stations. The second peak away from the wall represents the inclusion of Reynolds stress which starts getting produced at the buffer layer and gains dominance over viscous stress at a height which shifts closer to the surface with increasing ζ.

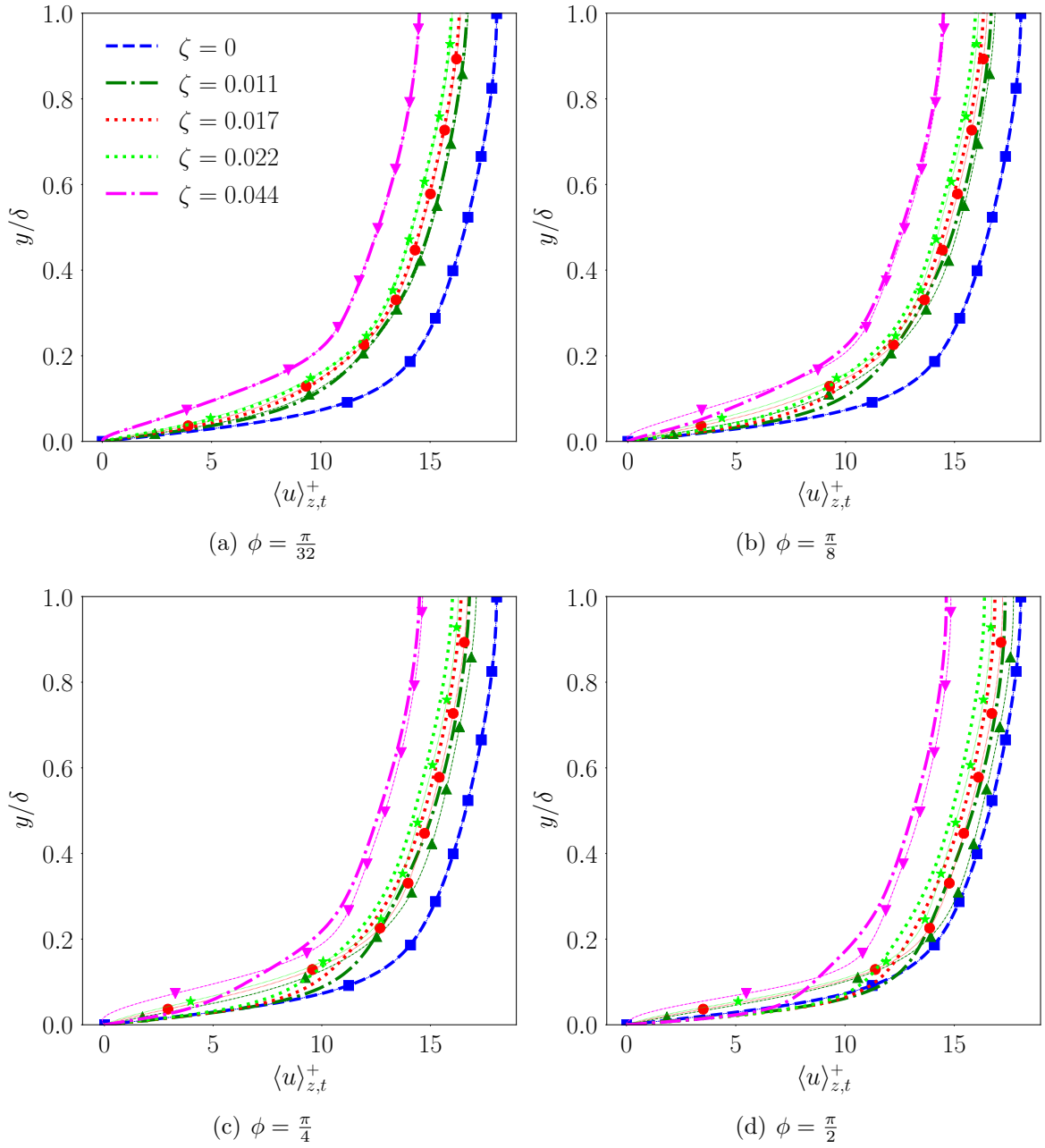

(a) $\phi = \frac{\pi}{32}$ (b) $\phi = \frac{\pi}{8}$

(c) $\phi = \frac{\pi}{4}$ (d) $\phi = \frac{\pi}{2}$

Figure 5.9: Comparison of spanwise and temporally averaged inner scaled streamwise velocity profile at different phase locations (ϕ) of the wave.

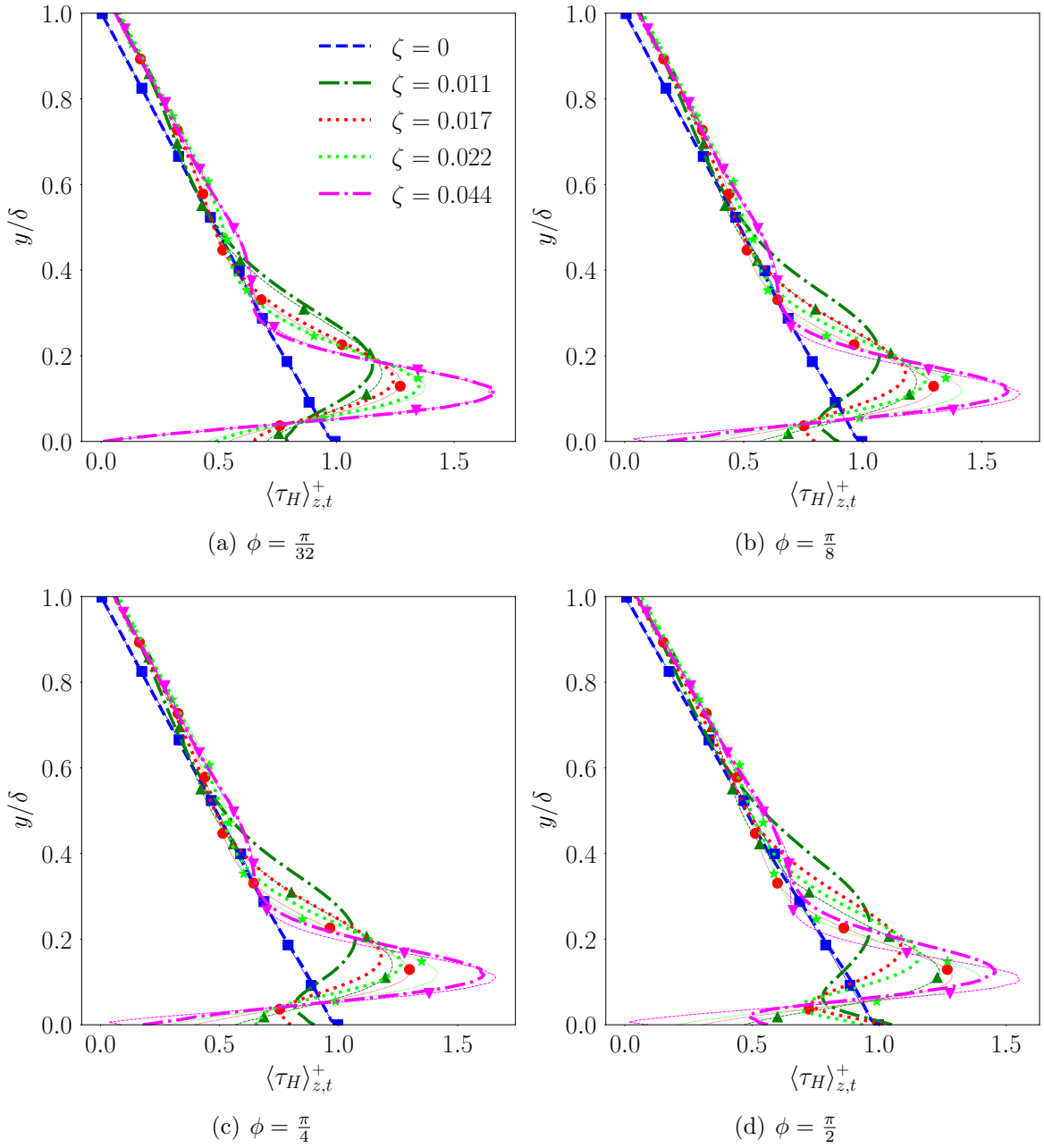

(a) $\phi = \frac{\pi}{32}$ (b) $\phi = \frac{\pi}{8}$

(c) $\phi = \frac{\pi}{4}$ (d) $\phi = \frac{\pi}{2}$

Figure 5.10: Comparison of spanwise and temporally averaged inner scaled horizontal stress profile at different phase locations (ϕ) of the wave.

Asymmetry in the vertical velocity is expected between upslope and downslope in a sense that opposite sign would be expected as the fluid particles climb up and down from the peak in the upslope and downslope region respectively. However, the downslope profile is even more disturbed because of the absence of any forward

facing surface that results in the downslope fluid particles near the trough to roll over particles having very small streamwise velocity. This causes those particles to get pushed down in the middle phases (i.e. $\phi = \frac{\pi}{8}$ and $\phi = \frac{\pi}{4}$) indicated by very high negative vertical velocity in the downslope as shown in 5.11.

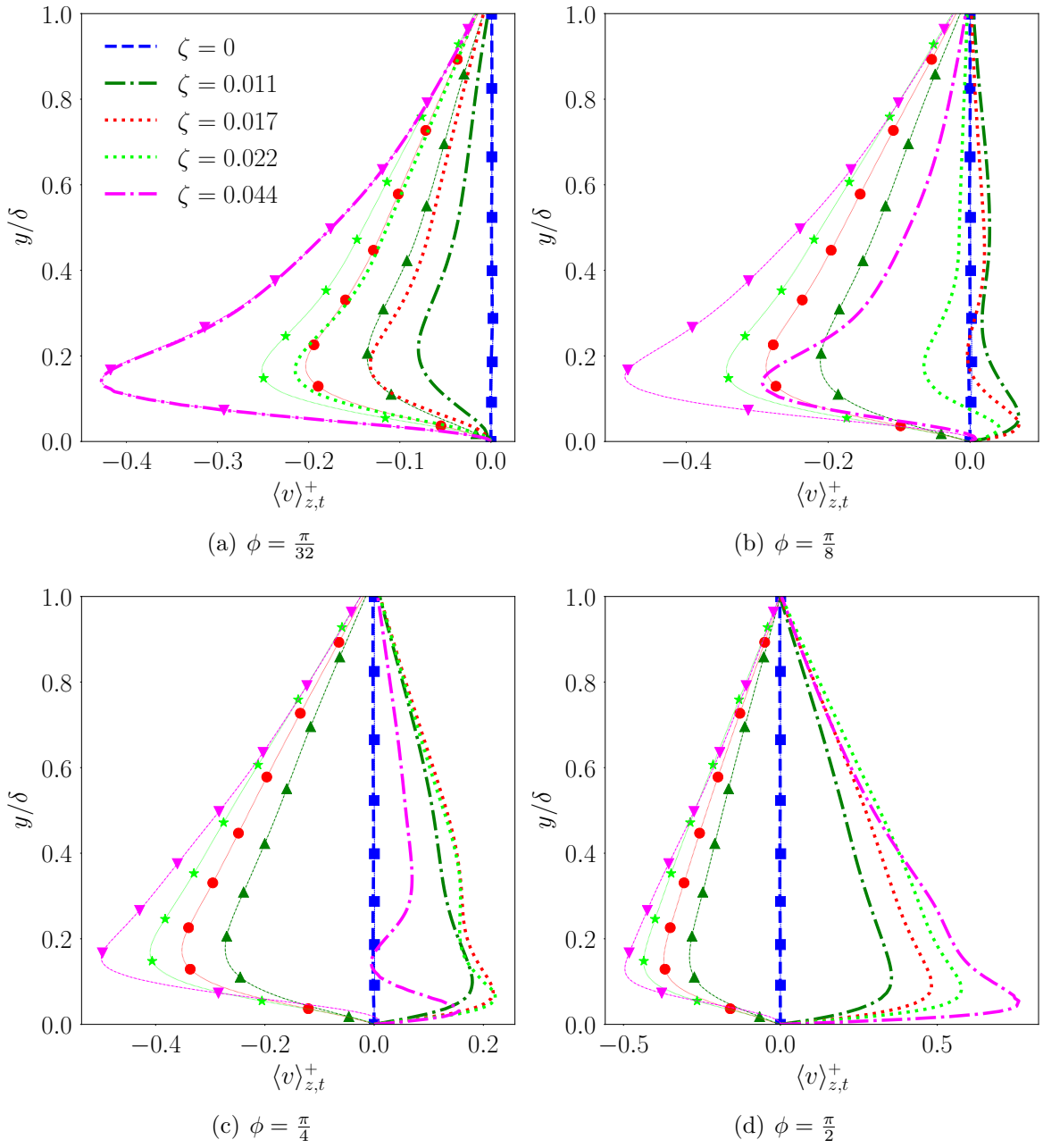

(a) $\phi = \frac{\pi}{32}$ (b) $\phi = \frac{\pi}{8}$

(c) $\phi = \frac{\pi}{4}$ (d) $\phi = \frac{\pi}{2}$

Figure 5.11: Comparison of spanwise and temporally averaged inner scaled vertical velocity profile at different phase locations (ϕ) of the wave.

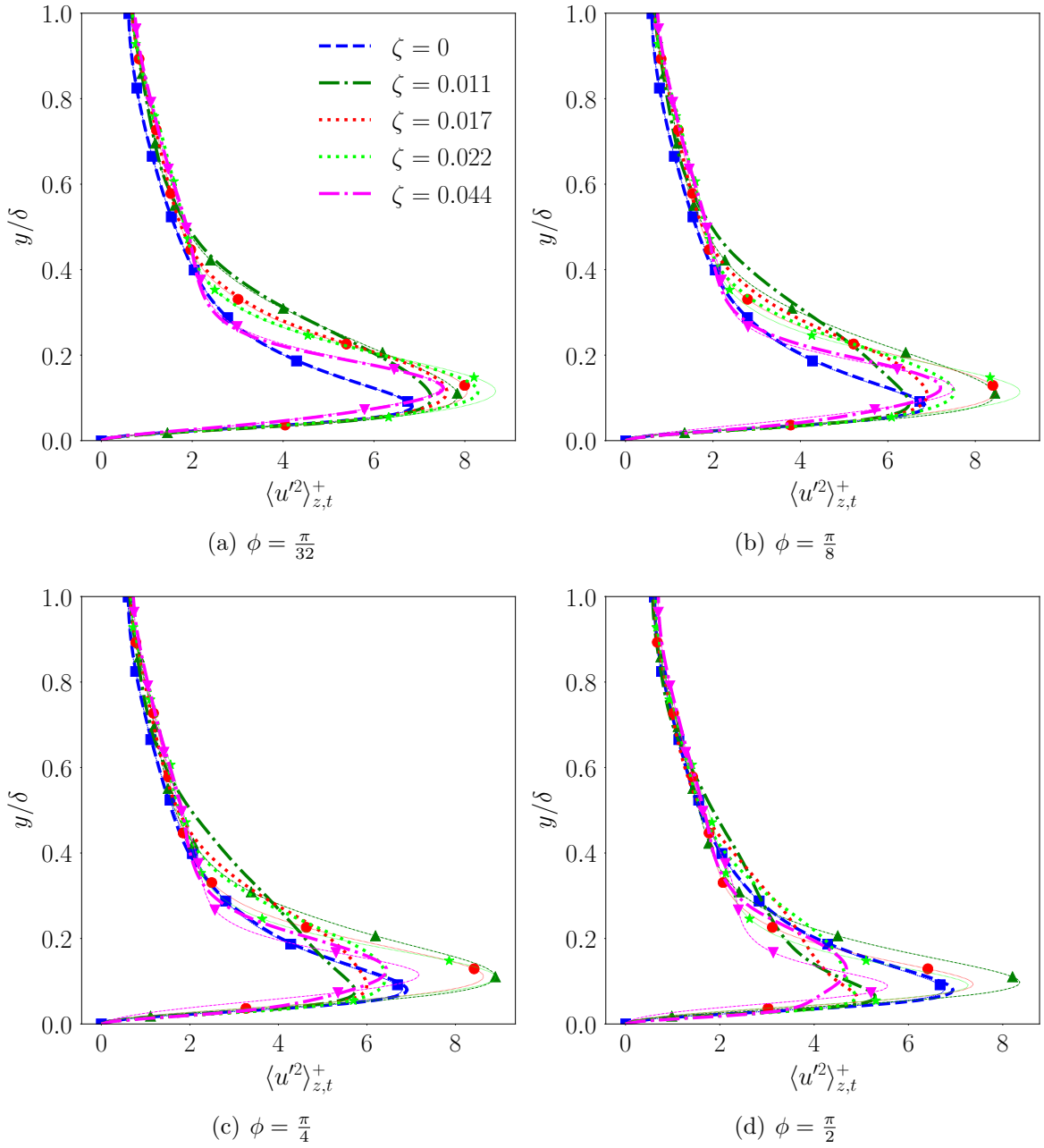

Figure 5.12: Comparison of spanwise and temporally averaged inner scaled streamwise variance profile at different phase locations (ϕ) of the wave.

Being the most dominant among the three variance profiles, streamwise variance exhibits significant deviations between the upslope and downslope as observed in figure 5.12. Downslope stations shows much higher streamwise variance compared to the corresponding upslope stations. Moreover, the peak of the variance starts decreasing

while climbing up the wave and increases while climbing down. This deviation gets biggest at $\phi = 2\pi - \frac{\pi}{4}$ as the upslope peak of the profile reaches minimum and the downslope peak reaches maximum.

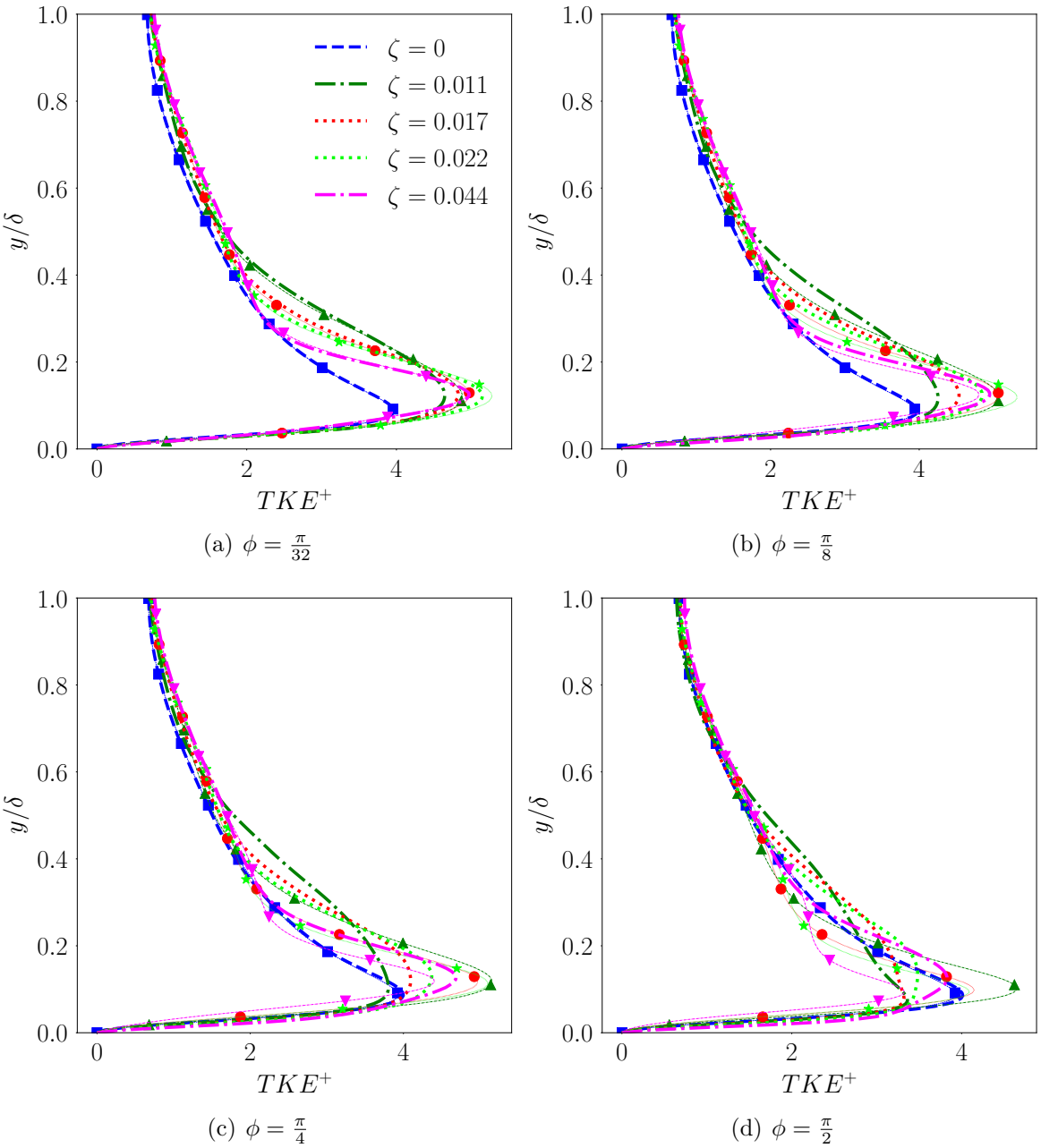

(a) $\phi = \frac{\pi}{32}$ (b) $\phi = \frac{\pi}{8}$

(c) $\phi = \frac{\pi}{4}$ (d) $\phi = \frac{\pi}{2}$

Figure 5.13: Comparison of spanwise and temporally averaged inner scaled TKE profile at different phase locations (ϕ) of the wave.

Similar trend is observed in the TKE profiles in figure 5.13 which is obviously expected to be influenced by the behavior of streamwise variance . On the contrary,

vertical and spanwise variance shows opposite behavior which is bigger magnitude in the upslope peak and smaller magnitude in the downslope peak as observed in figure 5.14 and 5.15 respectively. Also in consistence with the 1D profiles, the effect of changing wavelengths in the undulation-affected cases is not straightforward.

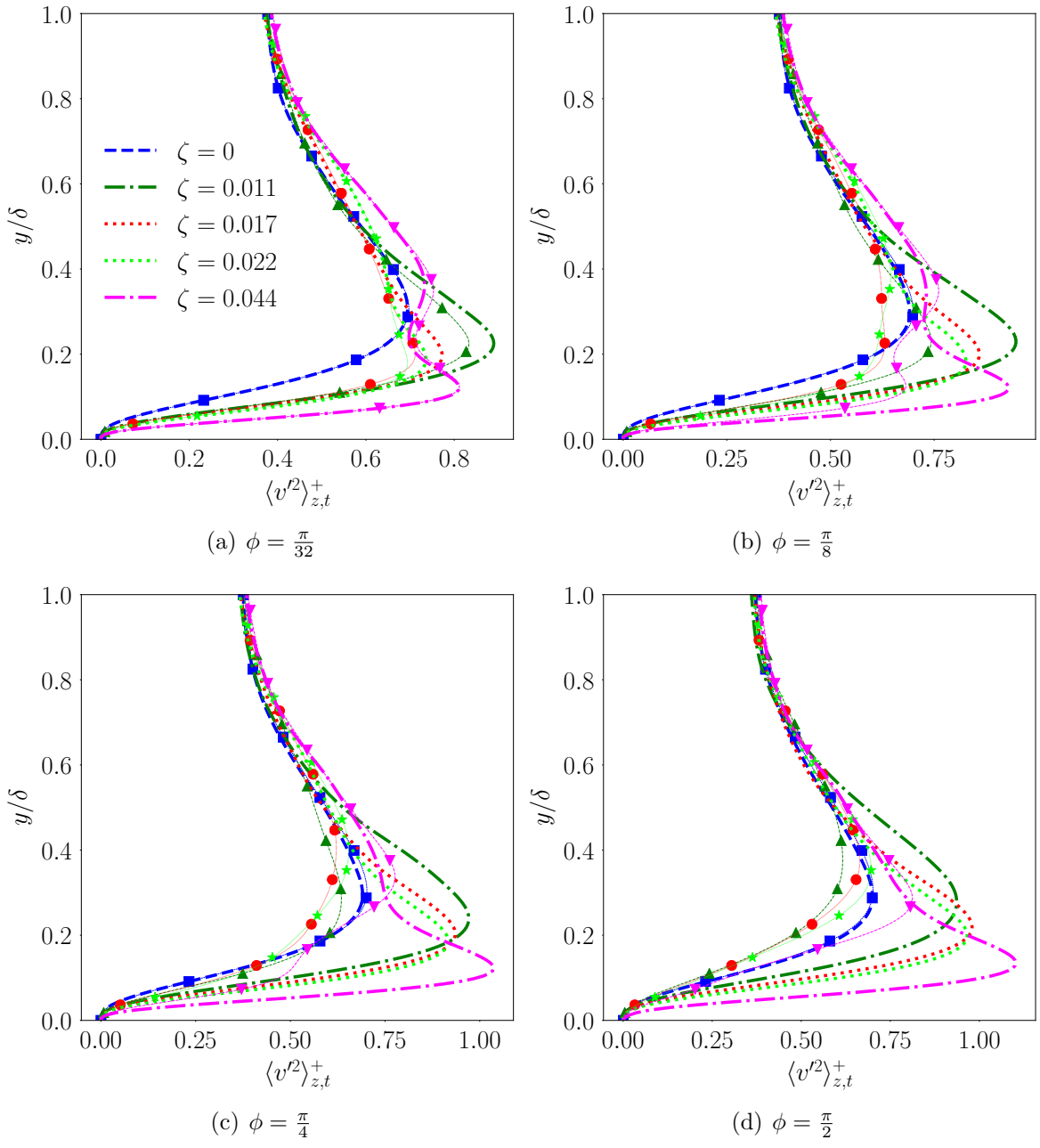

(a) $\phi = \frac{\pi}{32}$ (b) $\phi = \frac{\pi}{8}$

(c) $\phi = \frac{\pi}{4}$ (d) $\phi = \frac{\pi}{2}$

Figure 5.14: Comparison of spanwise and temporally averaged inner scaled vertical variance profile at different phase locations (ϕ) of the wave.

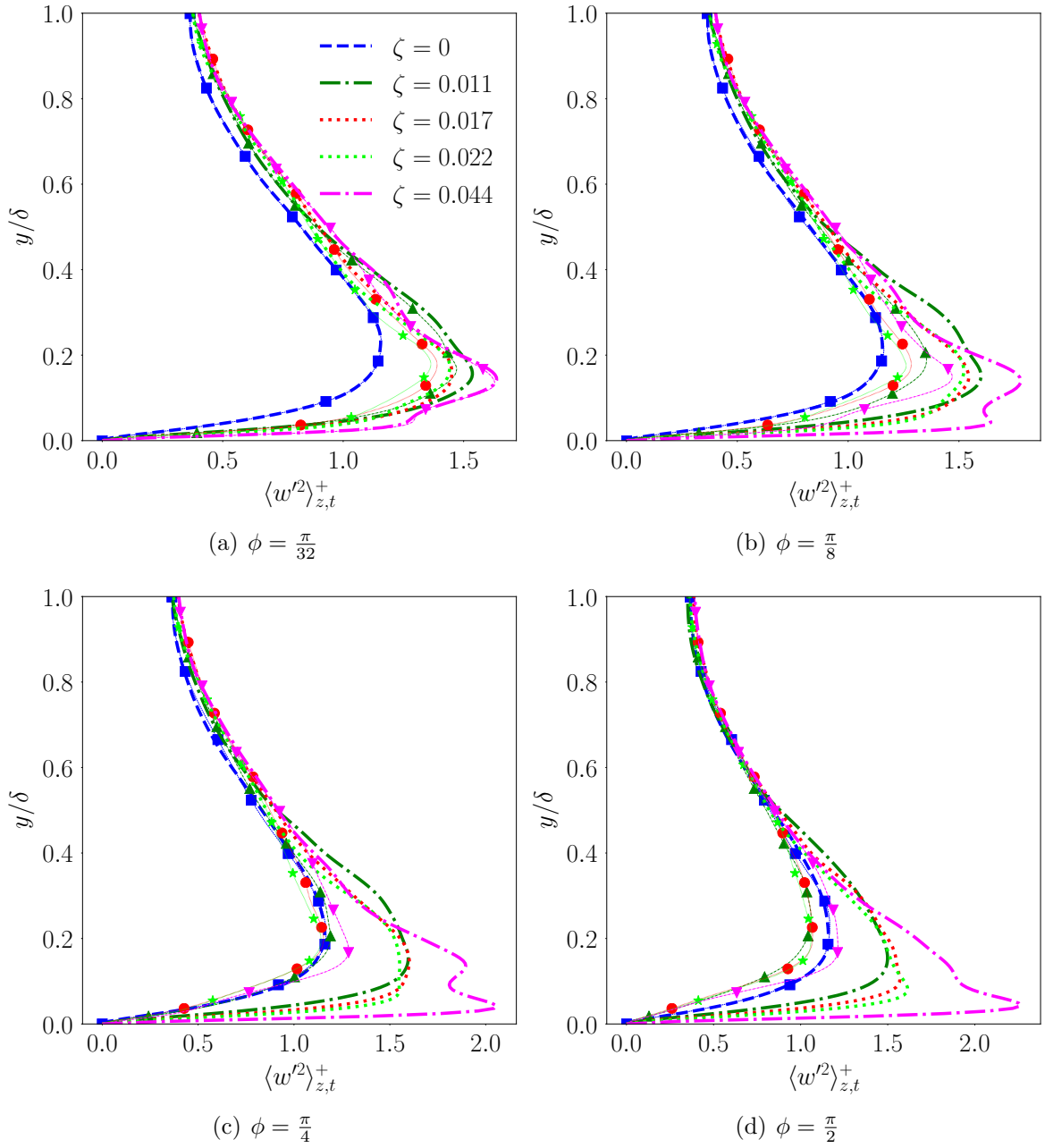

Figure 5.15: Comparison of spanwise and temporally averaged inner scaled spanwise variance profile at different phase locations (ϕ) of the wave.

Only the pair of stations closest to the peak ($\phi = \frac{\pi}{2}$ and $\Phi = 2\pi - \frac{\pi}{2}$) shows higher peak of vertical and spanwise profiles for increased wave steepness. So it makes more sense that on average the effect of changing wave steepness is not that significant while there is certain jump between with and without undulation flows. For $\zeta = 0.044$

there is another dominant asymmetry which is characterized by the magnitude of the two peaks. As earlier said in section 3.4.2, this double peak is a result of isolated vertical variance structure inside and outside the separation bubble. It is clear form the profiles for $\phi = \frac{\pi}{8}$ and $\phi = \frac{\pi}{4}$ that in the upslope, the inner peak is dominant while in the downslope, the outer peak is dominant.

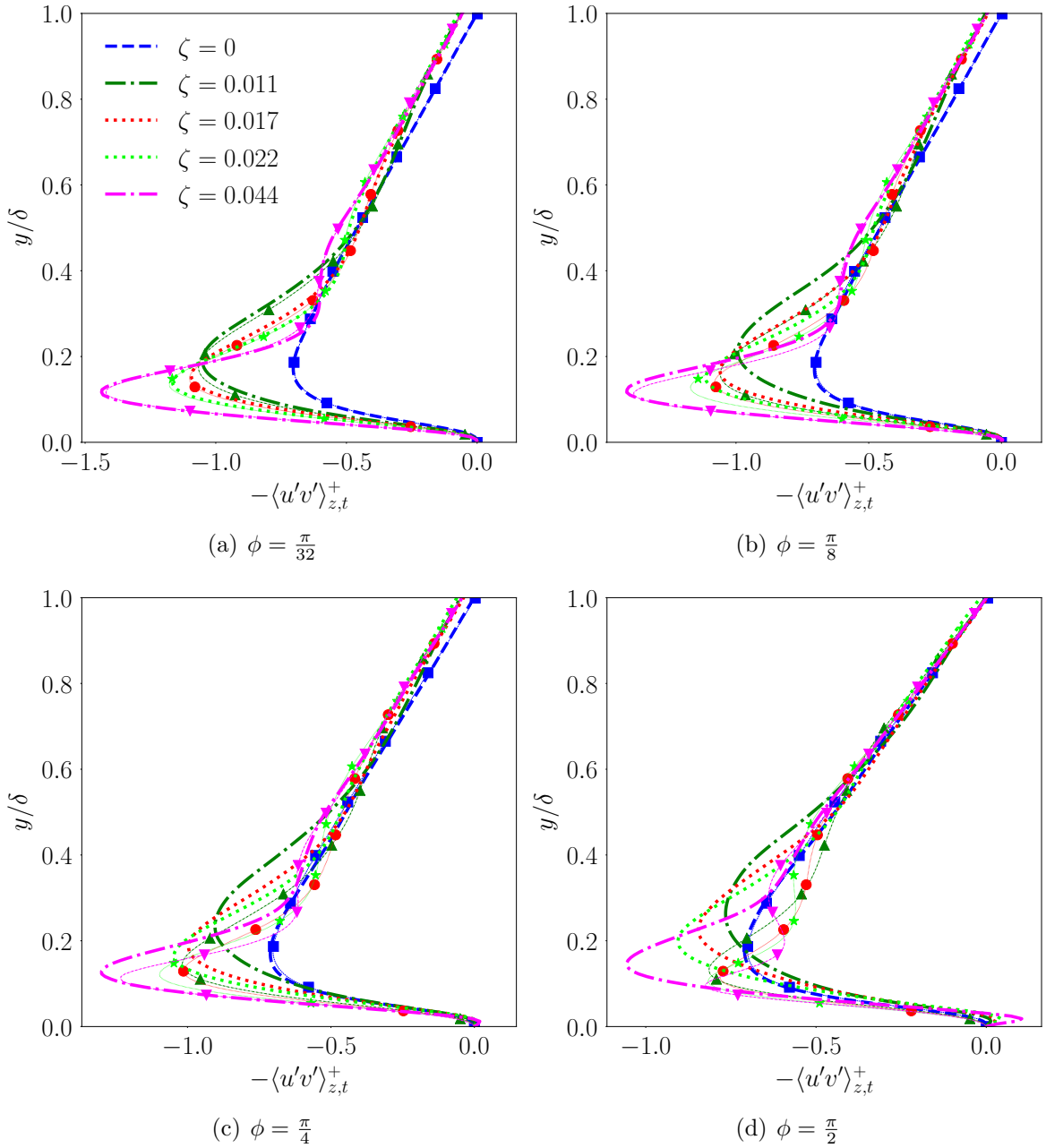

(a) $\phi = \frac{\pi}{32}$ (b) $\phi = \frac{\pi}{8}$

(c) $\phi = \frac{\pi}{4}$ (d) $\phi = \frac{\pi}{2}$

Figure 5.16: Comparison of spanwise and temporally averaged inner scaled Reynolds stress profile at different phase locations (ϕ) of the wave.

Onset of flow detachment is hinted in the upslope station having positive Reynolds stress profiles particularly visible at $\phi = \frac{\pi}{2}$ as shown in figure 5.16. The peak of the profile increases with increased ζ in all stations consistently with our observation from the corresponding streamwise averaged profile..

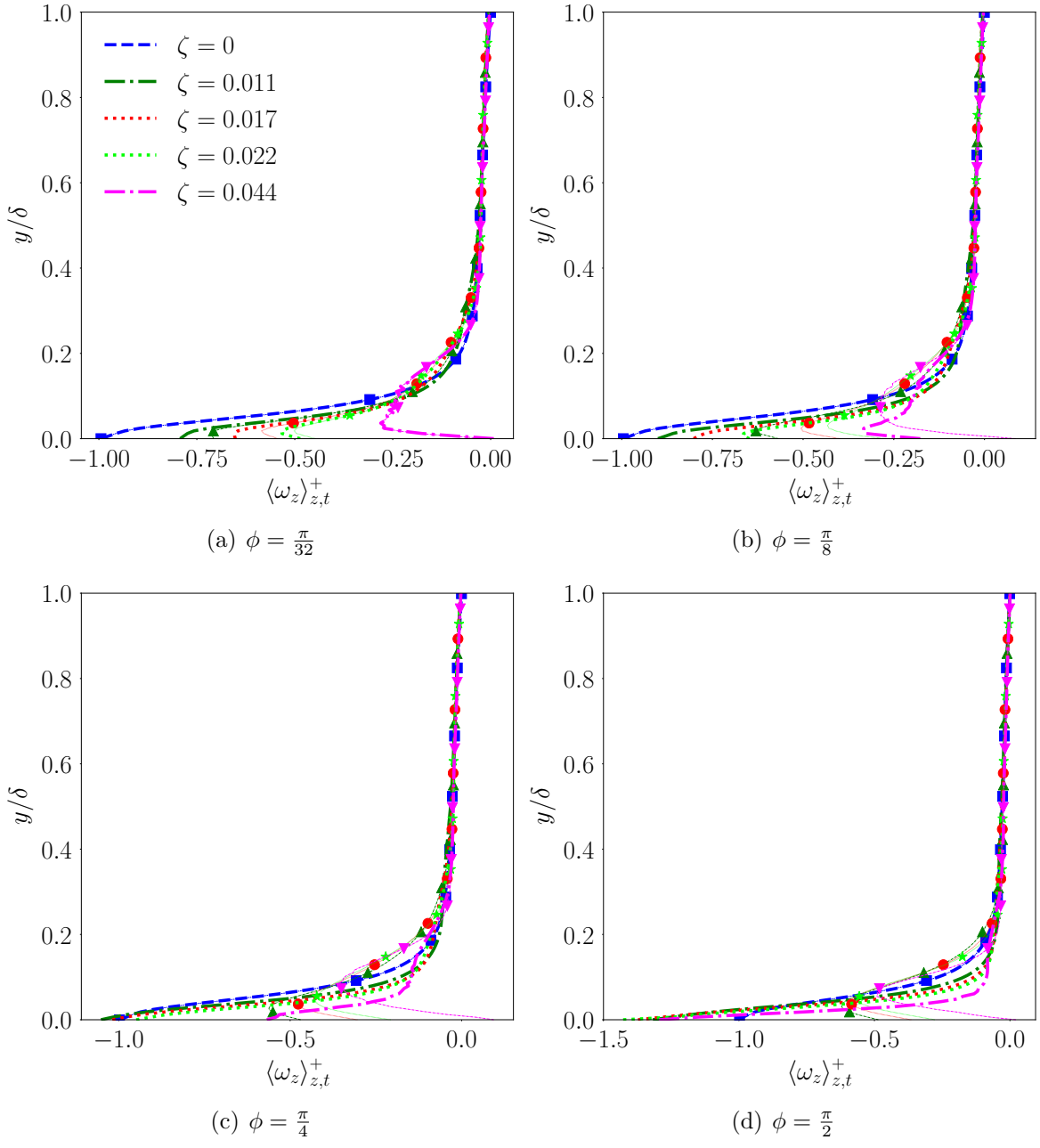

(a) $\phi = \frac{\pi}{32}$ (b) $\phi = \frac{\pi}{8}$

(c) $\phi = \frac{\pi}{4}$ (d) $\phi = \frac{\pi}{2}$

Figure 5.17: Comparison of spanwise and temporally averaged inner scaled spanwise vorticity profile at different phase locations (ϕ) of the wave.

The breaking up of the shear layer is also visible in the local stations in the

downslope region as shown in the spanwise vorticity profiles in figure 5.17. Thin low vorticity kinks near the downslope wall is observed that indicates that the shear layer tends to break up and incipient separation is hinted.

5.4 Quantification of the Deviation

Now that we have good understanding of the global and local structures as a function of both streamwise and vertical distance, we quantify the asymmetry induced errors as a function of steepness (ζ) and phase angle (ϕ) and interpret the trends through the lens of wall turbulence physics. This final analysis will provide concrete idea on the strength of deviation and the streamwise position where it is pronounced maximum. Both 1D and 2D representation of the asymmetry error is provided. In the 1D analysis as in figure 5.18, $\phi = 0$ specifies the lowest point of the wave (i.e. centre of the trough) while $\phi = \pi$ specifies the maximum (i.e. peak of the wave).

Streamwise velocity deviation slightly increases with the increasing wave steepness for the cases where $\zeta < 0.044$. At $\zeta = 0.044$ the peak of the asymmetry induced error seems to go down in magnitude. This is most likely because of the detachment of the flow happening at that steepness. Maximum deviation is identified just before the midway of the climb (mid-climb is specified as $\phi = \frac{\pi}{2}$) as shown in figure V.18(a). Vertical velocity shows the similar trend in deviation, however, the maximum is identified just after the midway of the climb as shown in figure V.18(b). The peak of the asymmetry error shifts closer to the peak with increasing ζ. Therefore, one thing can be said from the current analysis that the asymmetry induced error is sensitive to the presence of separation in case of streamwise velocity but insensitive in case of vertical velocity. The position of the maximum deviation is critical because mid way of the climb basically represents the steepest point (i.e. maximum local slope) of the wave where the form drag is expected to be maximum. This is evident from the 2D asymmetry structure shown in figure V.19(a) where we see a thick dark blue region

near the wall centered around the mid-climb of the wave. The shift towards the wave peak of the vertical velocity is also clear from figure V.19(b).

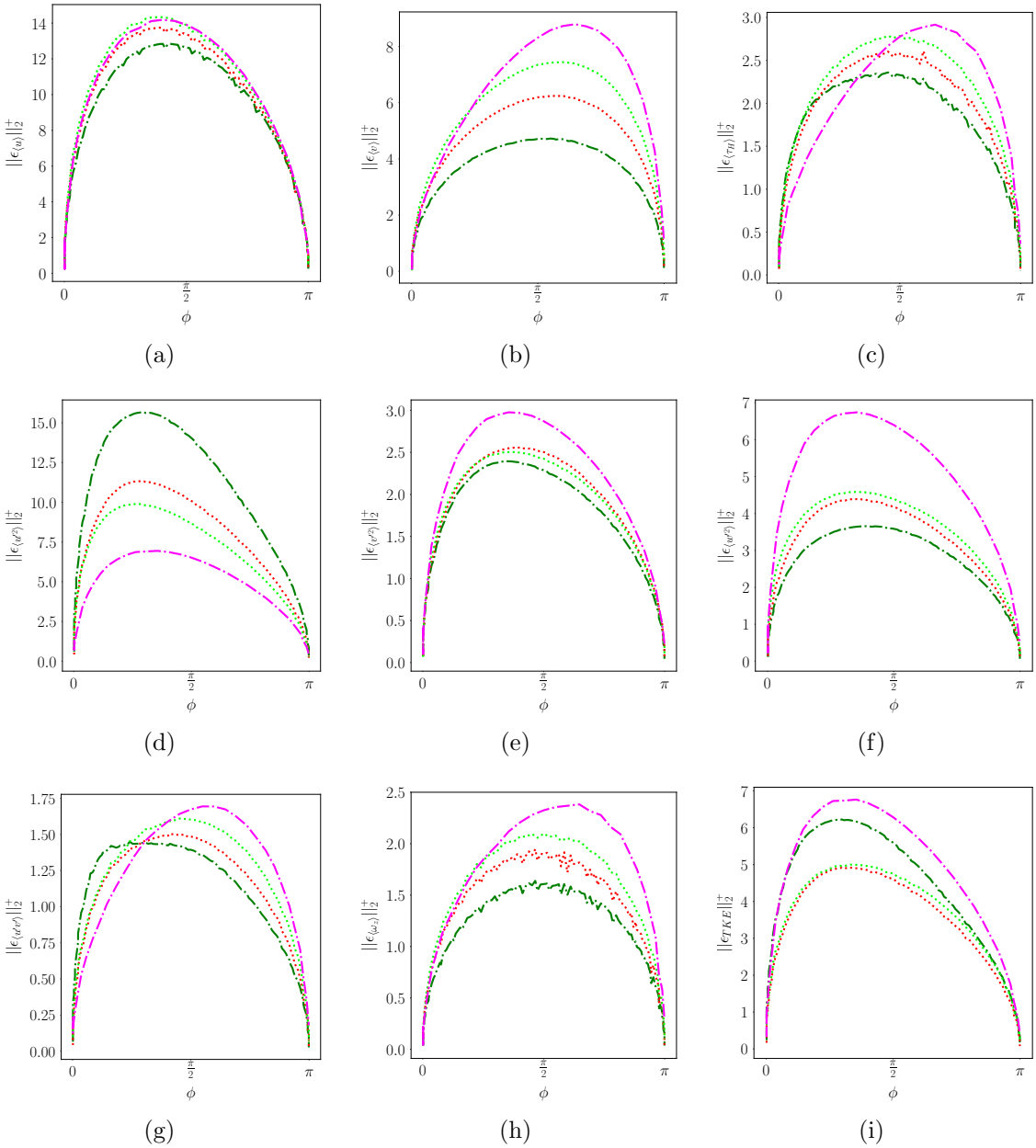

Figure 5.18: Normalized L_2 norm error ($||\epsilon||_2^+$) between upslope and downslope profile of different turbulent quantities: (a) streamwise velocity, (b) wall normal velocity, (c) horizontal stress, (d) streamwise variance, (e) vertical variance, (f) spanwise variance, (g) Reynolds stress, (h) turbulent kinetic energy and (i) spanwise vorticity, plotted against the phase angle, ϕ (The dash-dotted green, dotted red, dotted lime and dash-dotted magenta lines correspond to $\zeta = 0.011$, $\zeta = 0.017$, $\zeta = 0.022$ and $\zeta = 0.044$ respectively)

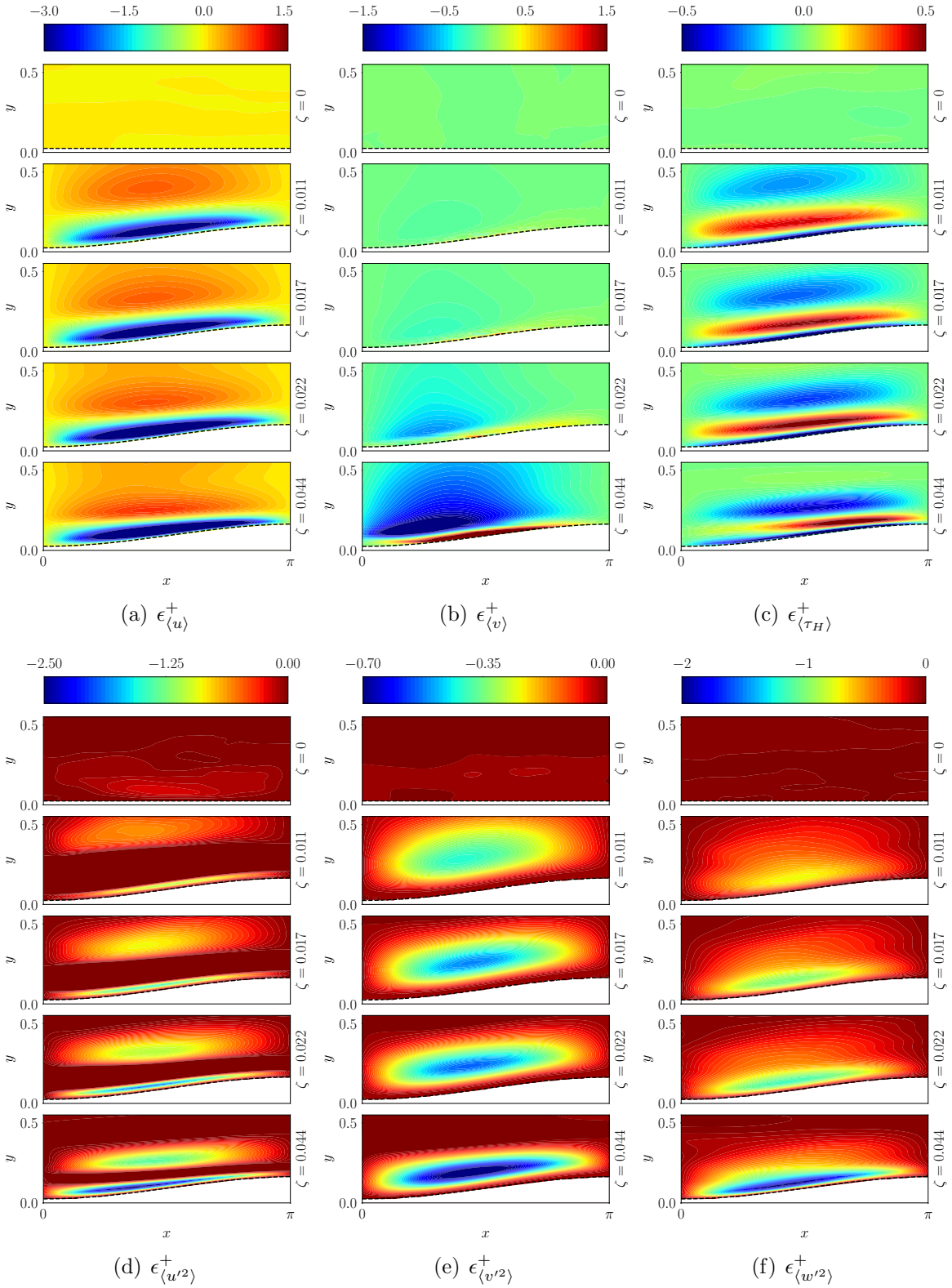

(a) $\epsilon^+_{\langle u \rangle}$ (b) $\epsilon^+_{\langle v \rangle}$ (c) $\epsilon^+_{\langle \tau_H \rangle}$

(d) $\epsilon^+_{\langle u'^2 \rangle}$ (e) $\epsilon^+_{\langle v'^2 \rangle}$ (f) $\epsilon^+_{\langle w'^2 \rangle}$

Figure 5.19: Inner scaled asymmetry-induced error in (a) streamwise velocity, (b) vertical velocity, (c) horizontal stress, (d) streamwise variance, (e) vertical variance and (f) spanwise variance

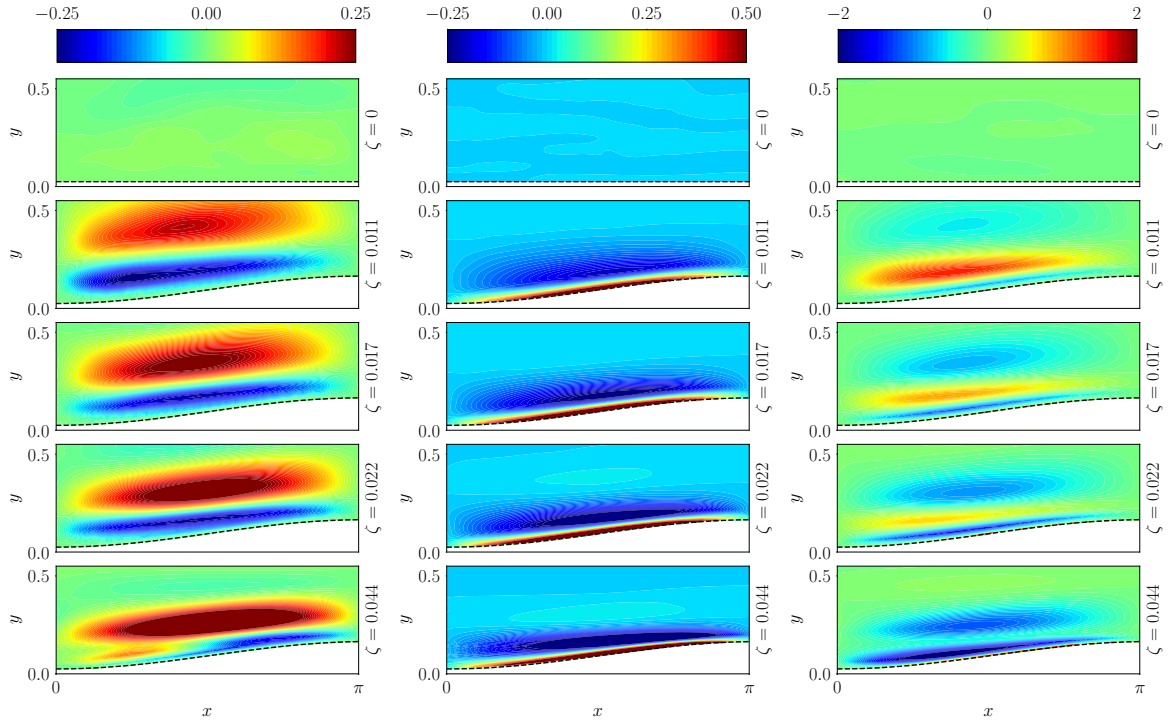

(a) $\epsilon^{+}_{\langle u'v' \rangle}$ (b) $\epsilon^{+}_{\langle \omega_z \rangle}$ (c) TKE^{+}

Figure 5.20: Inner scaled asymmetry-induced error in (a) $\langle u'v' \rangle_{z,t}$ covariance (b) spanwise vorticity and (c) TKE

Asymmetric error in total stress is also maximum at around the midway of the climb shifting slightly to the right for up to $\zeta = 0.022$. However, this error is sensitive to the separation of flow as for $\zeta = 0.044$, the peak of the error shifts towards the peak from $\phi = \frac{\pi}{2}$. From the 2D structure, it is clear that the high stress region indicated by the red zone as in figure V.19(c) is shifting towards the wave peak for $\zeta = 0.044$ while the same shift is almost ignorable in other $\zeta > 0$.

In all three error plots for variances monotonic trend is evident as the position of peak value gets shifted to the left (i.e. away from the peak) indicating the skew towards the trough region of the wave as suggested in figure V.18(d), V.18(e) and V.18(f). However the magnitude of the peak shows different trend between streamwise variance and the other two components. While the peak magnitude of streamwise variance decreases with increasing ζ, spanwise and vertical variance increases with

increased steepness on the contrary.Similar to horizontal stress, the asymmetric error for vertical and spanwise variance seems to be sensitive to separation. As observed in figure V.19(e) and V.19(f) sudden jump in the magnitude takes place when $\zeta = 0.044$. Position of the maximum deviation suggests that the energy production is maximum near the trough of the wave which is suggested in figure V.18(i) too. However, the trend of the peak error with increasing ζ is yet inconclusive.

Reynolds stress deviation between the upslope and downslope is maximum just before the midpoint of the climb, but with increasing steepness this peak shifts towards the peak of the wave as suggested by figure V.18(g). Maximum magnitude of the deviation increases with ζ.

Spanwise vorticity seems to peak exactly at the midpoint of the climb, where the steepness is highest for $\zeta = 0.011 - 0.022$. But, it gets shifted closer to the peak as consistent flow separation is present for steeper wave steepness (i.e. $\zeta = 0.044$) of this asymmetric error increases as in figure. V.18(h) and V.20(b).

CHAPTER VI

Conclusion and Future Work

6.1 Conclusion

In this work, we report outcomes from a DNS-based investigation of the turbulence structure and its deviation from equilibrium using high Reynolds number flow between two infinitely parallel plates with 2D wavy undulations. In particular, we set out to assess the influence of small wave slopes (with little to medium flow separation) on the turbulence structure and their correspondence to common roughness characterization that invariably deals with the high slope regime. To maximize the shape sensitivity on the flow structure, we operate in a transitional roughness Reynolds number ($k^+ = a^+ \sim 13 - 15$) which is much smaller than the fully rough regime corresponding to ($k^+ = a^+ \gtrsim 70$).

The streamwise mean velocity structure indicates a characteristic downward shift (to higher y^+) of the logarithmic region of the TBL indicating increased flow drag with increase in wave slope, ζ. This is associated with a sustained upward vertical flow in the lower roughness sublayer and corresponding downward flow in the buffer layer. The strength of these vertical motions increases with ζ and have a dominant role to play in the near surface turbulence production processes. In fact, analysis of the mean non-dimensional streamwise velocity gradients and inner-scaled turbulence production show that the buffer layer expands with increasing wave slope, ζ indicating that the well-known equilibrium understanding of near-wall turbulence processes is modulated even for such highly shallow wavy surfaces.

In fact, characterization of the roughness effects from such shallow surface un-

dulations with minimal flow separation is very different from the strong separation and form drag dominated Nikuradse type sand grain rough surfaces. Therefore, in our case, drag as represented by the roughness function turns out to be very weakly dependent on the wave amplitude (related to roughness height, $k^+ = a^+$) and more on the effective wave slope (2ζ). These conclusions are consistent with Napoli et al. (2008); Schultz and Flack (2009) where wavy surfaces in the high slope limit approach Nikuradse type roughness. Therefore, in such cases, one needs to model $\Delta\langle u\rangle^+$ as $f(a^+, \zeta)$.

In presence of weak (if not inconsistent) flow separation, the turbulence generation process within the roughness sublayer is primarily topology driven. For the two-dimensional surface undulations considered in this work, the differences in turbulence generation for different ζ originate in the production of small quantities of vertical velocity variance closer to the surface due to non-zero values for the vertical velocity gradients. In contrast, for the equilibrium TBL over a flat surface, horizontal homogeneity implies that the mean vertical velocity and its gradients are zero. However, the predominant generation of vertical variance still occurs through redistribution of the streamwise velocity variance (generated closer to the surface) through the return to isotropy term. Therefore, these two different production mechanisms interact to cause $\langle v'^2\rangle^+_{x,z,t}$ to peak at a larger value and closer to the surface (relative to a flat TBL) with increasing wave steepness, ζ. Similar trends are observed for the inner-scaled spanwise velocity variance.

The effect on the streamwise velocity variance, $\langle u'^2\rangle^+_{x,z,t}$ is more complicated. Specifically, the inner-scaled streamwise variance, $\langle u'^2\rangle^+_{x,z,t}$ (and consequently, TKE^+) displays a distinct upward shift in the location of this peak value for increasing wave steepness. In addition, the normalized peak variance magnitude decreases with ζ. Our analysis shows that even though surface-driven changes impact the various production terms ($\langle P_{11}^{u'u'}\rangle^+_{x,z,t}$ and $\langle P_{11}^{u'v'}\rangle^+_{x,z,t}$) for $\langle u'^2\rangle_{x,z,t}$, the overall variance

production, $\langle P_{11} \rangle^{+}_{x,z,t}$, does not show an upward shift in the peak. Therefore, plausible mechanisms for generation of this upward shift still point to the vertical variance being modulated through the pressure-strain term.

Overall, in the absence of significant flow separation, the surface undulations seem to generate vertical turbulence fluctuations closer to the surface which in turn modulates the entire near-wall turbulence structure. In the presence of steeper 2D waves with significant flow separation or three-dimensional wavy surfaces, the complexity starts to rise due to the generation of spanwise fluctuations near the surface.

Also, the deviation from equilibrium is not only a function of vertical distance due to the presence of streamwise homogeneity. Comparison between the upstream and downstream physics exhibits intriguing asymmetric structure that is strongest near the region with maximum local slope.

6.2 Future Work

Major follow up research can be conducted taking into account the outcome of the current study. Some of them are as follows:

- Higher Reynolds number cases can be investigated, which we have already started working on. That will give us even more information to characterize the roughness and understand the roughness sublayer physics.

- Also, we are working on a similar set of cases where we are taking care to fix the frictional Reynolds number so that the increased friction velocity has minimal influence on our analysis.

- While in the current work we modulated the steepness only by changing the wavelength, both wavelength and amplitude can be varied so that their individual effect can be identified.

- More separation dominated cases can be included in the analysis to understand the physics driven by the flow detachment near the wall.

- To better understand the deviations from equilibrium in the components of the Reynolds stress tensor, a dissection of the various terms in the Reynolds stress transport including production ($\mathcal{P}$), dissipation ($\mathcal{E}$) and pressure-rate-of-strain ($\mathcal{R}$) terms can be performed.

- Inhomogeneity effect due to the horizontal undulation can be further analysed based on the dispersion of turbulence structure which can potentially utilize the averaging using global coordinate system as discussed in section 5.2.

References

Busse, A., Thakkar, M., and Sandham, N. (2017). Reynolds-number dependence of the near-wall flow over irregular rough surfaces. *Journal of Fluid Mechanics*, 810:196–224.

Chan, L., MacDonald, M., Chung, D., Hutchins, N., and Ooi, A. (2015). A systematic investigation of roughness height and wavelength in turbulent pipe flow in the transitionally rough regime. *Journal of Fluid Mechanics*, 771:743–777.

Coceal, O., Thomas, T., Castro, I., and Belcher, S. (2006). Mean flow and turbulence statistics over groups of urban-like cubical obstacles. *Boundary-Layer Meteorology*, 121(3):491–519.

Colebrook, C. F., Blench, T., Chatley, H., Essex, E., Finniecome, J., Lacey, G., Williamson, J., and Macdonald, G. (1939). Correspondence. turbulent flow in pipes, with particular reference to the transition region between the smooth and rough pipe laws.(includes plates). *Journal of the Institution of Civil engineers*, 12(8):393–422.

Darcy, H. (1857). *Recherches expérimentales relatives au mouvement de l'eau dans les tuyaux*. Mallet-Bachelier.

De Marchis, M. and Napoli, E. (2012). Effects of irregular two-dimensional and three-dimensional surface roughness in turbulent channel flows. *International Journal of Heat and Fluid Flow*, 36:7–17.

Flack, K., Schultz, M., and Connelly, J. (2007). Examination of a critical roughness height for outer layer similarity. *Physics of Fluids*, 19(9):095104.

Flack, K. A. and Schultz, M. P. (2010). Review of hydraulic roughness scales in the fully rough regime. *Journal of Fluids Engineering*, 132(4):041203.

Flack, K. A. and Schultz, M. P. (2014). Roughness effects on wall-bounded turbulent flows. *Physics of Fluids*, 26(10):101305.

Flack, K. A., Schultz, M. P., and Shapiro, T. A. (2005). Experimental support for townsends reynolds number similarity hypothesis on rough walls. *Physics of Fluids*, 17(3):035102.

Ganju, S., Davis, J., Bailey, S. C., and Brehm, C. (2019). Direct numerical simulations of turbulent channel flows with sinusoidal walls. In *AIAA Scitech 2019 Forum*, page 2141.

Gautier, R., Laizet, S., and Lamballais, E. (2014). A dns study of jet control with microjets using an immersed boundary method. *International Journal of Computational Fluid Dynamics*, 28(6-10):393–410.

Hama, F. R. (1954). Boundary layer characteristics for smooth and rough surfaces. *Trans. Soc. Nav. Arch. Marine Engrs.*, 62:333–358.

Hultmark, M., Vallikivi, M., Bailey, S., and Smits, A. (2013). Logarithmic scaling of turbulence in smooth-and rough-wall pipe flow. *Journal of Fluid Mechanics*, 728:376–395.

Jayaraman, B. and Brasseur, J. (2014). Transition in atmospheric turbulence structure from neutral to convective stability states. In *32nd ASME Wind Energy Symposium*, page 0868.

Jayaraman, B. and Brasseur, J. G. (2018). Transition in atmospheric boundary layer turbulence structure from neutral to moderately convective stability states and implications to large-scale rolls. *arXiv preprint arXiv:1807.03336*.

Jiménez, J. (2004). Turbulent flows over rough walls. *Annu. Rev. Fluid Mech.*, 36:173–196.

Kim, J. and Moin, P. (1985). Application of a fractional-step method to incompressible navier-stokes equations. *Journal of computational physics*, 59(2):308–323.

Kim, J., Moin, P., and Moser, R. (1987). Turbulence statistics in fully developed channel flow at low reynolds number. *Journal of fluid mechanics*, 177:133–166.

Krogstad, P.-Å. and Efros, V. (2012). About turbulence statistics in the outer part of a boundary layer developing over two-dimensional surface roughness. *Physics of Fluids*, 24(7):075112.

Laizet, S. and Lamballais, E. (2009). High-order compact schemes for incompressible flows: A simple and efficient method with quasi-spectral accuracy. *Journal of Computational Physics*, 228(16):5989–6015.

Lee, M. and Moser, R. D. (2015). Direct numerical simulation of turbulent channel flow up to $Re_\tau \approx 5200$. *Journal of Fluid Mechanics*, 774:395–415.

Lele, S. K. (1992). Compact finite difference schemes with spectral-like resolution. *Journal of computational physics*, 103(1):16–42.

Leonardi, S., Orlandi, P., and Antonia, R. A. (2007). Properties of d-and k-type roughness in a turbulent channel flow. *Physics of fluids*, 19(12):125101.

Lumley, J. L. and Newman, G. R. (1977). The return to isotropy of homogeneous turbulence. *Journal of Fluid Mechanics*, 82(1):161–178.

Moody, L. F. (1944). Friction factors for pipe flow. *Trans. ASME*, 66:671–684.

Nakato, M., Onogi, H., Himeno, Y., Tanaka, I., and Suzuki, T. (1985). Resistance due to surface roughness. In *Proceedings of the 15th Symposium on Naval Hydrodynamics*, pages 553–568.

Napoli, E., Armenio, V., and De Marchis, M. (2008). The effect of the slope of irregularly distributed roughness elements on turbulent wall-bounded flows. *Journal of Fluid Mechanics*, 613:385–394.

Nikuradse, J. (1950). *Laws of flow in rough pipes*. National Advisory Committee for Aeronautics Washington, DC.

Parnaudeau, P., Lamballais, E., Heitz, D., and Silvestrini, J. H. (2004). Combination of the immersed boundary method with compact schemes for dns of flows in complex geometry. In *Direct and Large-Eddy Simulation V*, pages 581–590. Springer.

Perry, A. and Li, J. D. (1990). Experimental support for the attached-eddy hypothesis in zero-pressure-gradient turbulent boundary layers. *Journal of Fluid Mechanics*, 218:405–438.

Perry, A., Lim, K., and Henbest, S. (1987). An experimental study of the turbulence structure in smooth-and rough-wall boundary layers. *Journal of Fluid Mechanics*, 177:437–466.

Perry, A. E., Schofield, W. H., and Joubert, P. N. (1969). Rough wall turbulent boundary layers. *Journal of Fluid Mechanics*, 37(2):383–413.

Peskin, C. S. (1972). Flow patterns around heart valves: a numerical method. *Journal of computational physics*, 10(2):252–271.

Pope, S. B. (2001). Turbulent flows.

Raupach, M., Antonia, R., and Rajagopalan, S. (1991). Rough-wall turbulent boundary layers. *Applied mechanics reviews*, 44(1):1–25.

Schultz, M. and Flack, K. (2005). Outer layer similarity in fully rough turbulent boundary layers. *Experiments in Fluids*, 38(3):328–340.

Schultz, M. and Flack, K. (2007). The rough-wall turbulent boundary layer from the hydraulically smooth to the fully rough regime. *Journal of Fluid Mechanics*, 580:381–405.

Schultz, M. P. (2007). Effects of coating roughness and biofouling on ship resistance and powering. *Biofouling*, 23(5):331–341.

Schultz, M. P. and Flack, K. A. (2009). Turbulent boundary layers on a systematically varied rough wall. *Physics of Fluids*, 21(1):015104.

Shockling, M., Allen, J., and Smits, A. (2006). Roughness effects in turbulent pipe flow. *Journal of Fluid Mechanics*, 564:267–285.

Thakkar, M., Busse, A., and Sandham, N. (2018). Direct numerical simulation of turbulent channel flow over a surrogate for nikuradse-type roughness. *Journal of Fluid Mechanics*, 837.

Townsend, A. (1980). *The structure of turbulent shear flow*. Cambridge university press.

Volino, R., Schultz, M., and Flack, K. (2009). Turbulence structure in a boundary layer with two-dimensional roughness. *Journal of Fluid Mechanics*, 635:75–101.

Volino, R. J., Schultz, M. P., and Flack, K. A. (2011). Turbulence structure in boundary layers over periodic two-and three-dimensional roughness. *Journal of Fluid Mechanics*, 676:172–190.

APPENDIX A

Numerical Scheme Expanded

1.1 Governing Equations

Incompressible Navier-Stokes equations for Newtonian flow in a Cartesian co-ordinate system where x,y,z refers to streamwise, vertical and spanwise directions respectively:

$$\frac{\partial \mathbf{u}}{\partial t} = -\nabla p - \frac{1}{2}\big[\nabla(\mathbf{u} \oplus \mathbf{u}) + (\mathbf{u}\nabla)\mathbf{u})\big] + \nu\nabla^2\mathbf{u} + \mathbf{f} \tag{1.1}$$

$$\nabla.\mathbf{u} = 0. \tag{1.2}$$

Here, $\mathbf{f}$ is the body force, p is the pressure field and density is considered constant $\rho = 1$. Now we let $\mathbf{F}$ be expressed as:

$$\mathbf{F} = \frac{1}{2}\big[\nabla(\mathbf{u} \oplus \mathbf{u}) + (\mathbf{u}\nabla)\mathbf{u})\big] + \nu\nabla^2\mathbf{u} \tag{1.3}$$

To further break down into components in different direction, the x-momentum equation (streamwise component) is expressed as:

$$\frac{\partial u}{\partial t} = -\frac{\partial p}{\partial x} - \frac{1}{2}\left[\frac{\partial(u^2)}{\partial x} + \frac{\partial(uv)}{\partial y} + \frac{\partial(uw)}{\partial z} + u\frac{\partial(u)}{\partial x} + v\frac{\partial(u)}{\partial y} + w\frac{\partial(u)}{\partial z}\right] + \nu\left[\frac{\partial^2(u)}{\partial x^2} + \frac{\partial^2(u)}{\partial y^2} + \frac{\partial^2(u)}{\partial z^2}\right] + f_x. \tag{1.4}$$

Y and z-momentum equations can be expressed in a similar fashion.

1.2 Fractional Step Method

Assuming the x-directional body force $f_x = 0$, the first fractional step for x-momentum equation of AB3 scheme is expressed as:

$$\frac{u^{**} - u^k}{\Delta t} = \frac{1}{12}\Big[23F_x^k - 16F_x^{k-1} + 5F_x^{k-2}\Big] \tag{1.5}$$

Staggered grid system is used for storing pressure and velocities are stored on collocated nodes. 6OCCS is used to calculate the first and second derivatives in the $\mathbf{F_x}$ terms which are also stored at collocated nodes. This ends the first fractional step. The

procedure for the second fractional step is as follows:

$$\frac{u^{k+1} - u^{**}}{\Delta t} = -c_k \nabla \tilde{p}^{k+1} \tag{1.6}$$

For AB3, $c_k = 1$. Now, to get $\nabla \tilde{p}^{k+1}$ we take the divergence of equation 1.6 and set $\nabla u^{k+1} = 0$ to ensure zero divergence condition and thereby conserve mass flow. Thus, we get the following Pressure Poisson Equation (PPE):

$$\nabla . \nabla \tilde{p}^{k+1} = \frac{\nabla[-u^{**}(1-\epsilon)]}{c_k \Delta t} \tag{1.7}$$

Here, the ∇ is a 6OSCS operator that acts on p to give $\nabla \tilde{p}^{k+1}$ on collocated nodes. Then it acts again to give $\nabla . \nabla \tilde{p}^{k+1}$ on staggered grid. This technique ensures strict equivalence of derivatives in the physical space and proper coupling between velocity and pressure. In IBM framework, ϵ is a flag to distinguish between solid body and fluid region ($\epsilon = 1$ for solid body, $\epsilon = 0$ for everywhere else). Now, we apply Fast Fourier Transform (FFT) on the equation 1.7. We would like to specify for the clarification of the reader that this spectral treatment is done only in the streamwise and spanwise direction in the current simulations leveraging the periodic boundary condition. In the vertical direction, classical tridiagonal solver is used because of the no-slip boundary condition as well as the clustered grid very near the wall. However, the benefit of staggered grid system is employed to ensure strict equivalence in the spectral space. The first derivative 6OSCS can be expressed as follows:

$$\alpha f'_{i-\frac{1}{2}} + f'_{i+\frac{1}{2}} + \alpha f'_{i+\frac{3}{2}} = a\frac{f_{i+1} + f_i}{\Delta x} + b\frac{f_{i+2} + f_{i-1}}{3\Delta x} \tag{1.8}$$

The numerator of PPE is the divergence which can be expressed as D. So, considering $D = \nabla[-u^{**}(1-\epsilon)]$ the equation becomes:

$$\nabla . \nabla \tilde{p}^{k+1} = \frac{D}{c_k \Delta t} \tag{1.9}$$

D is first calculated and then FFT is applied along the streamwise and spanwise direction while a direct banded Tridiagonal Matrix Algorithm (TDMA) solver is used along the vertical direction as mentioned before to solve for $\tilde{p}^{k+1}$ on collocated nodes. At this point, u^{**} in the 2^{nd} fractional step as in equation 1.6 is consistent with the $\tilde{p}^{k+1}$. So, we proceed to get u^{k+1} on collocated nodes as shown by the following equation:

$$u^{k+1} = u^{**} - c_k \tilde{p}^{k+1} \tag{1.10}$$

More details on the technique of solving PPE for inhomogeneous geometry is found in Laizet and Lamballais (2009).

1.3 Discretizing the Derivatives

The first derivative is discretized as follows:

$$\alpha f'_{i-1} + f'_i + \alpha f'_{i+1} = a\frac{f_{i+1} + f_{i-1}}{2\Delta x} + b\frac{f_{i+2} + f_{i-2}}{4\Delta x} \tag{1.11}$$

And, second derivative is discretized as follows:

$$\alpha f''_{i-1} + f''_i + \alpha f''_{i+1} = a\frac{f_{i+1} - 2f_i + f_{i-1}}{2\Delta x^2} + b\frac{f_{i+2} - 2f_i + f_{i-2}}{4\Delta x^2} + c\frac{f_{i+3} - 2f_i + f_{i-3}}{9\Delta x^2} \tag{1.12}$$

Laizet and Lamballais (2009) used the same compact scheme to build their incompressible flow solver with quasi-spectral accuracy. We built on their numerical scheme and chose the co-efficient α,a,b,c exactly as they did. Their approximations is based on the work of Lele (1992) who discussed elaborately on different compact schemes and how the right choice of co-efficients can lead to different order of accuracy. To obtain spectral-like accuracy he chose $\alpha = \frac{1}{3}$, $a = \frac{14}{9}$ and $b = \frac{1}{9}$ for the first derivative that gives a sixth order tridiagonal scheme. For second derivative same order of accuracy is obtained by choosing $\alpha = \frac{2}{11}$, $a = \frac{12}{11}$, $b = \frac{3}{11}$ and $c = 0$. However, these sixth order tridiagonal schemes can only be used in the internal nodes. For the boundary nodes we use one-sided formulations for both first and second derivatives as shown below respectively which are both third order accurate:

$$f'_1 + 2f'_2 = \frac{1}{2\Delta x}(-5f_1 + 4f_2 + f_3) \tag{1.13}$$

$$f''_1 + 11f''_2 = \frac{1}{\Delta x^2}(13f_1 - 27f_2 + 15f_3 - f_4) \tag{1.14}$$

Again, for the nodes adjacent to the boundary, three point formulations are used. Both first and second derivative the schemes are fourth order accurate and expressed as following respectively:

$$\frac{1}{4}f'_1 + f'_2 + \frac{1}{4}f'_3 = \frac{3}{2}\frac{f_3 - f_1}{2\Delta x} \tag{1.15}$$

$$\frac{1}{10}f''_1 + f''_2 + \frac{1}{10}f''_3 = \frac{6}{5}\frac{f_3 - 2f_2 + f_1}{\Delta x^2} \tag{1.16}$$

APPENDIX B

Roughness Function Correlations of Nikuradse and Colebrook

2.1 Nikuradse's Correlations

The logarithmic velocity profile corresponding to the law of the wall for turbulent boundary layers is given by

$$\langle u \rangle^+ = \frac{1}{\kappa} ln(y^+) + A, \tag{2.1}$$

where, A is the intercept. Nikuradse (1950) generated correlations for this intercept as a function of roughness Reynolds number, $k^+ = \frac{ku_\tau}{\nu}$ as $A_{nik} = f(k^+)$. For hydraulically smooth regime this correlation is

$$A_{nik,smooth} = 5.5 + 5.75 log_{10} k^+; \quad \text{for} \quad 0 \leq log_{10} k^+ \leq 0.55. \tag{2.2}$$

The transitionally rough regime is further divided into three regions and different correlations were proposed as follows

$$A_{nik} = 6.59 + 3.5 log_{10} k^+; \quad \text{for} \quad 0.55 \leq log_{10} k^+ \leq 0.85 \tag{2.3a}$$

$$A_{nik} = 9.58; \quad \text{for} \quad 0.85 \leq log_{10} k^+ \leq 1.15 \tag{2.3b}$$

$$A_{nik} = 11.5 - 1.62 log_{10} k^+; \quad \text{for} \quad 1.15 \leq log_{10} k^+ \leq 1.83 \tag{2.3c}$$

For fully rough regime the intercept is a constant:

$$A_{nik,rough} = 8.48; \quad \text{for} \quad log_{10} k^+ \geq 1.83. \tag{2.4}$$

Using these correlations, the mean roughness function can be expressed as:

$$\Delta \langle u \rangle^+ = A_{nik,smooth} - A_{nik} \tag{2.5}$$

2.2 Colebrook's Correlation

Colebrook et al. (1939) proposed an alternative relationship for the entire roughness Reynolds number regime given by

$$\Delta \langle u \rangle^+ = \frac{1}{\kappa} ln(1 + 0.3k^+), \tag{2.6}$$

k^+ being the normalized equivalent roughness height. The asymptotic behavior in the fully rough limit is then written as:

$$\Delta\langle u\rangle^+ = \frac{1}{\kappa} ln(0.3k^+) \tag{2.7}$$

with $\kappa = 0.4$.

APPENDIX C

Dissection of the Transport Equation for Reynolds Stress Tensor

Transport equation for Reynolds stress tensor is expressed using index notation as

$$\underbrace{\frac{\partial}{\partial t}\langle u_i' u_j' \rangle_{z,t}}_{\mathcal{L}_{ij}} + \underbrace{\langle u_k \rangle_{z,t} \frac{\partial \langle u_i' u_j' \rangle_{z,t}}{\partial x_k}}_{\mathcal{C}_{ij}} = \underbrace{-\langle u_k' u_j' \rangle_{z,t} \frac{\partial \langle u_i \rangle_{z,t}}{\partial x_k} - \langle u_k' u_i' \rangle_{z,t} \frac{\partial \langle u_j \rangle_{z,t}}{\partial x_k}}_{\mathcal{P}_{ij}} - \underbrace{2\nu \Big\langle \frac{\partial u_j'}{\partial x_k} \frac{\partial u_i'}{\partial x_k} \Big\rangle_{z,t}}_{\epsilon_{ij}}$$
$$+ \underbrace{\Big\langle \frac{p'}{\rho} \Big(\frac{\partial u_i'}{\partial x_j} + \frac{\partial u_j'}{\partial x_i} \Big) \Big\rangle_{z,t}}_{\mathcal{R}_{ij}} + \underbrace{\frac{\partial}{\partial x_k} \Big[\langle -u_i' u_j' u_k' \rangle_{z,t} + \nu \frac{\partial}{\partial x_k} \langle u_i' u_j' \rangle_{z,t} - \Big\langle \frac{p'}{\rho} (\delta_{ki} u_j' + \delta_{kj} u_i') \Big\rangle_{z,t} \Big]}_{\mathcal{D}_{ij}}. \tag{3.1}$$

Here $\mathcal{L}_{ij}$ is the term corresponding to local change with time. $\mathcal{C}_{ij}$ is the convective transport term. $\mathcal{P}_{ij}$ represents the production of Reynolds stresses which is the negative product of Reynolds stress and the gradient of time-averaged velocity. Diagonal terms of the production tensor contributes to the production of turbulent energy. Dissipation of Reynolds stress is represented by ϵ_{ij}. $\mathcal{R}_{ij}$ is the pressure-rate-of-strain correlation contributing to the redistribution of Reynolds stress. Finally $\mathcal{D}_{ij}$ represents the diffusion of Reynolds stresses. In our study, leveraging spanwise homogeneity and temporal stationarity, all turbulent quantities are averaged along spanwise (z) direction and over 2500 temporal snapshots suggested by the $<>_{z,t}$ notation. Statistical stationarity renders $\mathcal{L}_{ij} = 0$ in our case. So,

$$\mathcal{C}_{ij} = \mathcal{P}_{ij} - \epsilon_{ij} + \mathcal{R}_{ij} + \mathcal{D}_{ij}. \tag{3.2}$$

In the following analysis, we averaged all of these quantities along the inhomogeneous streamwise (x) direction (i.e. double averaging). The unified effect of production, dissipation and pressure-rate-of-strain is characterized using a term Λ expressed as

$$\langle \Lambda_{ij} \rangle_x = \langle \mathcal{P}_{ij} \rangle_x - \langle \epsilon_{ij} \rangle_x + \langle \mathcal{R}_{ij} \rangle_x. \tag{3.3}$$

Also we computed the diffusion term ($\langle \mathcal{D} \rangle_x$) as

$$\langle \mathcal{D}_{ij} \rangle_x = \langle \mathcal{C}_{ij} \rangle_x - \langle \Lambda_{ij} \rangle_x. \tag{3.4}$$

We point to the benefit of readers that the streamwise averaging can not be interchanged with the spanwise and temporal averaging because of the streamwise inhomogeneity (i.e. $\langle \mathcal{P}_{ij} \rangle_x \neq \langle u_k' u_j' \rangle_{x,z,t} \frac{\partial \langle u_i \rangle_{x,z,t}}{\partial x_k}$). Also, the superscript a and b in the convective transport term represents $k = 1$ and $k = 2$ components respectively.

VITA

Saadbin Khan

Candidate for the Degree of

Master of Science

Thesis: NEAR WALL STRUCTURE AND DEVIATION FROM EQUILIBRIUM IN WAVY CHANNEL TURBULENCE

Major Field: Mechanical & Aerospace Engineering

Biographical:

Personal Information:

Born at Barisal Bangladesh in November of 1993.

Education:

Completed Bachelors of Science in Mechanical Engineering at Bangladesh University of Engineering and Technology, Dhaka, Bangladesh in March 2016.

Completed the requirements for the degree of Master of Science with a major in Mechanical & Aerospace Engineering at Oklahoma State University in July 2019.